A Strontium lattice clock with reduced blackbody radiation shift

Von der QUEST-Leibniz-Forschungsschule der
Gottfried Wilhelm Leibniz Universität Hannover
zur Erlangung des Grades

Doktor der Naturwissenschaften
Dr. rer. nat.

genehmigte Dissertation
von

M.Sc.-Phys. Ali Khalas Anfoos Al-Masoudi
geboren am 04.07.1986, in Babylon

2016

Referent	PD Dr. Christian Lisdat Physikalisch-Technische Bundesanstalt
Koreferent	Prof. Dr. Ernst M. Rasel Leibniz Universität Hannover
Tag der Disputation	30.09.2016

Abstract

Optical clocks have been quickly moving to the forefront of the frequency standards field due to their high spectral resolution, and therefore the potential high stability and accuracy. The accuracy and stability of the optical clocks are nowadays two orders of magnitude better than microwave Cs clocks, which realize the SI second. Envisioned applications of highly accurate optical clocks are to perform tests of fundamental physics, for example, searching for temporal drifts of the fine structure constant α [Pei04, Ros08, Hun14], violations of the Local Position Invariance (LPI) [For07], dark matter and dark energy [Der14, Arv15], or to performance relativistic geodesy [Bje85].

In this work, the uncertainty of a strontium lattice clock, based on the ${}^1S_0 - {}^3P_0$ transition in ^{87}Sr, due to the blackbady radiation (BBR) shift has been reduced to less than 1×10^{-18} by more than one order of magnitude compared to the previous evaluation of the BBR shift uncertainty in this clock. The BBR shift has been reduced by interrogating the atoms in a cryogenic environment. The systematic uncertainty of the cryogenic lattice clock is evaluated to be 1.3×10^{-17} which is dominated by the uncertainty of the AC Stark shift of the lattice laser and the uncertainty contribution of the BBR shift is negligible.

Concerning the instability of the clock, the detection noise of the clock has been measured, and a model linking noise and clock instability has been developed. This noise model shows that, in our lattice clock, quantum projection noise is reached if more than 130 atoms are interrogated. By combining the noise model with the degradation due to the Dick effect reflecting the frequency noise of the interrogation laser, the instability of the clock is estimated to be $1.6 \times 10^{-16}/\sqrt{\tau/\mathrm{s}}$ [Al-15] in regular operation.

During this work, several high-accuracy comparisons to other atomic clocks have been performed, including several absolute frequency measurements. The Sr clock transition frequency was measured to be 429 228 004 229 873.04 (11) Hz [Gre16], with significant improvements of the statistical uncertainty due to longer measurements and using H-Maser as flywheel to cover any gaps in the operation of the Sr clock. Optical frequency ratio measurements between our clock and a single ${}^{171}\mathrm{Yb}^+$ ion clock [Hun16] at PTB have been carried out, to measure a possible temporal drift of the fine structure constant α. From the measurements the most stringent limit on a potential linear drift of α over time of -0.67×10^{-17} per year with an uncertainty of $\pm0.47 \times 10^{-17}$ has been derived (in preparation). Furthermore, comparisons between the Sr clocks at PTB (Braunschweig) and SYRTE (Paris) via a fiber link [Rau15,Lop15] have been performed, and the fractional offset frequency between them has been measured to be $(4.7 \pm 5.0) \times 10^{-17}$ [Lis16]. Such comparisons over large distances are an important step towards a redefinition of the SI second based on an optical transition.

Keywords: frequency standards, blackbody radiation shift, absolute frequency

Zusammenfassung

Optische Uhren haben sich innerhalb kurzer Zeit eine Spitzenposition im Feld der Frequenzstandards erobert, da sie eine hohe spektrale Auflösung und damit eine hohe Stabilität und Genauigkeit erreichen können. Genauigkeit und Stabilität optischer Uhren sind heute zwei Größenordnungen besser als die der Mikrowellen Cs-Uhren, die zur Realisierung der Sekunde verwendet werden. Mögliche Anwendungen dieser hochgenauen Uhren sind Tests fundamentaler Physik, wie Beispielsweise die Suche nach zeitlichen Variationen der Feinstrukturkonstante α [Pei04, Ros08, Hun14], Verletzungen der lokalen Positions-Invarianz (LPI) [For07], dunkler Materie und dunkler Energie [Der14, Arv15], oder zur Durchführung relativistischer Geodäsie [Bje85].

Im Rahmen dieser Arbeit wurde der Schwarzkörperanteil an der Unsicherheit einer auf dem $^1S_0 - {}^3P_0$ Übergang in ^{87}Sr basierenden Strontium Gitteruhr um etwa eine Größenordnung auf weniger als 1×10^{-18} reduziert. Dafür wurden die Atome in einer kryogenen Umgebung abgefragt. Die systematische Unsicherheit der kryogenen Gitteruhr wurde evaluiert und betrug $1{,}3 \times 10^{-17}$, wobei die Unsicherheit der AC-Stark-Verschiebung durch den Gitterlaser den dominanten Anteil bildet, wohingegen die Unsicherheit durch die Schwarzkörperverschiebung zu vernachlässigen ist.

Im Hinblick auf die Instabilität der Uhr wurde das Detektionsrauschen gemessen und ein Modell zur Verknüpfung des Detektionsrauschens mit der Instabilität entwickelt. Dieses Modell zeigt, dass das Quantenprojektionsrauschlimit erreicht wird, wenn mehr als 130 Atome abgefragt werden. Durch Kombination des Rauschmodells mit einer Abschätzung des Dick-Effektes, welcher die Laserinstabilität wiederspiegelt, wurde die Instabilität der Uhr als $1{,}6 \times 10^{-16}/\sqrt{\tau/\mathrm{s}}$ [Al-15] für den regulären Uhrenbetrieb abgeschätzt.

Während dieser Arbeit wurden mehrere hochgenaue Vergleichsmessungen mit anderen Atomuhren durchgeführt, darunter einige Absolutfrequenzmessungen. Als Ergebnis wurde die Frequenz des Uhrenübergangs als 429 228 004 229 873,04 (11) Hz [Gre16] gemessen, wobei aufgrund der langen Messzeit signifikante Verbesserungen der statistischen Unsicherheit erreicht werden konnten. Zudem wurde ein Wasserstoffmaser als Schwungrad benutzt um Zeiten zu überbrücken in denen die Strontiumuhr nicht einsatzbereit war. Das optische Frequenzverhältnis zu einer $^{171}Yb^+$ Einzelionenuhr [Hun16] wurde gemessen, um mögliche zeitliche Variationen der Feinstrukturkonstante α zu detektieren. Aus diesen Messungen kann ein Limit für eine potentielle lineare Drift von α gegeben werden, dass $-0{,}67 \times 10^{-17}$ pro Jahr mit einer Unsicherheit von $\pm 0{,}47 \times 10^{-17}$ beträgt. Weiterhin wurden Vergleiche zwischen Sr-Uhren an der PTB (Braunschweig) und SYRTE (Paris) über einen optischen Faserlink [Rau15, Lop15] durchgeführt. Der relative Frequenzunterschied zwischen den beiden Uhren betrug $(4{,}7 \pm 5{,}0) \times 10^{-17}$ [Lis16]. Derartige Vergleiche über große Entfernungen sind ein wichtiger Schritt in Richtung einer Neudefinition der SI-Sekunde durch einen optischen Übergang.

Stichworte: Frequenzstandards, Schwarzkörperverschiebung, Absolutfrequenz

Publications

Stephan Falke, Nathan Lemke, Christian Grebing, Burghard Lipphardt, Stefan Weyers, Vladislav Gerginov, Nils Huntemann, Christian Hagemann, **Ali Al-Masoudi** , Sebastian Häfner, Stefan Vogt, Uwe Sterr and Christian Lisdat.
A strontium lattice clock with 3×10^{-17} inaccuracy and its frequency.
New Journal of Physics **16**, 073023 (2014).

Ali Al-Masoudi, Sören Dörscher, Sebastian Häfner, Uwe Sterr and Christian Lisdat.
Noise and instability of an optical lattice clock.
Physical Review A **92**, 063814 (2015).

C. Lisdat and G. Grosche and N. Quintin and C. Shi and S. M. F. Raupach and C. Grebing and D. Nicolodi and F. Stefani and **A. Al-Masoudi** and S. Dörscher and S. Häfner and J. -L. Robyr and N. Chiodo and S. Bilicki and E. Bookjans and A. Koczwara and S. Koke and A. Kuhl and F. Wiotte and F. Meynadier and E. Camisard and M. Abgrall and M. Lours and T. Legero and H. Schnatz and U. Sterr and H. Denker and C. Chardonnet and Le Coq, Y. and G. Santarelli and A. Amy-Klein and Le Targat, R. and J. Lodewyck and O. Lopez and P.-E. Pottie.
A clock network for geodesy and fundamental science.
Nature Com. **7**, 12443 (2016).

C. Grebing and **A. Al-Masoudi** and S. Dörscher and S. Häfner and V. Gerginov and S. Weyers and B. Lipphardt and F. Riehle and U. Sterr and C. Lisdat.
Realization of a time-scale with an optical clock.
optica, **3**, 563-569 (2016).

Stefan Vogt, Sebastian Häfner, Jacopo Grotti, Silvio Koller, **Ali Al-Masoudi**, Uwe Sterr and Christian Lisdat.
A transportable optical lattice clock.
Journal of Physics: Conference Series **723**, 012020 (2016).

Contents

Chapter 1

Introduction

During the 20th century, high-precision spectroscopy played a prominent role and it has been improved over the years until now. High-precision spectroscopy has provided unbelievable contributions to the understanding the modern physics, for example, lamb shift in atomic hydrogen and deuterium [Wei94,Sch99], nuclear magnetic moments, etc. This kind of measurements were a great input for theoreticians to develop more accurate theories.

In 1960 the laser is invented [Mai60], thus opening a new area for high resolution spectroscopy of optical transitions in atoms, ions, and molecules. As another great step laser cooling gave access to cold atoms and ions [Win75,Hän75,Win79,Phi85,Chu85] were major breakthroughs in the development for improving the high resolution spectroscopy, leading for example to fountain atomic clocks.

Time or frequency have become the most accurate physical quantity (both in optical and in microwave frequencies). The progress of building atomic clocks based on optical transitions was dramatically speeded up when the frequency comb [Hän06, Cun01, For07] was invented, which allows us to measure absolute frequency measurements at high frequency much more accurately and simpler compared to the method of frequency chains [Tel96, Sch96].

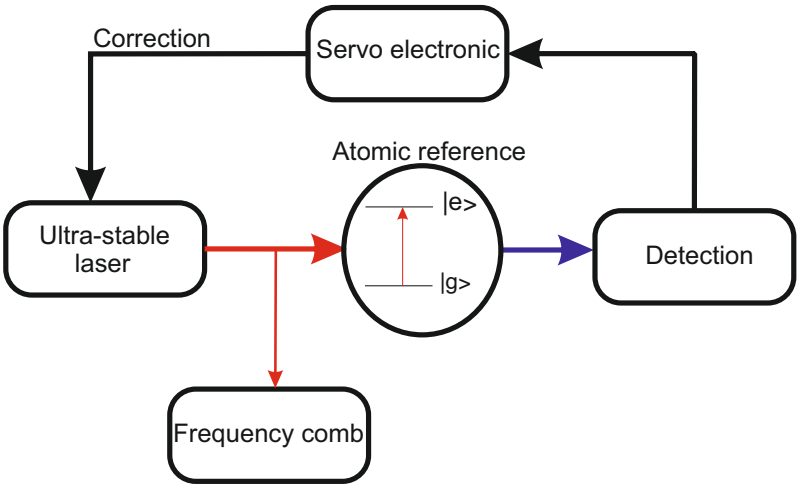

Figure 1.1: Schematic of an optical atomic clock. An ultra-stable laser is steered to an atomic transition reference by correction signals derived from atomic spectroscopy. The optical frequency can be converted to other frequency domains by a frequency comb.

1.1 Optical clocks

The principle of a optical clocks is as following: an ultra-stable laser is used as the local oscillator for the clock because of the laser frequency is sensitive to environment effects, it cannot be used as frequency standard alone. Thus the light is used to probe a narrow atomic transition of an atom or ion. A transition between two eigenstates has an energy difference of ΔE, which relates to emission or absorption of electromagnetic radiation of frequency of $f = \Delta E/h$. The energy differences, thus the atomic transition frequencies depend on the fundamental properties of an atom or ion, thus the frequency of a transition can be used as a reference. The atomic signal (the excitation probability of clock states) is used to determine the difference between the local oscillator frequency and that of the reference atom and apply feedback to the local oscillator frequency as shown in Figure 1.1. Now, the question is: on which criteria can I chose the atomic reference? To answer this question several points have to be considered:

- High Q-factor ($\nu/\Delta\nu$) for better stability of the clock, where ν is the transition frequency and $\Delta\nu$ is the natural linewidth of the transition.

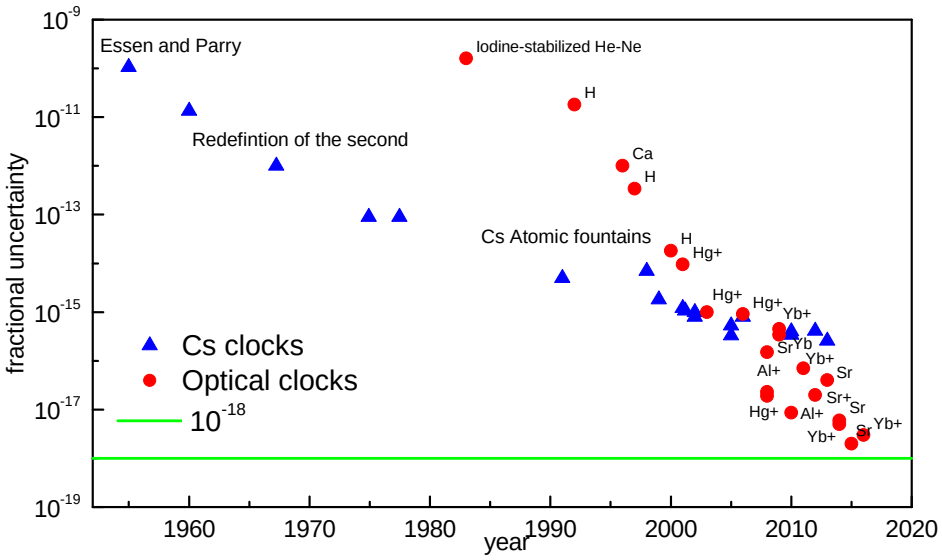

Figure 1.2: Fractional uncertainty of the optical clocks (circles) and primary cesium clocks (triangles).

- The probe time (interrogation time) should be long to observed narrow line width, since the full width at half-maximum (FWHM) $\approx 0.8/t_{pulse}$ (for Rabi interrogation).
- The atomic spectroscopy is observed with high signal to noise ratio (S/N) to improve the stability of the clock.
- The energy of the clock states should be insensitive to the environment surrounding the atom.

Unfortunately, there is no atom or ion that fulfills all the points mentioned above. Each candidate has advantages and disadvantages. The neutral atoms are typically more sensitive to the surrounding environment than single ions. Thus careful investigation of the systematic effects is required as I will explain in chapter 3. Ion clocks suffer from poor signal-to-noise ratio (S/N), thus very long averaging times are required to reduce the statical uncertainty of the measurements. Figure 1.2 shows the evolution of optical and microwave clocks for comparison. The optical clock's development has shown a significantly faster rate of improvement over last decade.

Table 1.1 lists candidate species of optical clocks using neutral atoms and ions, they are under investigation in different countries.

^{87}Sr	^{171}Yb	^{199}Hg	^{24}Mg	^{88}Sr^{+}	^{171}Yb^{+}	^{27}Al^{+}	^{199}Hg^{+}	^{115}In^{+}
Tokyo	NIST	SYRTE	LUH	NPL	PTB	NIST	NIST	PTB
JILA	NMIJ			NRC	NPL	PTB		
SYRTE	KRISS			MIKES				
PTB	INRIM							
NPL	UDuess							
NIM								
UFlo								
Torun								

Table 1.1: Optical clock candidates based on neutral atoms and ions. Research institutions: Tokyo, University of Tokyo. JILA, University of Colorado, Joint Institute for Laboratory Astrophysics. SYRTE, Systémes de Référence Temps Espace, France. PTB, Physikalisch-Technische Bundesanstalt, Germany. NPL, National Physical Laboratory. NIM, National Institute of Metrology, China. UFlo, University of Florence, Italy. Torun, Nicolaus Copernicus University, Poland. NIST, National Institute of Standards and Technology, USA. NMIJ, National Metrology Institute of Japan. KRISS, Korea Research Institute of Standards and Science. INRiM, Istuto Nazionale di Ricerca Metrologica, Italy, UDuess, University Düsseldorf, Germany. MIKES, Mittatekniikan Keskus, Finland. NRC, National Research Council, Canada. Adapted from [Gil11].

1.2 The second and its future

The international system of units (SI) consists of seven base units; the second for time, the meter as the unit of length, the kilogram for mass, the ampere for electrical current, the kelvin for temperature, the mole for the amount of substance, and the candela for luminous intensity. Table 1.2 shows a list of the SI base units together with the physical relation and the methods that are used for realization of the units. I will give here some details on the unit of time, more details on the other SI units can be found in [Kov04, Bor05].

The definition of the second was last revised in 1967 (history of the second before that can be found in [Ram83, Jes99]), where an atomic transition is used, the ground state hyperfine frequency splitting of the ^{133}Cs atom. This was only a decade after Essen and Parry had build a first atomic clock based on Cs atoms in 1955 [Ess55]. Thus the definition of the second became *"The second is the duration of 9 192 631 770 periods of the radiation corresponding to the transition between the two hyperfine levels of the ground state of the ^{133}Cs atom"* [Lev99, Bau12]. At that time the fractional uncertainty of Cs clocks was 10^{-10}, which was a significant improvement compared with previous realizations. Their

unit	Physical relation	method
second	$\nu = \Delta E/h$	Cs clock
meter	$\lambda = c/\nu$	optical interferometer
volt	$U = nh\nu/e$	Josephson junction
ampere	$I = e\nu$	single electron transistor
ohm	$R_K = h/e^2$	quantum Hall effect
kelvin	$T = E/k_B$	Boltzmann's constant

Table 1.2: SI units with physical relation that used for realizations [Pei10]. The unit of mass is omitted here.

uncertainty has been improved significantly over the decades, especially when laser cooling and trapping have arrived, thus enabling higher spectroscopic resolution with cold atoms. These techniques have had great leverage to realize first Cs fountain clock in 1991 [Cla91]. Fountain clocks are used to realize the second with uncertainty below than 10^{-15}, making the second is most accurate SI unit so far, and prompting Arthur Shawlow (the 1981 Nobel Prize winner in physics) *"Never measure anything but frequency!"*.

Redefinition of the second

As I mentioned above, the caesium fountain clock have been used to realize the second for decades. The Cs fountain clocks achieve frequency uncertainties of about 2×10^{-16} at PTB (not published yet). However, optical clocks based on neutral atoms or single ions have shown significant improvement over a decade. Optical clocks have two orders of magnitude better accuracy than the best caesium fountain clocks, nowadays (^{87}Sr lattice clock 2×10^{-18} [Nic15] and single $^{171}Yb^{+}$ ion clock 3×10^{-18} [Hun16]) and they show also better instabilities than caesium fountain clocks. Accuracy and stability of optical clocks have opened the debate in the time and frequency community on a redefinition of the second based on optical clocks since 2001. In 2015, BIPM (International Committee of Weights and Measures), approved a list of secondary representations of the second including several transitions used by optical clocks [CIP15]. There are some questions that have to be addressed before a redefinition the second [Rie15, Gil11]:

- First, of course, do optical clocks have benefits? What are these?
- Are optical clocks ready for the redefinition of the second?

- Do we have enough optical clocks?
- Which candidate transition is going to be used for the definition of the second?

The Cs clocks are very good for the most of the applications, both for society and science. However, realization of the second based on the optical clocks will open new areas of applications, both in science and technology. There are some technical challenges have to be solved before the redefinition. Comparisons of optical clocks separated by large distances (on a continental scale) are essential; this kind of comparison should be limited by the clocks themselves, not by the link. Thus, stable links are required. Unfortunately, satellite link are not yet capable to provide the stability and also accuracy required for comparisons of optical clocks. In order to overcome this problem, optical links are required to link between those clocks. In Europe, there are several optical links under construction between a number of NMIs (National Metrology Institutes) and other research institutes. An optical link between PTB and SYRTE has been operated since 2015, the first comparison between two optical clocks on both ends has been performed in 2015 with our Sr clock. Details on the measurement are given in Chapter 5. For comparisons of optical clocks across continents, transportable optical clocks can do the job. Several transportable optical clocks are under development. Furthermore geodetic modeling has to be improved, very accurate determination of gravitational potential differences is required for this kind of comparison.

The redefinition of the second will take place if optical clocks (at least three clocks) have to shown a systematic uncertainty in level of 10^{-18}. Three or more independent optical frequency measurements limited by the uncertainty of the best Cs atomic clocks. Comparisons of three or more of the optical clocks (same species) at different institutes with an uncertainty of level of 5×10^{-18}, via fiber links or transportable clocks. Optical clocks ratio measurements (more than 5 clocks) have to performed with uncertainty of 5×10^{-18}. The optical clocks have to contributed regularly to TAI (Temps Atomique Internatinal), in English International Atomic Time.

1.3 Outline of the thesis

With the short motivation described in this introduction, I will turn now to more details.

In Chapter 2, I will discuss the experimental setup, the description of cooling, trapping, and high resolution spectroscopy of the ^{87}Sr atoms are introduced. I also discuss in some details how we prepare the ^{87}Sr atoms in a selected nuclear spin state.

In Chapter 3, I describe the accuracy of the Sr lattice clock, I will give some details on the systematic shifts of the ^{87}Sr lattice clock and how we have removed the largest uncertainty contribution of the clock due to blackbody radiation shift by implementing the cold finger inside the vacuum chamber, which can operate at cryogenic temperature.

In chapter 4, I discuss the instability of the clock. I will show how we measure all the noise of the clock and noise model is developed, thus the instability of the clock is estimated.

In chapter 5, I show some applications of the optical clocks, I describe absolute frequency measurements, comparisons between the Sr lattice clocks at PTB and SYRTE via optical fiber link, ratio measurements between the ^{87}Sr lattice clock and the single $^{171}Yb^{+}$ ion clock both at PTB.

In chapter 6, I will briefly summary and discuss the future work in our group and how we will push the accuracy of the clock further by a new vacuum chamber design.

Chapter 2

Preparation and Spectroscopy of ^{87}Sr atoms

In this chapter, details on our experiment are presented. First, the atomic properties of the Sr atoms with energy levels are introduced. Then, I will describe the blue MOT to cool the atoms to few mK, and after that the second stage cooling (red MOT) is presented to cool the atoms further to the μK range. After that, details on the optical lattice trap, spin polarization of the ^{87}Sr atoms, and spectroscopy are described. Finally, the stabilization of the interrogation laser to the clock transition is discussed.

2.1 Strontium atoms

Strontium is one of the alkaline-earth atoms, which comprise group 2 of the periodic table of elements (together with other atoms like Beryllium, Magnesium, Calcium, Barium, and Radium). These atoms have similar atomic properties due to the similarity of their electronic configurations. Atomic Sr has two valence electrons, which produce an interesting mixture of electronic states where the total electron spin can be zero or one, thus resulting to single states or triplet states. The energy diagram is shown in Figure 2.1, the energy levels are described according to the Russell and Saunders notation [Rus24]. The ground state of the Sr atom $^1S_0$ has zero total angular momentum $J = 0$ and zero total electronic spin $S = 0$, which has strong dipole transition to the first excited singlet

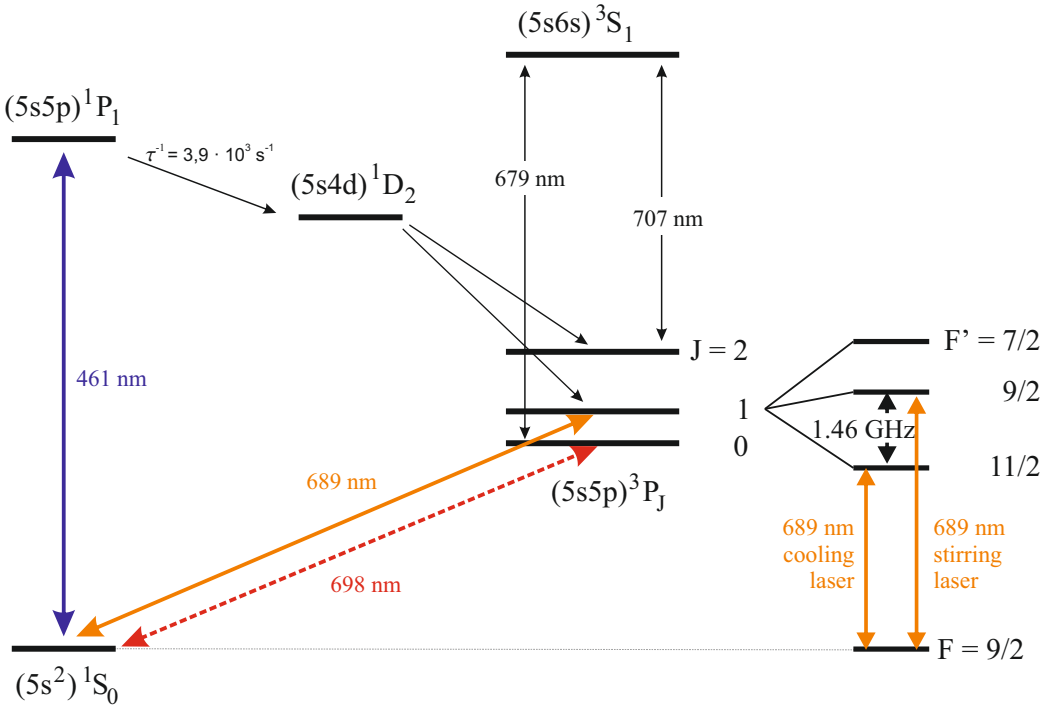

Figure 2.1: Diagram of the energy level of strontium atoms with the transitions used for cooling, repumping, and spectroscopy and their associated wavelength.

Isotope	Abundance	Nuclear Spin
^{84}Sr	0.56 %	0
^{86}Sr	9.9%	0
^{87}Sr	7.0%	9/2
^{88}Sr	82.6%	0

Table 2.1: The natural abundances of the Sr isotopes.

state $^1P_1$. For the coupling between singlet state $^1S_0$ and the triplet states, according to the dipole selection rule $\Delta S = 0$ there is no dipole transitions are allowed, but because of spin-orbit interaction of the $^1P_1$ with $^3P_1$, a weak dipole transition amplitude between $^1S_0$ and $^3P_1$ states exists [Bre33, Boy07c]. This kind of transition is commonly called an intercombination transition. For the $^3P_0$ state, coupling between $^1S_0$ and $^3P_0$ depends on the isotopes of the strontium. It has bosons (^{84}Sr, ^{86}Sr, ^{88}Sr) and fermions (^{87}Sr) as seen table 2.1. For the fermionic isotpoe, which has a nuclear spin of $I = 9/2$, a weak mixing of the $^3P_1$ with $^3P_0$ states exists due to the hyperfine interaction, thus coupling between $^1S_0$ and $^3P_0$ is allowed very weakly. For bosons, an external magnetic field during the spectroscopy is required, more details can be found in [Tai07].

2.2 Sr atoms from atomic oven to blue MOT

Cooling and trapping an atomic sample nowadays are well known techniques; many books and articles deal with them. Cooling and trapping have been studied in depth in [Win79, Phi85, Met99]. For Sr, details on cooling and trapping are given in [Boy07a, Lud08b, Vel10, Mid13, Vog15]. I will summarize briefly how we cool and trap the Sr atoms: The source that provides the Sr atoms is an oven, which is filled with strontium granules. It is a 35 mm long cylinder (stainless steel) with an inner diameter of 4 mm. The oven is heated to 500 °C. A hot atomic beam is produced by sublimation and passes through several capillaries with 2 mm diameter to produce a high-flux, collimated atomic beam. The atomic beam enters a 40 mm long Zeeman slower and interacts with a Zeeman slowing laser coming from the opposite direction, which is red detuned from the $^1S_0 - ^1P_1$ transition (461 nm) by −400 MHz. The atoms are decelerated from their initial velocity of about 550 m/s to about 50 m/s. After that atoms are captured in a 3D magneto-optical trap (MOT) operated on the $^1S_0 - ^1P_1$ transition, which is red detuned from resonance by

-40 MHz. Three collimated beams are sent through free space into vacuum chamber, the two horizontal beams and one vertical beam are retro-reflected back via mirrors. The magnetic field in anti-Helmholtz configuration is used for the blue MOT, which is created by pair of coils located inside the vacuum chamber. These coils are water cooled. The $^1S_0 - {}^1P_1$ transition is not closed perfectly, so atoms can decay to $^3P_2$ via a decay channel through $^1D_2$ (as seen in Figure 2.1), thus reducing the total steady-state atom number in the blue MOT. In order to overcome this, optical repumping is required to pump the atoms from $^3P_2$ into $^1S_0$. The $^3P_2 - {}^3S_1$ transition (707 nm) is used to pump the atoms into the $^3P_1$ state, which decays to the $^1S_0$, and an additional repumper is applied to drive the $^3P_0 - {}^3S_1$ transition (679 nm) and repump any atoms may decay into the long lived $^3P_0$ state in the process. The repumper lasers are frequency modulated about 1-2 GHz by laser's piezo transducer (PZT), which is useful for ^{87}Sr, which has a large number of non-degenerate hyperfine levels which may become populated by the decay or the repumping. Typical atom numbers in the blue MOT are 2×10^7 atoms with 3 mK temperature. The blue laser light at 461 nm is generated by a diode laser at 922 nm that seeds a tapered amplifier and is frequency-doubled in a bow-tie SHG cavity. The maxumim power is bout 250 mW, the output is coupled into a fiber and then split via beam splitter (BS) cubes into Zeeman slower, MOT, and detection branches. The repumper lasers (707 nm, 679 nm) are also commercial ECDLs. The laser beams are coupled together into one fiber and sent into the blue MOT along one direction and reflected back via a mirror.

2.3 Cooling with narrow line width transition

After the Sr atoms have been cooled to about 3 mK on the $^1S_0 - {}^1P_1$ transition, a second stage cooling is applied to cool the atom down to μK temperatures. This (red MOT) uses the $^1S_0 - {}^3P_1$ intercombination transition at 689 nm which has a linewidth of 7.5 kHz. For ^{87}Sr, the MOT does not operate efficiently on the $|^1S_0, F = 9/2\rangle - |^3P_1, F = 11/2\rangle$ transition. Because the g factor of the excited state $^3P_1$ is much larger than that of the ground state $^1S_0$, this leads to, a strong m_F dependence for the transition in the presence of magnetic fields. At a given position, for example at $-x_0$ with $m_F \mu_g B(x_0) < 0$, where MOT beams are send to the atomic sample from both sides, σ^- from right and σ^+ from the left. The atoms can absorb the light from both, as seen in Figure 2.2, where the transition with

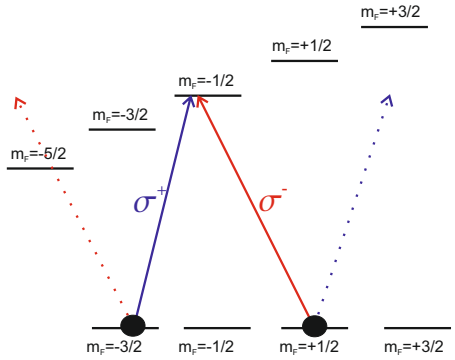

Figure 2.2: Simplified scheme of a MOT operation with $g_e >> g_g$. For example, atoms (with several magnetic sublevels m_F) at a given position (at $-x_0$ with $m_F \mu_g B(x_0) < 0$), atoms in some of m_F magnetic sublevels are excited with σ^+ transition, while other m_F magnetic sublevels are excited with σ^- transition.

$\Delta m_F = -1$ by σ^- light will push atoms outside the MOT while the transition with $\Delta m_F = 1$ by σ^+ light will push atoms into center of the MOT. Fortunately, the probability of absorption from those transitions is also depends on the Clebsch-Gordan (CG) coefficients, thus making the absorption from wrong beam (σ^- transition) is weaker, because it has much smaller Clebsch-Gordan (CG) coefficient compared to the σ^+ transition.

In order to operate the MOT more efficiently, population shaffling of the magnetic sub level is required, e.g., by optically pumping between them by so called Stirring laser (this has been noticed first in Katori group [Muk03]). The transition ${}^1S_0, F = 9/2$ to ${}^3P_1, F = 9/2$ is used for this purpose, because the Zeeman shift is about 5 times smaller that for cooling on ${}^1S_0, F = 9/2$ to ${}^3P_1, F = 11/2$ transition and thus the atoms remain in resonance with stirring laser for longer time and resulting efficiently mixed magnetic sublevels. The 689 nm light, used for cooling, is generated from home made ECDL (master laser), which is stabilized to a 10 cm long ULE cavity. To get sufficient output power for operation of the red MOT, part of the master laser beam is injected to a slave laser for amplification. The slave's output of 15 mW is then sent to the vacuum chamber via fibers. An additional ECDL is used for stirring, it has a frequency offset of 1.4 GHz from the cooling laser and an output power of 5 mW, which is coupled to the same fibers as the master laser. The stirring laser is phase-locked to the master laser.

The red MOT consists of two cooling stages within 140 ms, where during first stage

(90 ms) the frequencies of the cooling and stirring laser are modulated by about 1 MHz to increase the velocity capture range, while during the second stage (50 ms) the modulation frequency is switched off and both intensity and detuning of the lasers are reduced for further cooling the atoms to 2-5 μK.

2.4 Sr atoms in optical lattice trap

Optical lattices are used nowadays as a standard tool for trapping of neutral atoms. They are used in lattices clocks because of their advantages of the suppression of the Doppler and recoil shift in the so called Lamb-Dicke regime [Dic53].

In our experiment, the optical lattice is formed by retro-reflection and it is overlapped and focused to the atomic sample at the MOT position.

The total electric field of the two counterpropogating beams of the 1D lattice can be written as,

$$\vec{E} = \vec{E_0}\cos(kz - \omega t) + \vec{E_0}\cos(-kz - \omega t), \tag{2.1}$$

$$\left|E^2\right| = 2\left|E_0^2\right|\cos^2(kx). \tag{2.2}$$

When atoms are in an AC electric field with a frequency-detuning from an atomic transition of two states, the states will experience an energy shift that depends both on the light's and atomic properties. The shift can be used to trap the atoms, and is expressed by

$$\Delta E = -\frac{1}{2}\alpha(\omega)\left|E^2\right|. \tag{2.3}$$

where $\alpha(\omega)$ is the polarizability of a state and $|E^2|$ is the amplitude square of the electric field. The potential of a standing wave for an 1D lattice trap along the z-axis and assuming a light beam with a Gaussian profile, can be written as

$$U(r,z) = 4U_0 e^{-\frac{2r^2}{w(z)^2}}\cos^2\left(\frac{2\pi z}{\lambda_{\text{laser}}}\right), \tag{2.4}$$

where U_0 is

$$U_0 = \frac{\alpha P}{\pi c \epsilon_0 w_0^2} \tag{2.5}$$

Here, P is the incident beam, w_0 is the beam waist at the focus. By assuming a harmonic trap the longitudinal and radial vibrational frequencies can be written as

$$\nu_z = \frac{1}{2\pi w_0 \lambda}\sqrt{\frac{32\pi\alpha P}{c\epsilon_0 M}} \tag{2.6}$$

and

$$\nu_r = \frac{1}{2\pi w_0^2}\sqrt{\frac{16\pi\alpha P}{c\pi\epsilon_0 M}}, \tag{2.7}$$

where M is the atomic mass of Sr.

In our setup, we are using a horizontally oriented 1D lattice that is linearly polarized. The laser light is generated by a Ti:sapphire laser from the company M2. Its frequency is stabilized to a frequency comb and it tuned to the magic wavelength at 813 nm [Kat03] (at the magic wavelength, the first order light AC Stark shift of the clock transition due to the optical lattice cancels). The lattice waist is about 65 μm. An incident lattice power of 280 mW produces lattice depth of 70 E_r, (E_r is the photon recoil energy of the lattice light $E_r = \hbar k^2/2m$), which corresponds to an axial frequency of 58 kHz and a radial frequency of 165 Hz. The lattice trap is on during the MOT stages and atoms are loaded from the single frequency red MOT into the lattice trap. The coldest atoms (in the axial vibrational state $\nu = 0$) are selected by ramping the lattice depth down to about 40 E_r, to allow hot atoms in higher vibrational states to leave the trap, for 20 ms and then ramping back to the typical operation depth, thus about 25% from atoms are remaining in the trap.

2.5 Spin polarization and spectroscopy

Once the coldest atoms are trapped in the lattice trap, an other issue that has to be taken into account is that, in presence of an external magnetic field, the degeneracy of the Zeeman sublevels is lifted resulting in a splitting of the clock transition, thus an additional frequency shift to the clock transition due to Zeeman shift is presented, as written in Eqs.(3.12, 3.13). In case of ^{87}Sr atoms with nuclear spin $I = 9/2$, there are 10 magnetic sublevels (for $F = 9/2$). The population of the magnetic sublevel are nearly equally distributed over all the magnetic sublevels. The population distribution is not desired for high accuray and precision measurements because each magnetic sublevel has a different

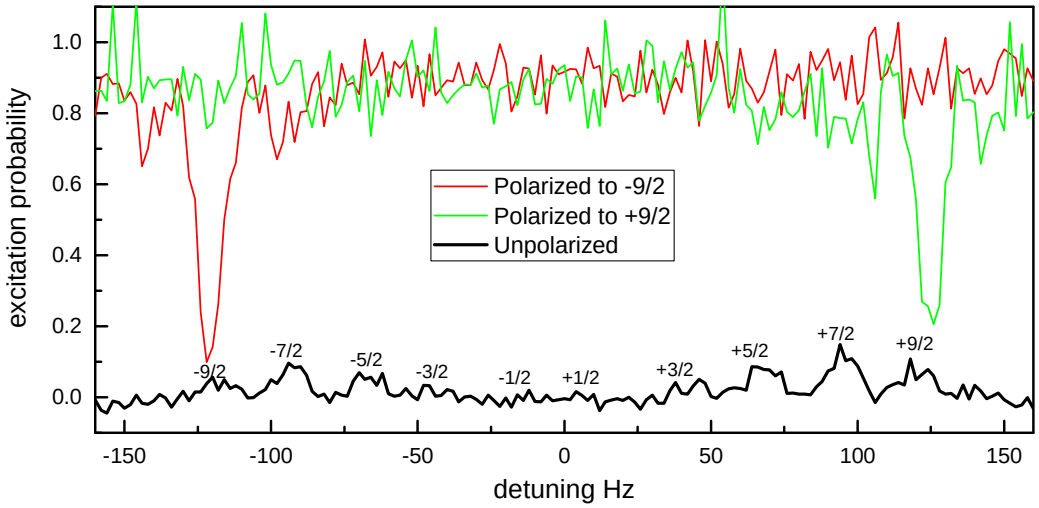

Figure 2.3: Excitation probability on the clock transition with spin polarization (red and green lines) and without spin polarization (black line). A $\pi-$pulse of 50 ms was used in a Rabi interrogation sequence.

Zeeman shift, and AC Stark shift of the lattice laser. In order to overcome this problem, atoms are required to be prepared in a specific magnetic sublevel. According to Eq.(3.12), the first order Zeeman shift can be cancelled out by interrogating two magnetic sublevels with opposite sign, like $m_F = \pm 9/2$ and using the average resonance frequency of the two. Optical pumping is done by driving the transition $|^1S_0, F = 9/2\rangle$ to $|^3P_1, F = 9/2\rangle$ with σ^+ or σ^- light to prepare the atoms in $m_F = +9/2$ or $m_F = -9/2$, respectively. During optical pumping (which takes 20 ms), we apply a small bias magnetic field (few tens of μT) by using MOT coils to generate a homogeneous magnetic field.

In reality, after spin-polarization, some atoms might remain in the other Zeeman sublevels, which can cause an additional frequency shift of the clock transition due to linepulling. In order to remove these atoms, we apply a purification sequence as following: we transfer the atoms in $m_F = +9/2$ into the excited state, $^3P_0$, by applying a resonant, short π-pulse (50 ms, 16 Hz Fourier-limited line width) on the $^1S_0 - {}^3P_0$ transition with large a bias magnetic field of 600 μT to spectrally resolve the different Zeeman components (600 Hz splitting between neighboring Zeeman sublevels). Then, remaining atoms in the ground state are blown away from the trap by a pulse of blue light resonant with the $^1S_0 - {}^1P_1$ transition. then, the interrogation pulse is applied, thus atoms in excited state

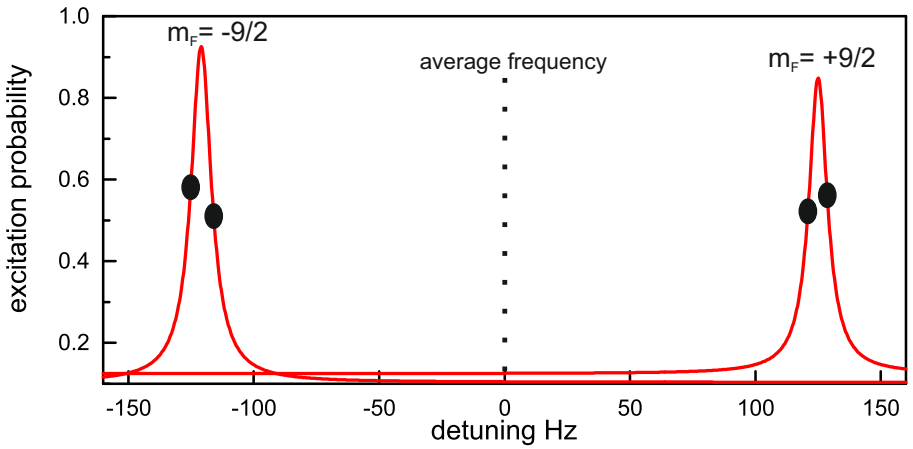

Figure 2.4: Stabilization of the interrogation laser to the clock transition. The sequence consists of four cycles (indicated by the black dots). Two magnetic sublevels, $m_F = \pm 9/2$, are probed to average out the first-order Zeeman shift and each component is probed on both sides (left and right) at the points of maximum slope to determine into which direction the interrogation laser drifts. Thus the average of all four cycles is calculated (vertical dash line).

$^3P_0$ are driven to the ground state with a long π-pulse and the excitation probability is measured by detecting the atoms in both clock states. Figure 2.3 shows the excitation signal of the interrogation for frequency scans across resonance for spin-polarized (red and green lines) and unpolarized samples (black line). The spin-polarization light is derived from the stirring laser with about 20 μW of power and sent to the atomic sample parallelly and anti-parallelly to the quantization axis from both sides (one direction for $m_F = +9/2$ and the second direction for $m_F = -9/2$).

Our new interrogation laser, which is pre-stabilized to a 48 cm-long ULE cavity, allows us to probe the atoms very long (650 ms) Fourier-limited line width of 1.3 Hz is observed. More details on the interrogation laser can be found in [Häf15b, Häf15a].

2.6 Stabilizing to the clock transition

The stabilization principle of the interrogation laser to the atomic transition is shown in Figure 1.1. The excitation probability is used to steer the interrogation laser to the atomic transition. In order to discriminate, in which direction the laser is drifting (lower

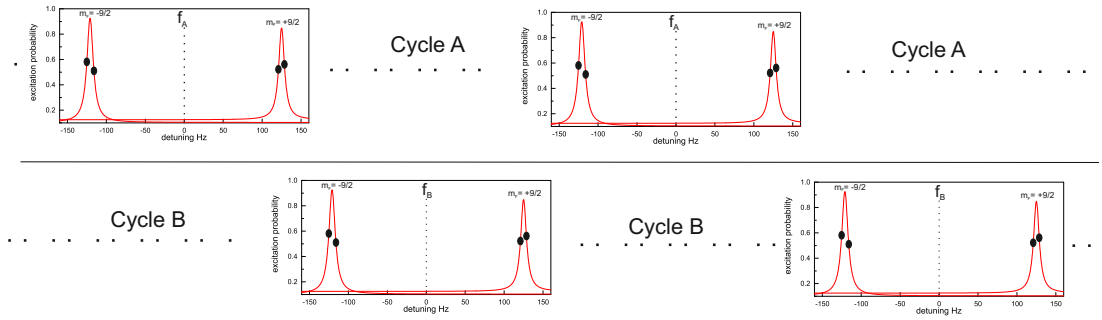

Figure 2.5: The self-comparison scheme (interleaved stabilizations) where the parameter of interest is vary between two values from cycle A to cycle B and the difference frequency $\Delta f = f_A - f_B$ is measured.

or higher in frequency), the interrogation laser probes on the fringe of the clock transition lineshape (Rabi interrogation sequence). It is probed close to the half-maximum points on both sides; new atoms are loaded for each interrogation. The total cycle time consists of a preparation time of 550 ms and an interrogation time of 640 ms. The difference between these excitation probabilities on both sides of the line is used for derive an error signal, which steers the interrogation laser. At the half-maximum points the sensitivity to frequency noise is high, as the full width at half-maximum (FWHM) $\approx 0.8/t_{pulse}$ [Dic88], thus longer clock pulse make the slope steeper.

Other issues that have to be taken into account for stabilizing the interrogation laser to the clock transition are that atoms in presence of a magnetic field will be subject to a Zeeman shift. The first order Zeeman shift can be averaged out easily with fermionic atoms, like ^{87}Sr atoms, where two magnetic sublevels are probed instead of one. In our case, we probe $m_F = \pm 9/2$, thus according to Eq.(3.12) the first order Zeeman shift is averaged out.

Figure 2.4 shows the normal operation of the clock, which consists of four cycles for probing the two magnetic subelevel $m_F = \pm 9/2$. The frequency shifts to address the $m_F = \pm 9/2$ sublevels are introduced by the AOM used to pulse the light of the interrogation laser. After each of four cycles the error signal is derived and fed back to the frequency of the AOM between the interrogation laser and the cavity. This sequence is referred to as single operation (or normal operation), which is used for example, in absolute frequency measurements, and ratio measurements against other clocks.

Lastly, the clock has to be characterized and all frequency shifts of the clock transition should be measured, or estimated, and corrected. In order to do so, the parameter of interest is varied, and we measure the corresponding frequency shift. For that a stable reference over the time of measurements is required. Unfortunately there no sufficiently a stable reference is variable (although our transportable Sr lattice clock was recently used as a reference, but is still under improvement). The problem is solved by performing a self-comparison, where the parameter of interest is varied between two values and the difference of the frequencies between them is measured. This method does not require an external stable reference, but relies on the short term stability of the interrogation laser. We have used this method to measure the magic wavelength of the lattice laser, collision shift, DC stark shift, etc. This method requires two independent servo loops. Figure 2.5 schematically shows two independent servo loops on the same experiment (one clock), where an experimental parameter is varied between two values, for example for in magic wavelength measurements, the intensity of the lattice laser is varied between two intensities (shallow and deep lattice) and the frequency difference between them is measured.

Chapter 3

Systematic uncertainty of the clock

The accuracy of optical clocks, based on either many neutral atoms or a single ion, has surpassed the Cs primary frequency standards since almost a decade ago [Lud08a, Lor08]. Nowadays, optical clocks achieve two orders of magnitude better than the Cs primary frequency standards [Nic15, Hun16]. The reasons for that is that, optical clocks operate at a frequency about five orders of magnitude higher than cesium clocks, which make fractional frequency shifts of optical clocks much much smaller than cesium clocks (for example, if $\delta\nu = 1$ Hz then, this leads to $\frac{\delta\nu}{\nu_{optical}} \ll \frac{\delta\nu}{\nu_{microwave}}$). Moreover, ion clocks are insensitive to the environments surround the ion, meaning the shift due to interaction between the ion and the environment is small and their uncertainty will be even smaller. In case of neutral optical lattice clocks, improving the knowledge on how the neutral atoms like strontium atoms interact with their environment over a decade has allowed us to push the accuracy of the neutral lattice clock beyond the Cs primary frequency standard and to the level of ion clocks. Moreover the instability of optical lattice clock is two orders of magnitude better than that of the Cs primary frequency standard (see next chapter), which allows us to perform very accurate measurements of the systematic shifts of the clock transition within very shot time. The observed frequency $\nu_{observed}$ is always equal to the atomic frequency ν_0 plus (or minus) some additional shift $\delta\nu$. The additional shift is not zero because the atom in general, and clock states in particular are not isolated 100 % from the environment surrounding the atomic sample, e.g., magnetic fields, electric fields, temperature, laser light, etc. All these additional shifts (systematic shifts) must be measured individually and the observed frequency needs to corrected in order to derive

the frequency of the unperturbed transition. The correction has an uncertainty due to the uncertainties associated with each individual correction procedure. The total uncertainty of an atomic clocks is then derived from all relevant contributions (more details on how we derived the uncertainties will be clear later on).

In atomic clock experiments, usually atoms (namely the clock transition) are interrogated at the position where they are cooled and trapped, which we call 'the MOT position'. The atoms in the MOT position have been characterized and the systematic shifts of the clock transition have measured individually, like AC Stark shift, collision shift, BBR shift, etc. The MOT position is not necessary the best position for spectroscopy, thus for better control systematic shifts, atoms are needed to move to somewhere else inside the vacuum chamber for spectroscopy.

In this chapter I will give details on the systematic shift with their uncertainties at the MOT position and then I will present how the BBR uncertainty has been reduced by order of magnitude by interrogating the atoms inside a well controlled environment (22 mm away from the MOT position) at cryogenic temperature, which we call it the coldfinger.

3.1 MOT position

In this section, I will present all systematic shifts and their uncertainties of the clock transition ($^1S_0 - {}^3P_0$) at the MOT position. many of these shifts are well understood and they have negligible contribution to the uncertainty budget of the clock but few of them still limited the accuracy of the clock.

3.1.1 Introduction of BBR shift

Blackbody radiation [Gal79, Ita82] is an electromagnetic field that is created by the emission of the blackbody, where the electric field E of a Blackbody with temperature T can be written by Planck's law [Saf10]

$$E^2(\omega)d\omega = \frac{8\alpha}{\pi}\frac{\omega^3 d\omega}{\exp(\frac{\omega}{K_B T}) - 1}. \tag{3.1}$$

The BBR shift of the clock transition is produced due to the difference in the energy shift of the clock states due to interact with the thermal radiation, thus the energy difference shift between the clock states can be written by integrating over the BBR spectrum as

$$\Delta E = \frac{1}{4h\epsilon_0\pi^3c^3}\int_0^\infty \Delta\alpha(\omega)\frac{\omega^3 d\omega}{\exp(\frac{\omega}{K_BT})-1}, \tag{3.2}$$

where $\Delta\alpha(\omega)$ is the polarizability difference between the clock states, where the polarizability of a state can written as following

$$\alpha_i(\omega) = \frac{2}{3\hbar}\sum_{i\neq j}|\langle i\,\|D\|\,j\rangle|^2\,\frac{\omega_{ij}}{\omega_{ij}^2-\omega^2}, \tag{3.3}$$

where $\langle i\,\|D\|\,j\rangle$ is a reduced electric dipole matrix element between states i and j. And ω_{ij} is the transition frequency and ω is the frequency of the BBR.

In our case, the ground state is $^1S_0$ where the nearest electronic transition is $^1P_1$ which is far away from the BBR spectrum, thus the polarizability of the ground state can be considered independent of frequency (the static polarizability can be consider). The excited state is $^3P_0$, where the transition $^3P_0 - {}^3D_1$ is covered by the BBR spectrum, thus it cannot be ignored. The dynamic terms must be consider in addition to the static term. The total energy shift can be written as [Deg05]

$$\Delta E(T) = -\frac{\Delta\alpha_{\text{static}}}{2}\left\langle E^2\right\rangle - \frac{\hbar}{2\pi}\left(\frac{K_BT}{\hbar}\right)^3\sum_k \frac{2J_k+1}{2J_i+1}\frac{A_{ki}}{\omega_{ik}^3}G\left(\frac{\hbar\omega_{ik}}{k_BT}\right), \tag{3.4}$$

where the first term in Eq. (3.4) describes the static energy shift difference of the clock states. $\Delta\alpha_{\text{static}}$ is the static polarizability difference of the clock states and $\langle E^2\rangle$ is the mean squared value of the electric field at temperature T, which is calculated by the energy density of the BBR according th the Stefan-Boltzmann law [Ita82],

$$\left\langle E^2\right\rangle = \frac{\rho}{\epsilon_0} = \frac{8\pi^2K_B^4}{15_0^3\epsilon_0h^3}T^4. \tag{3.5}$$

The second term in Eq. (3.4) describes the dynamic shift, which includes all possible electric-dipole transitions from state i to the states k with respective Einstein coefficients A_{ki} and transition frequencies are weighted by the function $G(y)$, which is the integral of

Atoms and ion	Transition	$\frac{\delta\nu}{\nu_0}$	Uncertainty	Reference
$^{171}Yb^{+}$	$^2S_{1/2} - {}^2F_{7/2}$	-70.5×10^{-18}	1.8×10^{-18}	[Hun16]
Al^{+}	$^1S_0 - {}^3P_0$	-9×10^{-18}	6×10^{-18}	[Cho10]
^{87}Sr	$^1S_0 - {}^3P_0$	-4572.3×10^{-18}	1.4×10^{-18}	[Nic15]
^{171}Yb	$^1S_0 - {}^3P_0$	-2600×10^{-18}	1×10^{-18}	[Por06, Bel14]

Table 3.1: The table shows the BBR shift at room temperature for different atoms and ions with their uncertainty.

the off-resonant energy denominator over the BBR spectrum [Far81],

$$G(y) = \int_0^\infty \frac{x^3}{e^x - 1}\left(\frac{1}{y-x} + \frac{1}{y+x} - \frac{2}{y}\right) dx \approx \frac{16\pi^6}{63y^3}, \tag{3.6}$$

where $x = \hbar\omega/K_BT$ and $y = \hbar\omega_{ik}/K_BT$. The total frequency shift due to BBR can be written as following

$$\Delta\nu_{BBR} = \Delta\nu_{Static} + \Delta\nu_{Dynamic} = -\frac{\Delta\alpha_{Static}}{2h}\left\langle E^2\right\rangle - \frac{(\delta E_e(T) - \delta E_g(T))_{Dynamic}}{h}. \tag{3.7}$$

where $\Delta\nu_{Static}$ and $\Delta\nu_{Dynamic}$ static and dynamic contribution and e and g are ground and excited state of the transition of interest, in our case the $^1S_0$ and $^3P_0$ states. The Eq. (3.7) can be written in better way as,

$$\Delta\nu_{BBR} = \Delta\nu_{Static}\left(\frac{T}{T_0}\right)^4 + \Delta\nu_{Dynamic}\left(\left(\frac{T}{T_0}\right)^6 + \mathcal{O}\left(\frac{T}{T_0}\right)^8\right). \tag{3.8}$$

T_0=300 K and T is the temperature of the surround environment of the atoms.

Table 3.1 shows the BBR shift for different kinds of atoms and ions; For example, the Al^{+} ion has the lowest BBR shift, this is due to the fact that the polarizabilities of the clock transition states in presence of BBR are almost the same, thus the difference between them is very small. The situation is different with neutral atoms, specially Sr and Yb atoms, where the BBR shift is large because the polarizabilities of the clock transition states in present of BBR spectrum are different, thus the difference between the clock states is large. Figure 3.1 shows the polarizability of the clock states $^1S_0$ and $^3P_0$ as a function of frequency and, additionally, the power spectral density of BBR at $T = 300$ K. This has been the main disadvantage of optical clocks based on neutral atoms [Por06] but nowadays, BBR shifts for neutral Sr and Yb atoms have been measured and characterized

very accurately as seen in Table 3.1.

The uncertainty of the BBR shift stems from two sources; the first source is the atomic response to the BBR (the sensitive of the atom to the BBR). The sensitivity depends on the atomic properties. The atomic response is represented by the BBR shift coefficients ν_{static} and $\nu_{dynamic}$. In our group, my colleague Thomas Middelmann [Mid12a, Mid13] has measured the static shift coefficient with an uncertainty below 10^{-18} at room temperature by measuring the differential dc polarizability of the two clock states. This measurement has been done in our apparatus by installing a precision capacitor and measuring the BBR shift as a function of applied voltage to the capacitor; more details on this measurement are found in [Mid12a, Mid13]. The dynamic shift arises from coupling to the transition $^3P_0 - {}^3D_1$ which is spectrally overlap with the BBR. The uncertainty of the dynamic shift has been reduced in our group by a modeling of the dynamic shift by using new accurate value for static shift coefficient in combination with other observables, thus the dynamic shift uncertainty is reduced to level of 5×10^{-18} at room temperature (more details in [Mid12a, Mid13]). Recently the dynamic shift has been measured in Jun Ye's group at JILA with an uncertainty of 1.4×10^{-18} by measuring the life time of the $^3D_1$ state [Nic15].

The second part of the uncertainty stems from the BBR field itself, meaning how accurate we measure the temperature seen by atoms. One of the difficult task is to measure the temperature very accurately, on the level of few mK at room temperature. Figure 3.2 shows the uncertainty of the BBR shift as a function of temperature for different uncertainties of the temperature. The black solid lines are the uncertainties due to our knowledge of the atomic response (both static coefficient ν_{static} and dynamic coefficient $\nu_{dynamic}$). The red solid line shows the uncertainty of the BBR shift as a function of the temperature for 1 K uncertainty; at room temperature (300 K) this leads to uncertainty of 7×10^{-17}. At 80 K, it leads to an uncertainty of 1×10^{-18}. From this it is very clear what is the requirement to operate the system with BBR accuracy of 1×10^{-18} or below; the first option at room temperature, the requirement is to measure the temperature seen by atoms very accurately with less than 10 mK. The second option is to operate the system at low temperature (below 100 K). This will reduce the BBR shift itself and thus its uncertainty as well and relax the necessity to measure the temperature very accurately (1 K uncertainty at low temperature will be sufficient to reach BBR accuracy in level of 1×10^{-18}), as seen in the Figure 3.2.

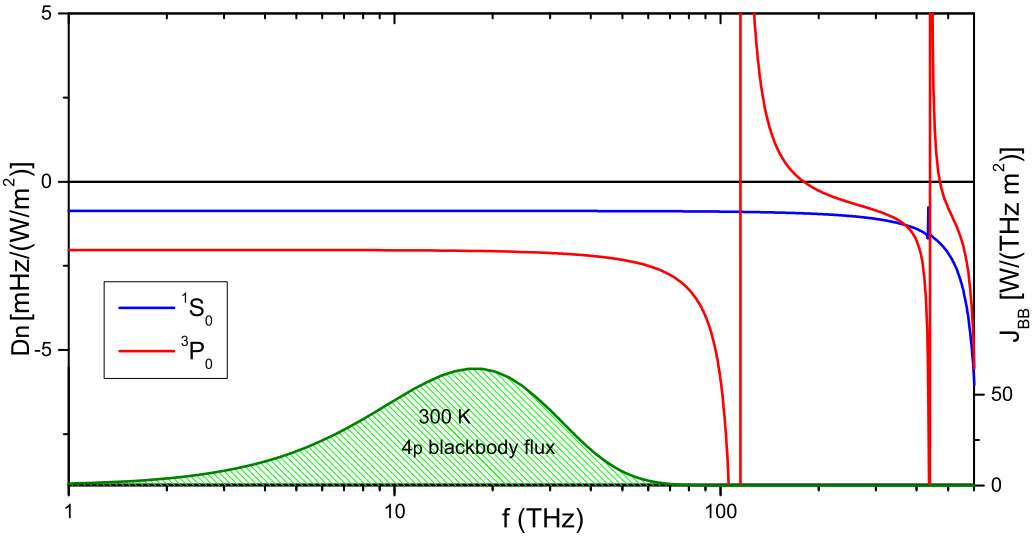

Figure 3.1: Polarizability of the clock states as a function of frequency (red and blue lines). The green solid line shows the flux of BBR field at T= 300 K. At low frequencies, the differential polarizability $\Delta\alpha$ is constant over the BBR spectrum and additional a weak transition $^3P_0 - {}^3D_1$ at around 115 THz.

3.1.2 Uncertainty of BBR shift in our system

At the MOT position, The largest frequency correction and uncertainty to the clock transition is due the BBR shift. At the MOT position we can operate only at room temperature (300 K), thus larger BBR shift has to take into account about -2.1 Hz. For the uncertainty of the BBR shift, as I mentioned previously the atomic response to BBR is known very well better than 2×10^{-18} at room temperature but we lack of the temperature knowledge at the MOT position. We cannot measure the temperature very accurately at the MOT position. We estimate the effective temperature seen by the atoms by measuring the temperature across the entire vacuum chamber by several PT100 temperature sensors and determining hottest and coldest points. Without further knowledge on the thermal system, we assume a rectangular probability distribution for the representative temperature be between hottest and coldest point. Thus, according to BIPM's GUM (Guide to the Expression of Uncertainty in Measurements) [GUM08], the representative temperature can be written as following,

$$T_{\text{rep.}} = \frac{T_{\text{hottest}} - T_{\text{coldest}}}{2}, \tag{3.9}$$

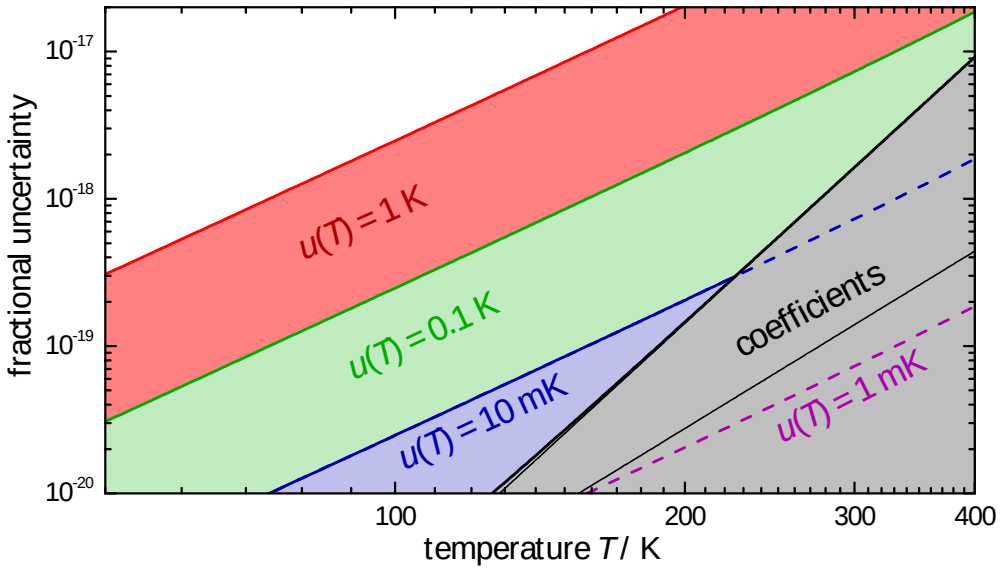

Figure 3.2: Uncertainty of the BBR shift as a function of temperature for different temperature uncertainties. The uncertainty of atomic response (static ν_{static} and dynamic coefficients $\nu_{dynamic}$) are also plotted for completeness (black solid lines). The red solid line shows the uncertainty of the BBR shift as a function of the temperature for 1 K uncertainty. The green solid line is shown with uncertainty of 100 mK, and blue solid line with uncertainty of 10 mK, and violet dash line with 1uncertainty of 1 mK of the temperature.

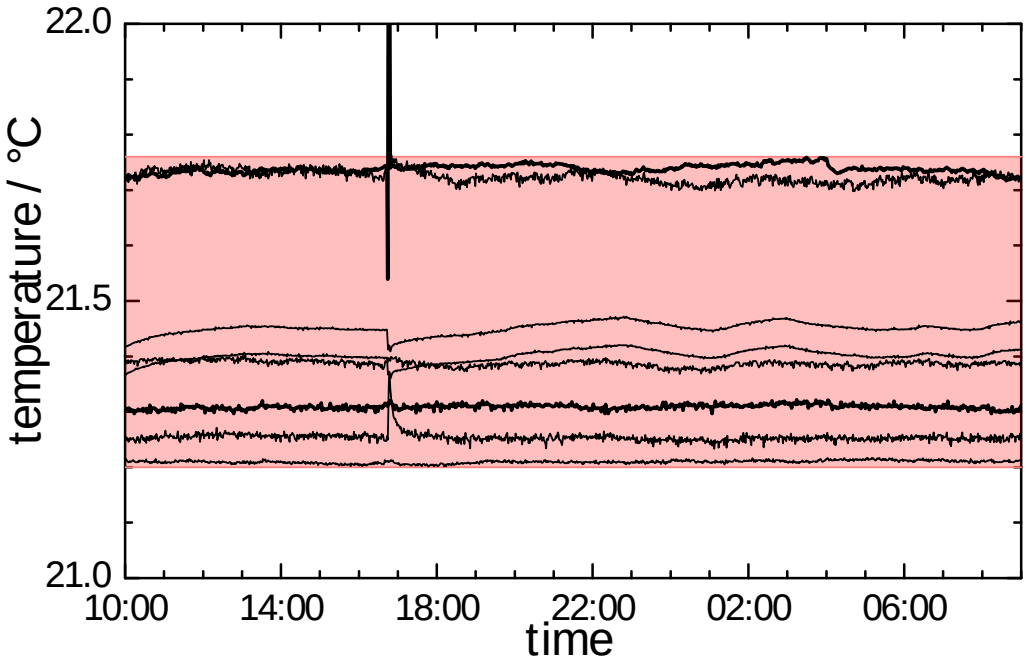

Figure 3.3: This figure is shown the temperature reading of the PT100 sensors cross the vacuum chamber during the measurements.

and the uncertainty of the the temperature is

$$u(T_{rep.}) = \frac{T_{hottest} - T_{coldest}}{\sqrt{12}}. \tag{3.10}$$

Additional care has been taken to avoid undesired heat sources, the Zeeman slower is water cooled and stabilized within 0.1 K. All magnetic field coils are water cooled. Moreover during some measurements we add 1 s dead time between the cycles (where all coils are switch off) to reduce the heat load, adding the dead time will degraded the stability of the clock, thus we add this dead time only during the measurements where is not required high stable clock (for example, during the ratio measurements against $^{171}Yb^{+}$ ion clock). The temperature gradient between hottest and coldest points during the operation is 600 mK, as seen in Figure 3.3. Thus the BBR shift has uncertainty of 1.3×10^{-17}, which is limited by the uncertainty of the temperature seen by atoms.

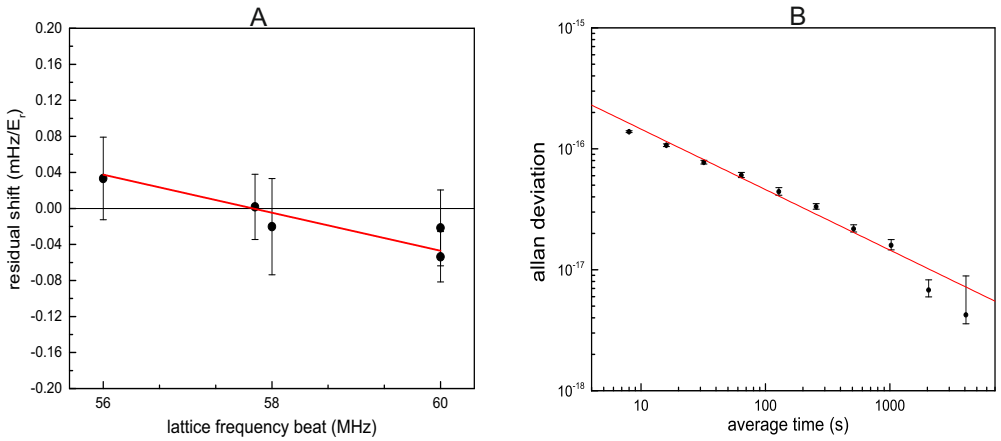

Figure 3.4: The residual shift of the clock transition for interleaved measurements. A) shows the residual shift as function of lattice frequency with lattice depth modulated between 71 E_r and 143 E_r. B) shows typical instability of the interleaved measurements, the red solid line shows instability of $4.6 \times 10^{-16}/\sqrt{\tau}$.

3.2 Other effects

During this subsection, I will discuss all other systematic shift that may shift the clock transition from its unperturbed frequency. These systematic shifts must be measured and corrected very accurately. Most of the systematic shifts can be measured by the clock itself by self-comparison of the clock, i.e., using so-called interleaved stabilizations (see 2.6). I will present systematic shifts due to lattice light, DC stark, first and second-order Zeeman, collisions, line pulling, tunneling, interrogation laser, optical path length error, and servo error.

3.2.1 Lattice light shift

A neutral atom in presence of an electric field of the laser will polarized, which leads to an energy shift of the state of interest, which called AC Stark shift. It can be written as

$$\Delta\nu = -\frac{1}{2h}\alpha_i |E|^2 \tag{3.11}$$

where α_i is the polarizability of the state of interest (and it can be written as the sum of three polarizabilities, scalar, tensor and vector) and E is the amplitude of an electric field of the laser. The AC Stark shift was a big challenge to controlled until Katori [Tak03]

proposed the concept of a magic wavelength in 2003, where the two clock states, $^1S_0$ and $^3P_0$, are shifted by the same amount and thus the differential AC Stark shift due to the laser vanishes for these states. This kind of cancellation is only valid for the first order shift (linear dependence on laser intensity). Higher order shifts (hyperpolarizability, quadratic-dipole transition (E2) and magnetic-dipole transition (M1)) have to be taken into account and controlled carefully to reach an accuracy of 10^{-18}, details on the theoretical calculations of the magic wavelength can be found in [Kat09, Guo10, Boy07a]. The magic wavelength is measured by the interleaved stabilization method, where the frequency of the lattice laser is stabilized to a frequency comb which is referenced to the H-Maser. Then the intensity of the lattice laser is modulated between two values (in our case typically between 71 E_r and 143 E_r). The observed frequency shift of the difference between two stabilization sequences is recorded and the observed shift is corrected from the residual shift due to the hyperpolarizability, collisions, tunneling and then the corrected frequency is normalized to the average lattice intensity which atoms experience. Such measurement is repeated for different lattice frequencies to determine the zero crossing for the first order Stark shift (due to scalar and tensor polarizabilities) as seen in Figure 3.4. We find the magic frequency in our lattice laser is 368554465.0 (3) MHz. 3 MHz uncertainty of the magic lattice frequency causes 9×10^{-18} fractional uncertainty of the first order Stark shift due to scalar and tensor polarizabilities. This uncertainty arises from statistical, hyperpolarizability, tunnelling and collision, which are added in quadrature. The shift due to vector polarizability is averaged out since we interrogate both $\pm 9/2$ m_F components and the vector shift depends linearly on m_F.

The correction and uncertainty of the higher order shifts (hyperpolarizability, quadratic-dipole transition (E2) and magnetic-dipole transition (M1)) have been estimated. We estimated the shift due to hyperpolarizability for our lattice depth, using the coefficient from [Wes11], which is $0.45(10)\mu\text{Hz}/E_r^2$ and the thermal average of the lattice depth of 57 E_r. This leads to a shift of 4.8×10^{-18} with an uncertainty of 1.8×10^{-18} including 20% uncertainty of the lattice intensity seen by atoms. Electric-quadrupole (E2) and magnetic dipole (M1) light shifts were first discussed in [Tai08] for $J = 0$ to $J = 0$ transitions. We follow the upper limit given in [Wes11], which gives rise to a shift is smaller than ± 0.31 mHz $/\sqrt{E_r}$. This leads to an actual uncertainty of 3.4×10^{-18}.

3.2.2 DC Stark shift

DC electric fields cause a shift of the clock transition. The Sr lattice clock group in LNE-SYRTE group found huge DC stark shift due to patch charges accumulating on the build-up lattice's cavity mirror [Lod12]. In our group, we found in 2013 that the magnetic field coils of the MOT were not grounded but set to a voltage of about 21 V and between the coils, there was a capacitor which was grounded (the capacitor was using for [Mid12a]). The residual DC Stark shift cause by 21 V is -1.52×10^{-16} measured experimentally by interleaved stabilization between 21 V and 0 V applied to the coils, this shift had to be taken into account in a previous absolute frequency measurement [Fal14]. The problem is solved by setting the MOT coils to GND potential. We have measured if there is any residual DC Stark shift by applying deliberate electric potential to the electrodes near the atomic sample (MOT coils, capacitor, other electrode) and measuring the influence on the clock transition as a function of the applied potential. We have observed a parabolic dependence, since the DC Stark shift is proportional to the square of the electric field. The projection of the remaining stray electric field is determined by the offset of the parabola from zero applied electric potential. In order to estimate the absolute value of the remaining stray field, we have measured the projection of the remaining stray field at three different configurations by the electrodes near the atomic sample and the angle between them must be determined. To determine the angle between them, we have measured three other projections while applying a known electric field with one of the other two electrodes (for example, one of these measurements is done by applying 20 V on the capacitor and measuring the influence on the clock transition as a function of the applied potential on the MOT coils) and comparing the applied field strength with the observed projection of this field. The residual electric field is found to be 15.8(22) Vm^{-1}, this field is due to a voltage difference of 0.7 V between the MOT coils which caused by a protection diode in the electrical connection between them. The residual shift is very small (negligible) and has uncertainty of 3×10^{-19}.

3.2.3 First and second-order Zeeman shift

The energy of the atomic level changes in presence of a magnetic field [Lur62]. The shift depends on the properties of the atomic structure, namely the Landé factor of the states.

In case of the first order Zeeman shift, if the Landé factors of the clock states are equal, then there is no first order Zeeman shift on the clock transition (like in the case of pure LS states). Unfortunately, our clock states have different Landé factors due to hyperfine mixing of the upper state [Boy07c], thus the linear Zeeman shift has be taken into account. The first order shift can be written,

$$\Delta_B^{(1)} = \delta g \mu_B m_F B/h, \tag{3.12}$$

where δg is the difference between the Landé factors of clock states, μ_B is the Bohr magneton, m_F the magnetic sublevel of the clock states, B the magnetic field and h Planck's constant. The first-order Zeeman shift is averaged out in our case since we stabilized our clock to the average frequency of the Δm_F= 0 Zeeman transitions from levels $\pm$9/2 mF, where the first-order Zeeman shift for magnetic sublevels $\pm$9/2 mF with present of a homogenous magnetic field is equal but opposite sign and taking the average of the two such transition ($\pm$9/2 mF) gives an effective transition frequency which has no first-order Zeeman shift.

For the second-order Zeeman shift, using a homogenous magnetic field during the spectroscopy will introduces a second-order Zeeman shift which is cannot be removed as in first-order Zeeman shift. The second-order Zeeman shift arises from levels splitting in energy due to the fine-structure splitting, the second-order Zeeman shift is dominated by the interaction of the $^3P_0$ and $^3P_1$ states. The second order Zeeman shift can be written as following,

$$\Delta_B^{(2)} = -\frac{2\alpha^2\mu_B^2}{3h^2(\nu(^3P_1) - \nu(^3P_0))}B^2 = aB^2. \tag{3.13}$$

Where α is the coupling coefficient between $^1P_1$ and $^3P_1$ states due to the spin-orbit coupling. $(\nu(^3P_1) - \nu(^3P_0))$ is the frequency difference between the $^3P_0$ and $^3P_1$ states. The quadratic coefficient (a) has been measured in the same way as previous measurement [Fal11] with better accuracy, the quadratic coefficient is found to be $a = 0.228(2)\text{Hz/G}^2$ which has good agreement with other group [Boy07c,Wes10a]. During the clock operation, a bias magnetic field is applied (few tens of μT). The bias magnetic field split the $m_F \pm$ 9/2 components by 240 Hz, the splitting tells us how much magnetic field is experienced by the atoms. From the splitting and the quadratic coefficient we have calculated the

second-order Zeeman shift to be -3.2×10^{-17} (fractional shift) with an uncertainty of 1.3×10^{-18}.

3.2.4 Collisional shifts

Cold collisions shift

Interactions between cold atoms can cause an additional shift. This collision shift has been measured in our system by an interleaved stabilization, one running at low atom number and the second with high atoms number which is done by using different loading time of the blue MOT. Finally. We have varied atom number by factor of 10 between low and high atom number. The frequency difference between them has been measured and there is not a significant shift is observed, the observed frequency shift is consistent with zero with uncertainty of 0.8×10^{-18}.

Background gas collision shift

Remaining background gas atoms in the main vacuum chamber could cause an additional shift to the clock transition. This shift has to take into account during the evaluation of the uncertainty budget of the clock. The background gas collision shift has been calculated in our group in [Fal14]. It has been re-calculated (similar way as in [Fal14], by using Eq.(3) in [Gib13] but without applying the approximation which has been used in [Gib13] for ΔC) for new evaluation of the clock, taking into account new vacuum pressure for our chamber (new lattice life time) and the dispersion coefficients C_6 between the background gases like (H, He, H_2, S_r, and Xe) and clock states, which is listed in table 3.2. From this calculation, we put an upper limit of the background gases fractional frequency shift to be $0(4) \times 10^{-18}$.

3.2.5 Line pulling shift

We use spin-polarized atoms to probe the clock transition, namely $m_F = \pm 9/2$ ^{87}Sr atoms. The line pulling is arise due to: First, there may be residual atoms in $m_F = \pm 7/2$ and it can be off-resonantly excited, which leads to an asymmetry of the observed

atom and molecules	C_6 (au) for $^1S_0$	C_6 (au) for $^3P_0$
H	119.0	150
He	43.76	50.85
H_2	114.86	131
X_e	749.5	891.2
S_r	3150	4100

Table 3.2: Some of the dispersion coefficients C_6 between some background gases and the clock states from [Mit10].

clock transition line and causes shift of the observed line center. The population of the $^3P_0, m_F = 7/2 - {}^1S_0, m_F = 7/2$ transition is measured experimentally, which is less than 5% and the splitting between magnetic sublevlel is known, thus the line pulling shift is determined.

Second: Line pulling may also arise due to imperfect polarization of the clock laser. If it is not exactly parallel to the quantization axis, e.g., due to birefringence of the viewports, or a tilt of the polarization axis. The resulting π-polarized light will couple not only $^3P_0, m_F = 9/2 - {}^1S_0, m_F = 9/2$ transition, but also the $^3P_0, m_F = 9/2 - {}^1S_0, m_F = 7/2$ transition. The $^3P_0, m_F = 9/2 - {}^1S_0, m_F = 7/2$ transition is expected to be 45 Hz higher than the $^3P_0, m_F = 9/2 - {}^1S_0, m_F = 9/2$ transition (depends on the experimental parameters). We have measured the population of this transition by performing several high-resolution scans cross the transition and thus upper limit of a fractional power in the σ-polarization is derived to be less than 10%. Then the time-dependent Schrödinger equation of the the three state system is integrated and an upper limit for the line pulling is derived. We put an upper limit of the total line pulling shift to be $0(1) \times 10^{-19}$.

3.2.6 Tunneling shift

Atoms in a periodicity of the trapping potential are subject for tunneling from site to site [Lem05]. The clock transition can be shifted from the atomic transition frequency by order of the bandwidth, when clock transition is probed, the transition frequency shift is depended on the bandwidth and qusimonetum q (with a period of $2k$). Moreover, the finite bandwidth of the vibrational states causing a line broadening. Both of these effects depend on the amount of the bandwidth (for example, for a horizontal lattice with depth of 80 E_r, the bandwidth of the lowest vibrational states are 13 mHz and 826 mHz), thus,

it is important to reduce the bandwidth and to keep the atoms in the lowest vibration state.

Our lattice trap, we avoid the population with $\nu > 0$ by the filtering procedure, where the lattice depth ramps down for 40 ms from 73 E_r to 40 E_r to allowing hottest atoms with $\nu > 0$ leave the trap and then the lattice depth ramp back to 73 E_r. The population of the vibrational states have been measured experimentally by sideband spectra; 4% of the atoms were found in the first axially excited state and zero population was found in the second state. Moreover, our lattice trap is nearly horizontal with a tilt of $\theta = 0.12(5)^\circ$, which causes an energy difference between neighboring sites of 2.4 Hz, thus reducing the bandwidth according to [Sia08]. We estimated the fractional frequency shift due to the tunneling to be 2×10^{-18}, which is added as an uncertainty only.

3.2.7 Interrogation laser shift

The interrogation laser light may introduce a frequency shift of the clock transition by coupling to other excited states when atoms interact with the interrogation light. Our new interrogation laser [Häf15b] allows us to interrogate the atoms for as long as 640 ms and thus with very little power in the nW range. We have determined the frequency shift caused by the interrogation laser by measuring the light intensity and using the coefficient -13(2) Hz$(\mathrm{Wcm}^{-2})^{-1}$ from [Hai07], we found the frequency shift due to the interrogation laser is less than 1×10^{-19}, which is added as uncertainty only.

3.2.8 Optical path length error shift

In our system, the interrogation laser is 12 m away from the atoms. The interrogation light is transferred via a single mode (polarization maintaining) fiber. Since any changes of the optical path length due to vibration of the lattice mirror or AOM chirp can cause a frequency shift. The optical path length has to stabilized. One advantage of the lattice clock is that the atoms have a fixed distance to the mirror that used to produce the standing wave of the lattice trap, this mirror can be used as a reference for optical length stabilization. This technique has been investigated in detail in our group [Fal12]. Based on the current experimental parameters (especially the longer clock pulse), the

uncertainty contribution of the optical path length stabilization is 1×10^{-19}, which is added as uncertainty only.

3.2.9 Servo error shift

The interrogation laser is referenced to an external cavity for pre-stabilization. The drift of the cavity due to aging causes an undesired frequency shift of the clock transition. This shift has to taken into account. The cavity drift is removed by drift compensation using a sweep AOM frequency. The drift cavity is changed by $\beta\nu_{err}/\tau_{cycle}$, where β is the drift cavity gain, ν_{err} is the frequency offset, and τ_{cycle} is the cycle time. The time constant for settling drift rate can be written as in [Fal11],

$$\tau_{constant} = \frac{-\tau_{cycle}}{\mathrm{In}(1-\frac{\beta}{\mathrm{G}})} \Longrightarrow \tau_{cycle}\frac{G}{\beta} \quad \mathrm{for}(\mathrm{G} >> \beta), \tag{3.14}$$

where G is the lock gain, in our system, the cycle time $\tau_{cycle} = 4 * 1.18$ s, $G = 0.5$, and $\beta = 0.02$, which lead to time constant of 118 s. The frequency servo error $\nu_{(servo\ err)}$, for a cavity due to a residual change of the drift rate $\ddot{\nu}_{cav}$, is determined by assuming that the correction of the drift rate is equal to the change in the cavity drift within lock cycle time as written in [Fal11],

$$\ddot{\nu}_{cav}.\tau_{cycle} = \frac{\beta}{\tau_{cycle}}\nu_{(servo\ err)} \Longrightarrow \nu_{(servo\ err)} = \ddot{\nu}_{cav}\frac{\tau_{cycle}^2}{\beta}. \tag{3.15}$$

The servo error $\nu_{(servo\ err)}$ is calculated, for the new interrogation laser, which is stabilized to a 48 cm long ULE cavity that has a $\ddot{\nu}_{cav} = 2 \times 10^{-7}$ Hz/s^2, to be zero with an upper limit uncertainty of 1.7×10^{-18}.

3.3 Summary

The Table 3.3 shows the uncertainty budget at the MOT position for last two evaluations 2012, 2015. The systematic uncertainty has been improved in 2015 by more than factor of two comparing with that in 2012 due to following; first the uncertainty due to BBR shift has been reduced by reducing the temperature gradient from 1.78 K (2012) to 600

	MOT position (2012)		MOT position (2015)	
Effect	Correction (10^{-18})	Uncertainty (10^{-18})	Correction (10^{-18})	Uncertainty (10^{-18})
BBR shift	4924	36	4929	12.8
BBR oven	16	12	9.4	9.4
lattice scalar and tensor	0	9	-7	9
lattice E2/M1	0	6	0	3.4
hyperpolarisability	-5	2	-4.8	1.8
second-order Zeeman	-32	1.3	-32	1.3
cold collisions	0	5	0	0.8
background gas collisions	1.5	1.5	0	4
tunneling	0	1	0	2
line pulling	0	0.3	0	2
interrogation laser	0	1	0	0.1
optical path length error	0	0.8	0	0.1
servo error	0	0.3	0	1.7
dc Stark shift	152	33	0	0.3
total	5120	52	4894.6	19.1

Table 3.3: Total uncertainty budget for MOT position for evaluations 2012, and 2015. All systematic frequency shifts are listed here with their uncertainties.

mK (2015) (see section 3.1.2 for more details). The second, we found, during the absolute frequency measurement in 2012 that the magnetic field coils of the MOT were not grounded but set to a voltage of about 21 V and between the coils, which caused a DC Stark shift of -1.52×10^{-16} with uncertainty of 3.3×10^{-17}. The problem is solved by setting the MOT coils to GND potential, thus suppress the DC Stark shift to $0(3) \times 10^{-19}$ (more details in section 3.2.2).

The evaluation of 2015 shows that, the uncertainty due to the BBR shift is still the largest one, limited by the uncertainty of the temperature seen by atoms. In order to suppress the uncertainty of the BBR shift further, The temperature seen by atoms has to measure accurately by more than factor of ten better at room temperate or operate the clock at cryogenic temperature. Unfortunately both of these options are impossible in the MOT position. In order to overcome this problem, we designed a control temperature environment (we call it 'cold finger') and installed it close to (22 mm away) the MOT position, where the atoms can be transport and interrogate inside the cold finger, more details on the cold finger in the next section.

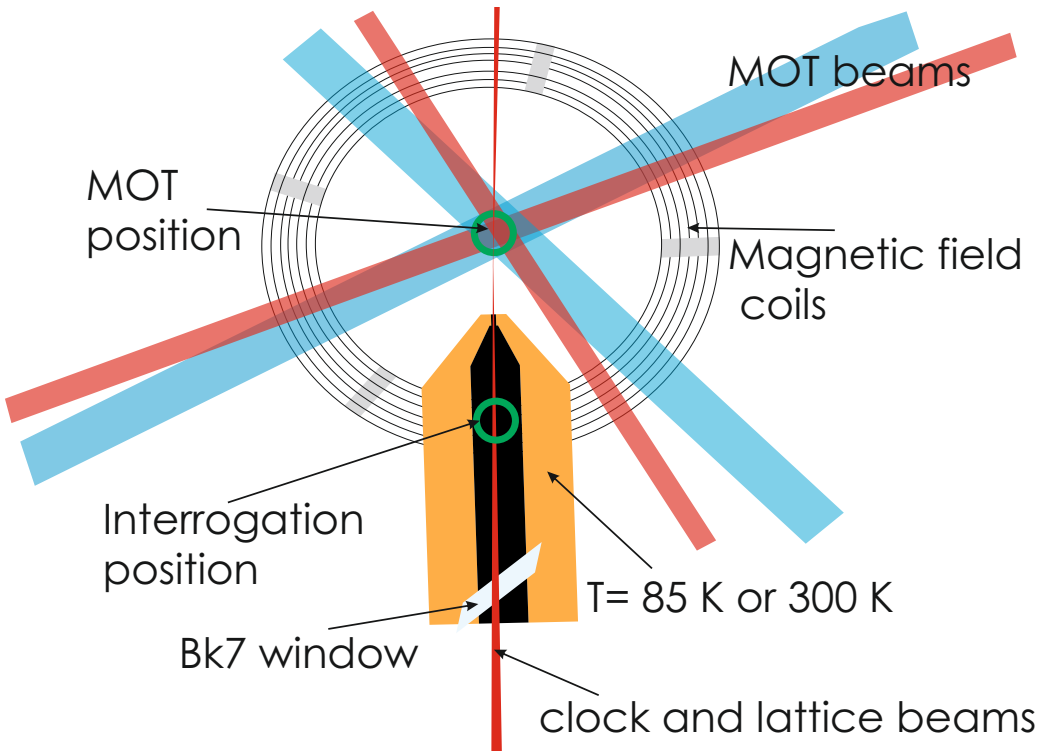

Figure 3.5: Schematic view of the cold finger inside the vacuum chamber, between the magnetic field coils and 22 mm away from MOT position.

3.4 Cold Finger

In this section I will give more details on how we reduced the uncertainty of the BBR shift, namely the temperature uncertainty. As you see from Figure 3.2, in order to suppress the temperature uncertainty to the 1×10^{-18} level there are two options; either to measure the temperature seen by atoms very accurately within the 10 mK at room temperature or to cool down the environment around the atomic sample to cryogenic temperature. We designed a homogenous temperature environment (we call it 'cold finger') and it installed into vacuum chamber close to the MOT position. The cold finger allows us to determine the temperature seen by atoms at room temperature by factor of ten better compared to the MOT position. The cold finger can be also operated at liquid nitrogen temperature which allows us to suppress the BBR shift by a factor of about 100 and thus its uncertainty.

3.4.1 Design

The cold finger is designed to have well control temperature environment and to have the possibility to interrogate the atoms inside the cold finger while the cold finger at room temperature or cryogenic temperature. The cold finger is made from a copper (which has high thermal conductivity) to create a homogenous temperature distribution around the atomic sample and also the copper has zero emissivity (ideally), thus reducing the thermal exchange between the cold finger and the outside environment. Moreover, the atoms inside the cold finger should be isolated from seeing the BBR from the outside, thus the cold finger has only two orifices, which make the cold finger not suitable to be placed at the MOT position because it provides no access for beams for cooling and detection, etc., thus the cold finger is located 22 mm away from the MOT position. The atoms have to transport from the MOT position into the cold finger, details on the transporting atom see 3.4.3. The atoms are first cooled and trapped at the MOT position, then moved to inside the cold finger for interrogation and then moved back to the MOT position for detection. Figure 3.5 shows a simplified schematic view of the cold finger inside the vacuum chamber.

The cold finger has the shape of a hollow cylindrical tube with a length of 83 mm, an outer diameter of 32 mm, and an inner diameter of 12.9 mm. Inside the tube there is a graphite tube, to provide a black surface seen by atoms to reduce indirect effects due to BBR entering from outside, with a length of 50 mm, an outer diameter of 12.7 mm and an inner diameter of 9.5 mm. The tip of cold finger has an orifice 0.5 mm diameter. The second orifice is from the back, which is is blocked by a BK7 glass window to suppress the BBR and allows lattice and interrogation lasers to pass through, Figure 3.6 shows the parts of the cold finger. The 1-D lattice laser beam passes through the cold finger via the orifice and reflect back by retro-reflection mirror at the second end of the vacuum chamber. Figure 3.7 shown the cold finger after assemble.

Figure 3.6: This figure shows the cold finger parts before they are assembled. (1) is the core of cold finger, (2) is the graphite tube which is inserted inside cold finger as seen in (8). (3) the mounts holding a BK7 window between them at Brewster's angle, which are themselves clamped down by a threaded ring (4). (5) is an other copper tube connected to the cold finger via (9) to extend the cold finger to reach a view port of the vacuum chamber. (6) is a steel mount, which connects the entire cold finger to an external view port seen in (10). (11) shows the physical contact between the cold finger and an LN2 tank via a copper rod. The flexible tube (3) is used to suppress any stress or expansion on the contact point (11) during the cooling. (13) is the LN2 tank.

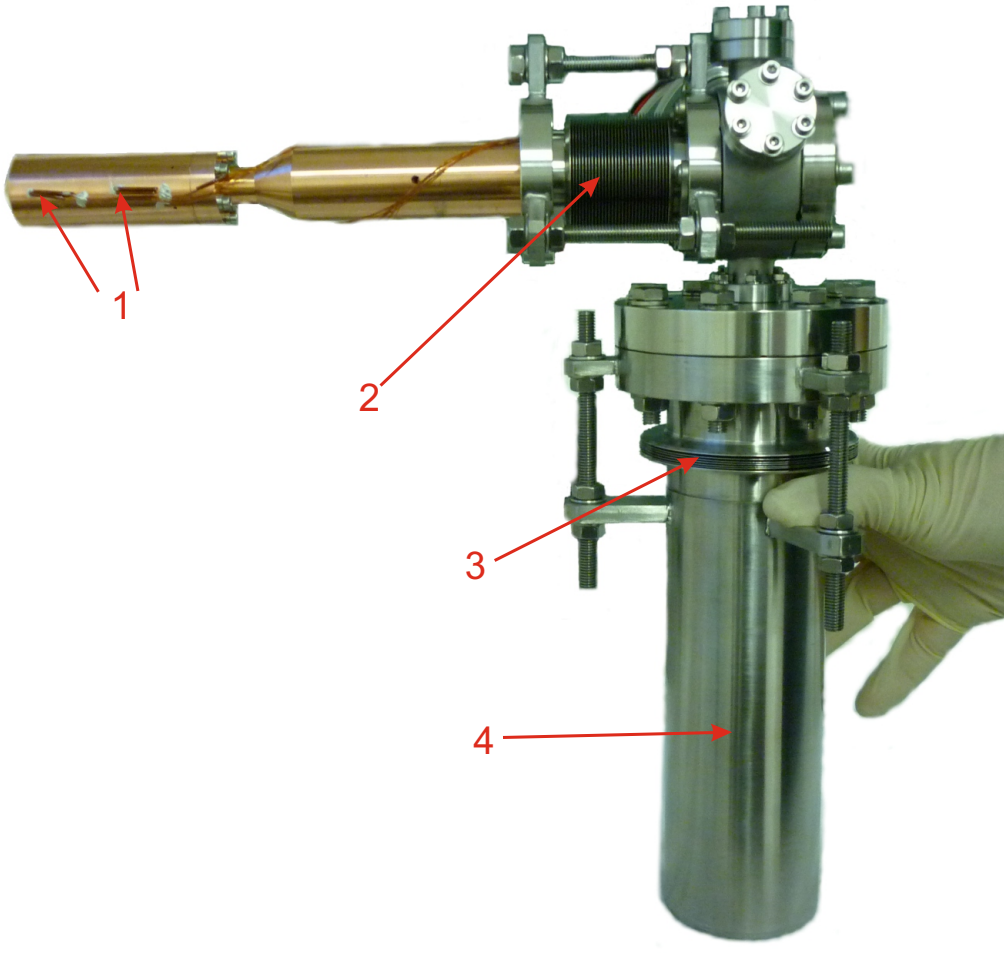

Figure 3.7: Cold finger after assembling all parts, (1) shows the Pt100 temperature sensors glued to the surface of cold finger. (2) shows the cold finger end is fixed to the viewport which has a flexible tube used for optimizing the orientation of cold finger. (3) is an additional flexible tube which is used to reduce any stress on the area where the cold finger is connected with the cold head of the LN2 tank. (4) is the LN2 tank, which has direct physical contact with the cold finger via a copper rod.

3.4.2 Residual BBR leakage

As I mentioned in the beginning of this section, the atoms inside the cold finger have to be isolated from outside world to avoid any BBR field may entering the cold finger. The cold finger has two orifices, one at the tip of the cold finger. The second at the back which is blocked by a BK7 glass window to suppress the transmission of the BBR from the outside. This means we have to take into account possible BBR which may entering from those orifices.

Tip of the cold finger

The atoms inside the cold finger experience an additional BBR shift due to BBR entering from the orifice. This shift has two contributions: the first one is due to BBR which seen by the atoms directly. This shift can be estimated as following

$$\Delta\nu_{BBR}^{(dir)} = \Omega \times \nu_{BBR}(T). \tag{3.16}$$

where Ω is the solid angle of the orifice as seen from the position of the atoms and can written as

$$\Omega \approx \frac{\pi r^2}{4\pi R^2} = \frac{r^2}{4R^2}. \tag{3.17}$$

Here r is the radius of the orifice and R is the distance between it and the position of the atoms inside the cold finger, typically $R = 15$ mm in our setup. The second contribution is due to reflection of BBR at room temperature which may enter from the orifice and hit the atoms after some reflection process on the inner wall of the cold finger. In order to estimate the shift, We assume for simplicity the cold finger to be a sphere with radius R [Mid11] and the orifice radius r. We assume that the BBR entering the cold finger via the orifice is isotropically from all directions, thus neglecting any effects of a finite size of the orifice. The inner wall has a spectral absorption coefficient $a(\nu)$. We consider also that the energy density inside the cold finger is spatially homogeneous and the total flux

entering into the cold finger is equal to the total flux out of the cold finger. The incoming flux at room temperature is written as [Mid11],

$$J^{RT}(\nu) = \frac{\pi r^2 c\rho(T_{RT},\nu)}{4}. \tag{3.18}$$

$\rho(T_{RT},\nu)$ is the spectral density of the BBR at room temperature, which can be written as

$$\rho(T_{RT},\nu) = \frac{8\pi h\nu^3}{c^3}\frac{1}{e^{h\nu/k_B T_{RT}}-1}. \tag{3.19}$$

The flux density of the BBR field emitted from the inner surface of the cold finger can be written as

$$J^{LN}(\nu) = \frac{\pi(4R^2-r^2)a(\nu)c\rho(T_{LN},\nu)}{4}. \tag{3.20}$$

Where, $a(\nu)$ is the absorption coefficient of the inner surface. The flux density which is absorbed by the inner surface of the cold finger is

$$J^{abs}(\nu) = -\frac{\pi(4R^2-r^2)a(\nu)c\rho^{coldfinger}(T,\nu)}{4}. \tag{3.21}$$

Finally, the flux density that leaks out of the cold finger can be written as

$$J^{leak}(\nu) = -\frac{\pi r^2 c\rho^{coldfinger}(\nu)}{4}. \tag{3.22}$$

where c is the speed of light. The spectral density inside the cold finger can be estimated by assuming the total density flux that enters into the cold finger is same as the total density flux that leaves the cold finger, the system is in equilibrium situation, when the sum of Eqs.(3.18),(3.20),(3.21),(3.22) is equal to zero. Thus we can write the spectral density $\rho^{coldfinger}$ inside the cold finger as

$$\rho^{coldfinger}(\nu) = \frac{(4R^2-r^2)a(\nu)\rho(T_{LN},\nu)+r^2\rho(T_{RT},\nu)}{(4R^2-r^2)a(\nu)+r^2}. \tag{3.23}$$

By using the Eq. 3.23 and integrating over the BBR spectrum inside the cold finger, the indirect BBR shift is calculated. Figure 3.9 shows the direct and indirect BBR shifts inside the cold finger. As you see, both are proportional to the orifice radius and for 0.25

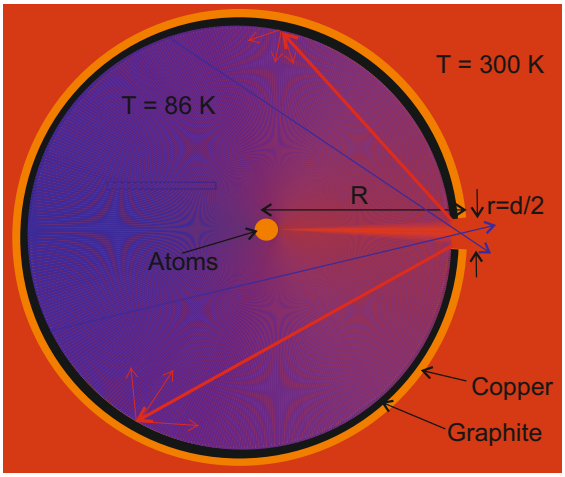

Figure 3.8: Sketch of the model used to estimate the effect of BBR leaking in from outside. We model the cold finger as a sphere and the atom at position 15 mm away from the orifice. The inner surface of the sphere is made of graphite which has a high absorption coefficient of 90%.

mm radius the total shift is very small, below 5×10^{-19} fractional shift. The shift is taken as an upper limit for the uncertainty, when the clock operate inside the cold finger.

Back of the cold finger

As I mentioned at the beginning in this section, the cold finger has a second opening port in the back to allow the lattice laser to pass through the cold finger and be reflected back as well as to send the interrogation laser beam to the atoms. The BBR entering through this orifice, has to take into account. This orifice is much large 10 mm diameter compared to that in the tip of the cold finger. The BBR shift arising due to this orifice according to Eq.(3.16) is on the level of 10^{-16}, which is a lot and has to be suppressed. We used BK7 glass in the back of the cold finger (see Figure 3.5) to suppress the transmission of the BBR and without disturbing lattice and interrogation lasers. The transmission of light through the BK7 window can be written as [Str77],

$$T = \frac{(1-R)^2 e^{-\alpha d}}{1 - R^2 e^{-2\alpha d}}, \tag{3.24}$$

where R is the reflection from the surface of the BK7 window, α is the absorption coefficient and d is the thickness of the BK7 window. Assuming that there is negligible

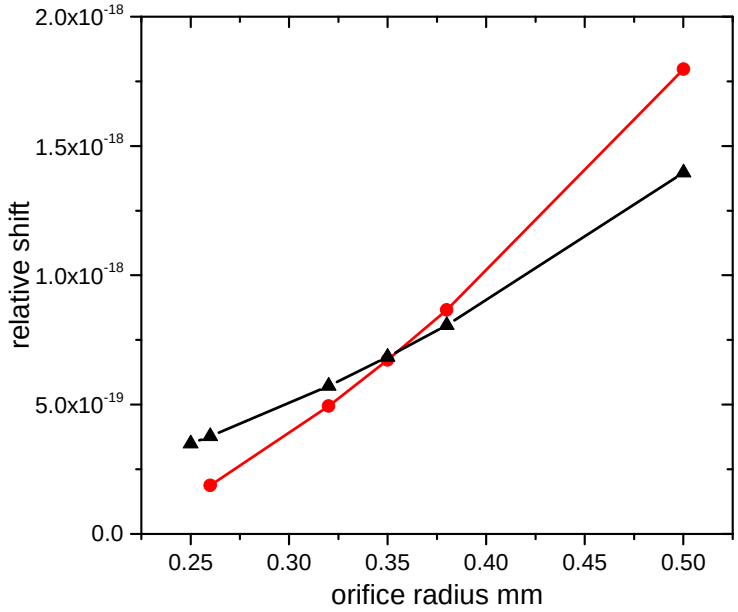

Figure 3.9: Residual BBR shift inside the cold finger due to BBR at room temperature entering through the orifice of the cold finger as a function of the orifice radius. Black triangles represent the direct BBR shift assuming atoms 15 mm inside the cold finger. Red circles represent the indirect BBR shift based on the model presented in the main text.

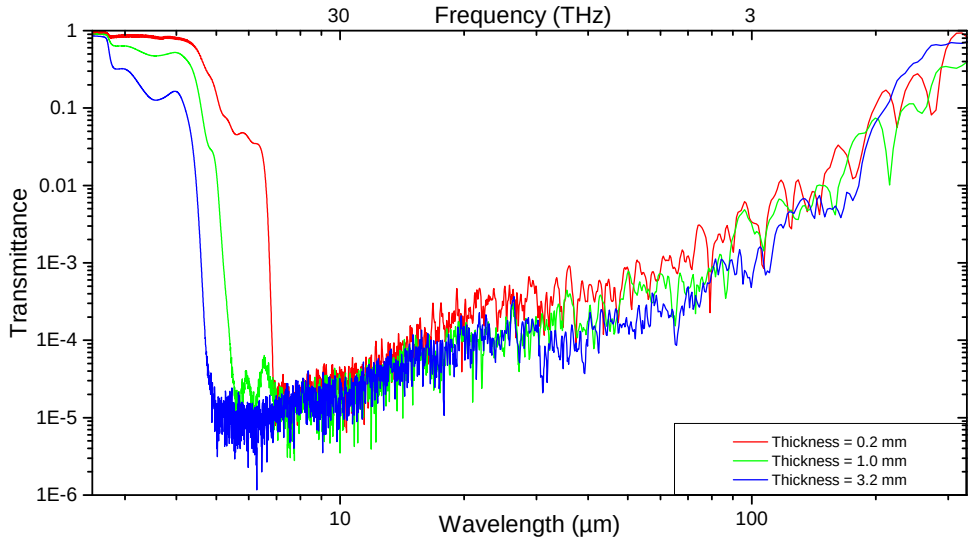

Figure 3.10: Transmittance of BK7 glass as a function of wavelength for different BK7 thicknesses. Red line for BK7 thickness 0.2 mm. Green line for BK7 thickness 2 mm and Blue line for BK7 thickness 3.2 mm. The transmittance is well below 10 % over all the BBR frequency range but above 80 THz the transmittance of BK7 starts to increase clearly for a thickness 3.2 mm.

reflection from the surface of the BB7 window ($R = 0$) to obtain upper limit, we can re-write Eq.(3.24) as

$$T = e^{-\alpha d}. \tag{3.25}$$

The absorption coefficient α of BK7 to the power spectrum of BBR, is important to determine, which thickness d we need to suppress the BBR shift to below 10^{-18}. We have used different sources to determine the absorption coefficient of BK7 in different frequency range, as following;

- Frequency range ($f \leq 1.3$ THz): The absorption coefficient used from the results reported by [Naf07].
- Frequency range (1.3 THz $\leq$ f $\leq$119 THz), PTB-Berlin (AG 7.32) has kindly measured the transmittance of BK7 for different thickness, as seen in figure 3.10.
- High frequencies $\geq$ 119 THz are covered by SCHOTT company (*www.schott.com*). The Schott datasheet specifies the transmittance of BK7, and the absorption coefficients have been derived.

By combining all absorption coefficients to cover the entire spectral range relevant for the room-temperature BBR, the transmittance of BK7 has been calculated for different thicknesses. To calculate how much BBR leaks through the BK7 window at the back of the cold finger, we again modeled the cold finger as a sphere with 20 mm radius (as an upper limit, the atom position inside cold finger is 30 to 35 mm away from back orifice). The BBR shift has been calculated for different BK7 window thickness as you see in figure 3.11. The BBR shift is suppressed to level of about 1×10^{-19} by using BK7 window thickness 3 mm. Thus the suppression will better if one increase the thickness of the BK7 window (see in Figure 3.11 for 10 mm). We decided to use 3 mm BK7 window. We also calculate the dynamic BBR shift at 115 THz, which is found to be very small, well below the 1×10^{-20} level, so it is negligible.

3.4.3 Characterization

In this subsection, I will give more details on the characterization of the cold finger, including temperature gradients of the cold finger, how to move atoms form the MOT

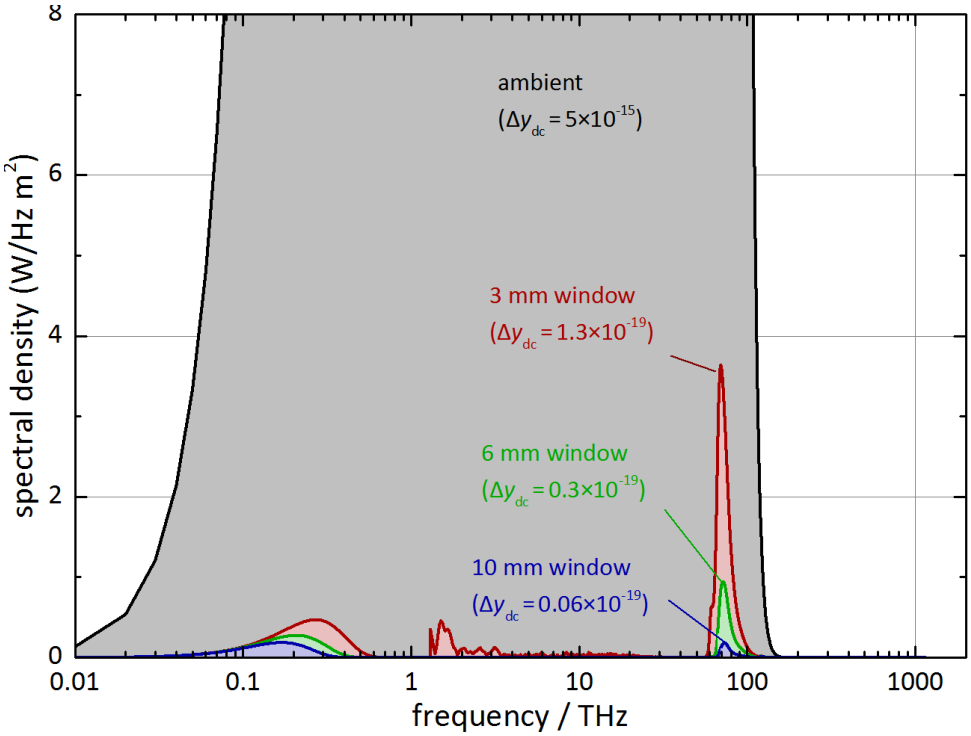

Figure 3.11: Spectral density of BBR as a function of frequency for different BK7 thicknesses. The black line normal spectrum of the BBR (full transmission). The red (green, blue) lines depicts the spectral density of the BBR at room-temperature transmitted through a BK7 window with a thickness of 3 mm (6 mm, 10 mm).

position to the cold finger position, the temperature of the atoms inside the cold finger, and sideband measurements.

Installing the cold finger

After assembling the cold finger shown in Figure 3.7, it was installed first in a test chamber. It was baked at 160 °C, limited by the maximum allowed temperature of some viewports and pumped down to 3×10^{-10} mbar. The baking lasted for more than one week. We tested the Pt100 temperature sensors on the cold finger by cooling it down to liquid nitrogen temperature to see how Pt100 sensors response. Figure 3.12 shows the temperature readings of the two Pt100 sensors on the cold finger, as it is cooled down to 86 K within only one hour with a time constant of about 30 minutes (determined from an exponential fit of an exponent decay). It stays at low temperature for 3–4 hours with one filling of the liquid nitrogen in the LN2 tank. When we let the cold finger warm up, it heated up very slowly within 24 hours with a time constant of 7 hours. In this test, the cold finger showed premising results.

The test chamber with the cold finger was moved close to our main chamber. To install the cold finger in the main chamber, the main chamber was vented with Argon and the cold finger installed in the main chamber (we replaced the cold finger in the position of the capacitor which had been used in previous work [Mid12a]). We baked the main chamber to 60 °C and it was pumped for several weeks. After that, the main chamber pressure had returned to normal condition. Figure 3.13 shows the cold finger inside the main chamber as well as the blue MOT of the ^{87}Sr atoms which is 22 mm away from its tip.

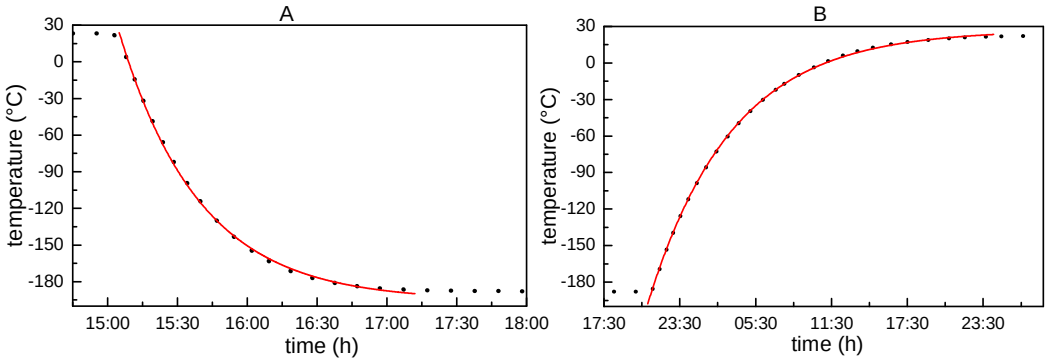

Figure 3.12: Temperature of cold finger over time, from 296 K to liquid nitrogen temperature (A) and returning back from liquid nitrogen temperature to 296 K, which takes about one day to return to room temperature (B). The dot points is the reading of Pt100 sensors and the red line is a fit of the function $y(t) = y_0 + Ae^{\frac{t-t_0}{t_c}}$, where the time constant t_c of 30 min for the case A and 7 hours for the case B.

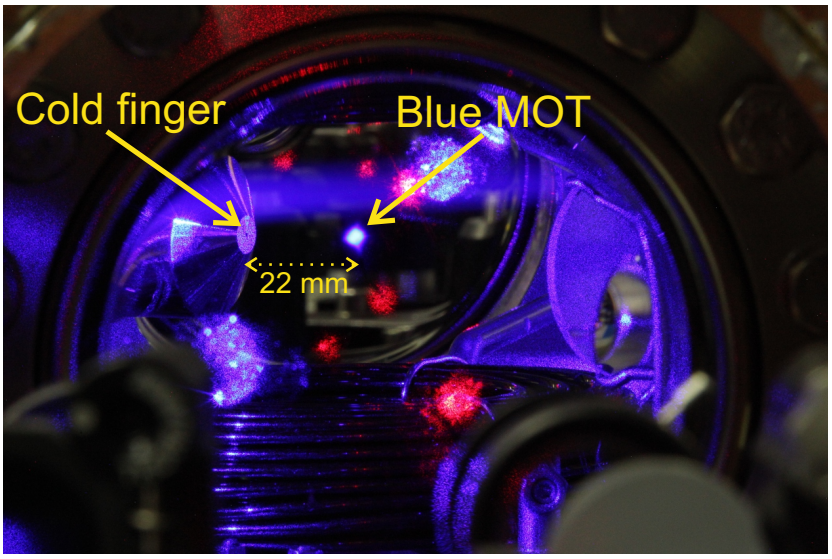

Figure 3.13: A photograph of the cold finger installed in the main chamber together with a blue MOT of the ^{87}Sr atoms.

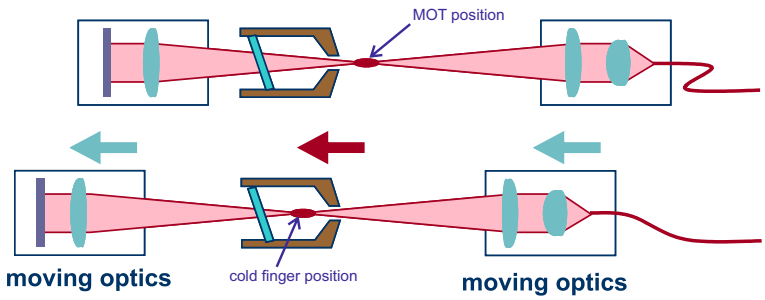

Figure 3.14: Schematic of the translation of the optical lattice setup. The translation stages on both sides move simultaneously to move the atomic sample from the MOT position to the cold finger for spectroscopy and then it move back to the MOT position for detection.

Translation stages

The cold finger tip is 22 mm away from the MOT position, and the atomic sample has to be moved from there into the cold finger for spectroscopy. We use the same setup developed by Thomas Middelmann [Mid12b] to move the atomic sample into the cold finger, I will summarize it here very briefly. In order to move the atomic sample into the cold finger, all optics of the lattice trap have to move from the MOT position into the cold finger position simultaneously with air-bearing translation stages. The lattice optics are mounted on two air-bearing translation stages, as in Figure 3.14, thus the atomic sample can be move over long distance up to 10 cm within 200 to 400 ms with only minimal changes of their alignment. The motion profile of the translation stages is selected as a sinusoidal acceleration for efficiently transporting as,

$$a(t) = \pm a_{max} sin \left[\frac{\pi(t - t_0)}{t_{ramp}} \right]^2 , \tag{3.26}$$

where a_{max} is the maximum acceleration of the translation stages usually 10 m/s^2, t_{ramp} is the duration of the acceleration. The trajectory is selected to be as in figure 3.15 with a transport distance about 45 mm within 350 ms. The translation stages have been optimized together with the cold finger's alignment to have the lattice laser pass through the orifice of the cold finger to have maximum power pass through the cold finger and be reflected back. During the motion the change in reflection power is less than 10%.

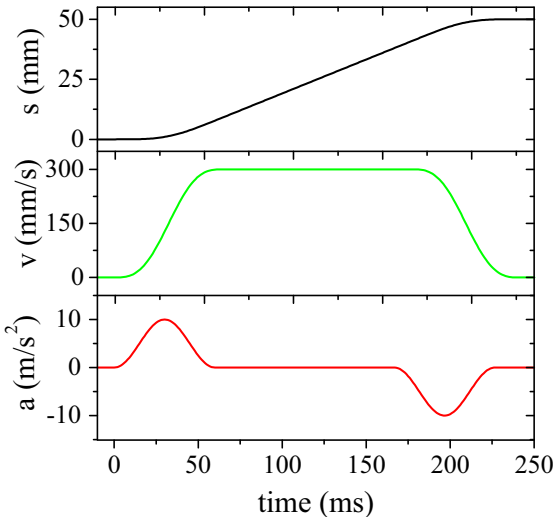

Figure 3.15: Typical trajectory of the translation stages. The translation stages move by a distance of 50 mm distance within 250 ms at a peak velocity of 300 m/s^2. The stages started and stopped using the same profile for acceleration and deceleration adapted from [Mid12b].

Trap lifetime

After optimizing the reflection power of the lattice laser during the motion, the ^{87}Sr atoms have been transported by 45 mm from MOT position to the cold finger position within 350 ms. The atom loss during the transporting is about 10 %.

The lifetime of the atoms has been measured in the cold finger. To determine the lifetime in the trap, we have measured the remaining population after storing the atoms in the cold finger for different durations. Figure 3.16 shows the decay of the atoms from the trap in the cold finger. The lifetime has been determined under two conditions; once when the cold finger was at room temperature, and the second time at cryogenic temperature. Both measurements show almost the same lifetime, 1.7 s and 2.1 s, respectively.

Compensation magnetic field

At the position of the atoms inside the cold finger the residual magnetic field can be completely different from that at the MOT position. The residual magnetic field needs to be compensated along all three axes, to reducing the splitting between the $m_F = \pm 9/2$ components, thus minimizing the second-order Zeeman shift. The coils which are used

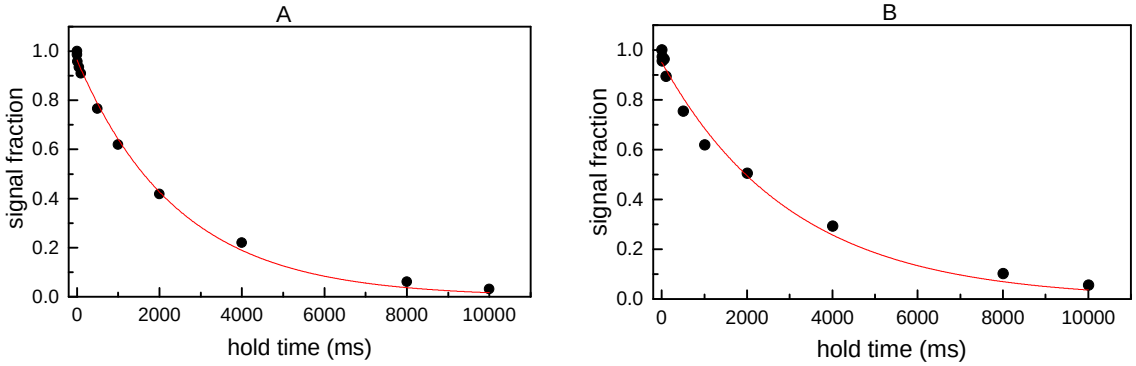

Figure 3.16: Fraction of the initial atom number remaining in the trap as a function of holding time. A) the cold finger was at room temperature 294 K, the life time was 1.7 s. B) The cold finger was at 86 K, the life time was 2.1 s.

to compensate residual magnetic fields in the MOT position have been used for the cold finger as well. As we found a large change of the residual magnetic field along the x-axis. Figure 3.17 shows the splitting of the clock transition ($m_F = +9/2$) component as a function of the current applied to the coils in x and y directions.

Sideband and atom temperature

Further characterization of the lattice trap inside the cold finger, including the lattice depth and the atomic temperature, requires measuring the sideband spectra [Win79] in the lattices. The axial sidebands are recorded after transporting the atoms from the MOT position to the cold finger position, and also without transport at MOT position for comparison. From these measurements we found that the potential depth at the cold finger position is similar to that at the MOT position Figure (3.18). We can infer the potential depth from the axial trapping frequency. The temperature of the atomic sample has also been determined from the sideband spectra (red and blue sideband) and the analysis is done according to the model developed in [Bla09]. At the cold finger position, the temperature of the atoms has been 0.8 μK axial temperature and 1.6 μK radial temperature, which is close to the temperature at the MOT position (0.3 μK and 1.6 μK axial and radial temperature respectively). The temperature in the axial direction is a bit higher due to some shaking of the stage.

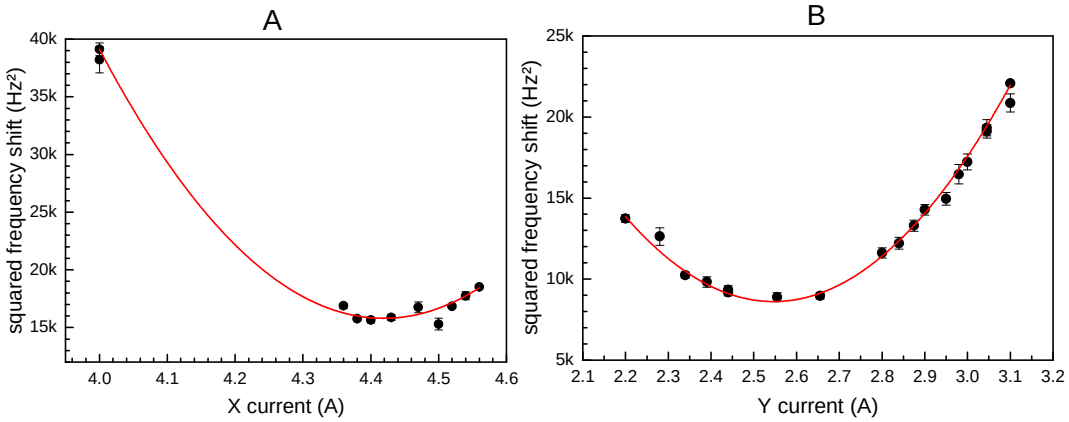

Figure 3.17: Splitting squared of the clock transition with $m_F = +9/2$ component from plotted as a function of the current applied to the compensation coils along the x, and y axes. The data is well described by a parabola fit. A) Applied current was on the X-axis coils, which was the largest residual magnetic field, the best value of the current was 4.45 A. B) Applied current was on the Y-xis coils, best current value was 2.55 A. During the measurements, the bias magnetic field (few tens of μT) is applied for quantization axis. The splitting between the $m_F = \pm 9/2$ components is found to be 180 Hz.

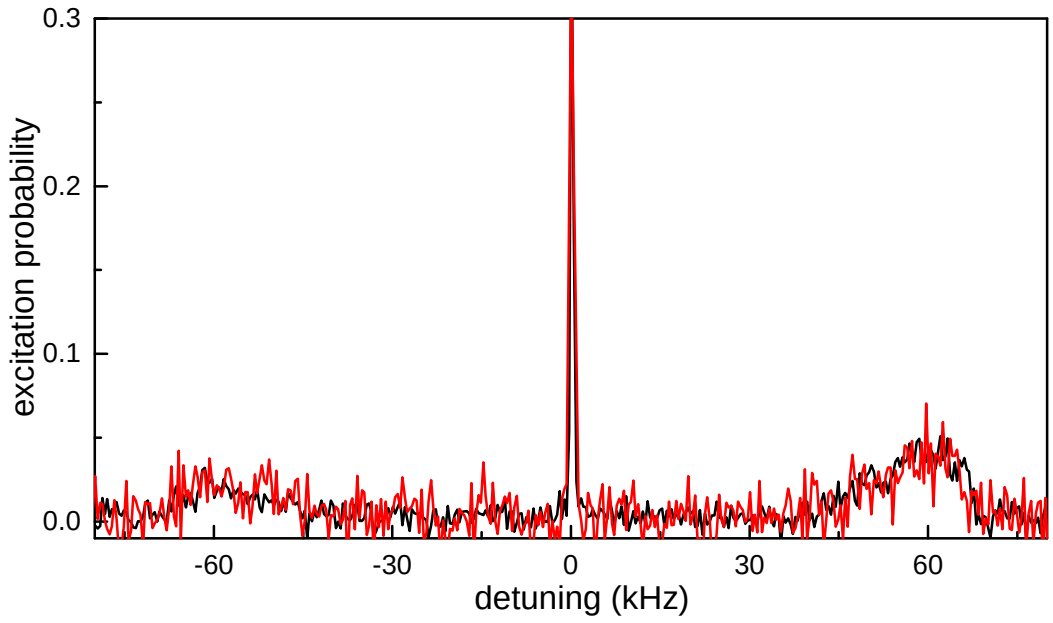

Figure 3.18: Axial sideband spectrum and the carrier. Black solid line: at the MOT position with no transporting. Red solid line: at the cold finger position. The axial frequency of the trap $\approx$ 75 kHz is the same at the MOT and cold finger positions.

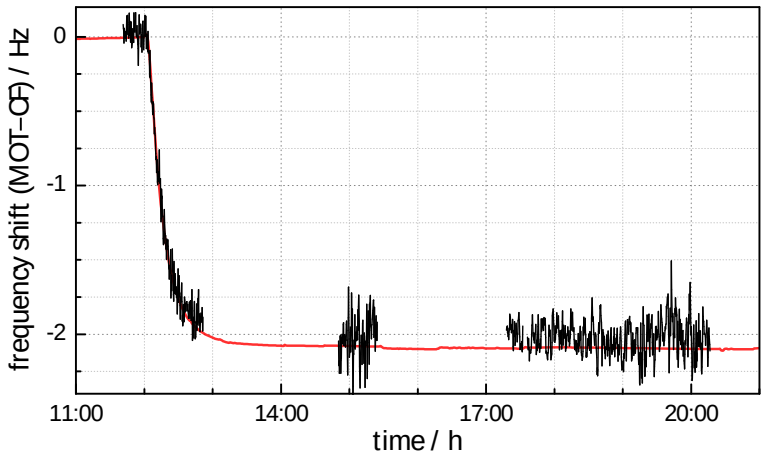

Figure 3.19: Frequency difference between clock operation at MOT and cold finger positions over time. The measurement start with both positions at room temperature and then the cold finger start to cool down. As you see the frequency shift due to BBR shift starts to be clear once the cold finger cools down. The red line is the expectation value for the difference of BBR shift between MOT and cold finger position according to Eq. 3.8.

3.4.4 BBR shift measurements

During this subsection, I will present the BBR shift measurements in the cold finger position. The ^{87}Sr lattice clock was operating at the cold finger position while the cold finger was at room temperature and cryogenic temperature to measure how the shift of the clock transition is temperature dependence, according to BBR shift equation (3.8). In order to measure this shift a stable reference clock is required. The MOT position was used as a reference by doing a self-comparison (Sr1 vs Sr1) by operating two interleaved stabilizations, one at the cold finger position and the second at the reference position (the MOT position). The second option is to use the transportable ^{87}Sr lattice clock (Sr2) of our group as a reference. We have used both references for better understanding the ^{87}Sr lattice clock at the cold finger, as it will be clear during this subsection.

The MOT position as a reference

The MOT position has been used as a reference to measure the BBR shift of the $^1S_0 - {}^3P_0$ transition of ^{87}Sr atoms by interrogating them in interleaved stabilizations: The first

stabilization cycle probes the atoms at the MOT position and the second stabilization cycle at the cold finger position. The correction from atomic reference to the clock laser is recorded for both stabilizations and the difference in frequency between them is due to the BBR shift. We started the measurement when the cold finger was at room temperature and after that the cold finger start to cool down while the measurements was running to monitor online the shift during the cooling of the cold finger. Figure 3.19 shows the result and the expectation value of the difference of BBR shifts between MOT and cold finger positions represented by the red solid line, which is calculated according to Eq.(3.8), as you see once the cold finger start to cool the difference shift between MOT and cold finger positions is increased and it follows the expected dependence. We have noticed that there is small frequency offset between the MOT and cold finger positions as you may see it in the Figure 3.19, where the expectation does not mach perfectly the result. The fractional frequency offset is 9×10^{-17}. There are several reasons that can cause this frequency offset as,

- Residual DC Stark shift, magic wavelength of the lattice laser, second-order Zeeman shift.

- Residual motion of the atoms in the lattice: It can be arise due to the shaking of the translation stage during and after the transport from the MOT to the cold finger positions and can cause a Doppler shift.

- The effective temperature seen by the atoms at the MOT position may change when the cold finger is cooled down (the cold finger is only 22 mm away from the MOT position and has a finite emissivity).

The residual DC Stark shift has been checked by operating the clock inside the cold finger at different positions and we did not observed a significant frequency shift. The magic wavelength of the lattice laser was 2 MHz different between the MOT and cold finger positions during the BBR measurement, which caused a fractional shift less than 1×10^{-17}. The second-order Zeeman shift is different between the MOT and cold finger positions by 1.2×10^{-17} because they have different magnetic field. Now I will give more details on the other points which are listed above.

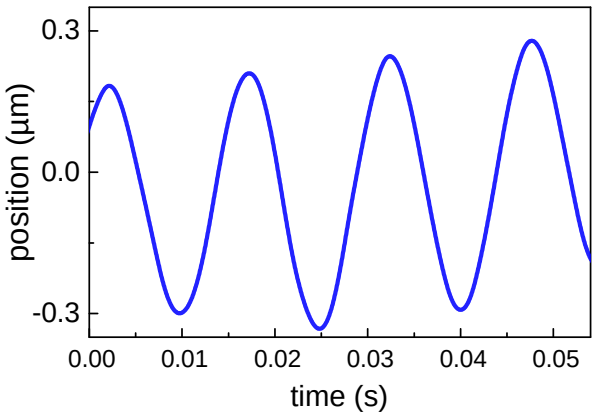

Figure 3.20: The shaking of the translation stage after arrival at the final position. The shaking is detected by the motion control of the translation stages. The shaking amplitude is less than 300 nm.

Residual Motion

We have noticed that, when we move the atomic sample from the MOT to the cold finger positions, the air bearing translation stages were shaking after reach the final position, as seen in (Figure 3.20). The shaking oscillates at a frequency of 57 Hz (about 17 ms period) with a damping constant of several hundreds milliseconds. If this shaking is purelly in axial direction of the lattice, we expected that it produces no frequency shift (Doppler shift) since we used fiber length stabilization during the interrogation time to stabilize optical length from the interrogation laser to the atom position. We have checked the inloop error signal of the fiber length stabilization (Figure 3.21) with motion (at the cold finger) and without motion (at the MOT position). Both signals show similar characteristics, the phase is stabilized within 0.1 ms and there is no oscillation with 17 ms periods is observed. From this we would not expect a Doppler shift along the interrogation laser. But, the atoms could move nearly vertical or with angle with respect to the interrogation beam due to the shaking. This scenario is possible since the lattice optics are mounted on the translation stages (the income lattice beam is mounted on the first stage and the retro-reflection mirror is mounted on the second stage). Once the stages are shaking, this will moves the focus of the lattice beam up and down, thus the atomic sample with it. We have recorded the retro-reflection power of the lattice beam without intensity stabilization (the power which reflects from the retro-reflection mirror into fiber). We have seen a clear

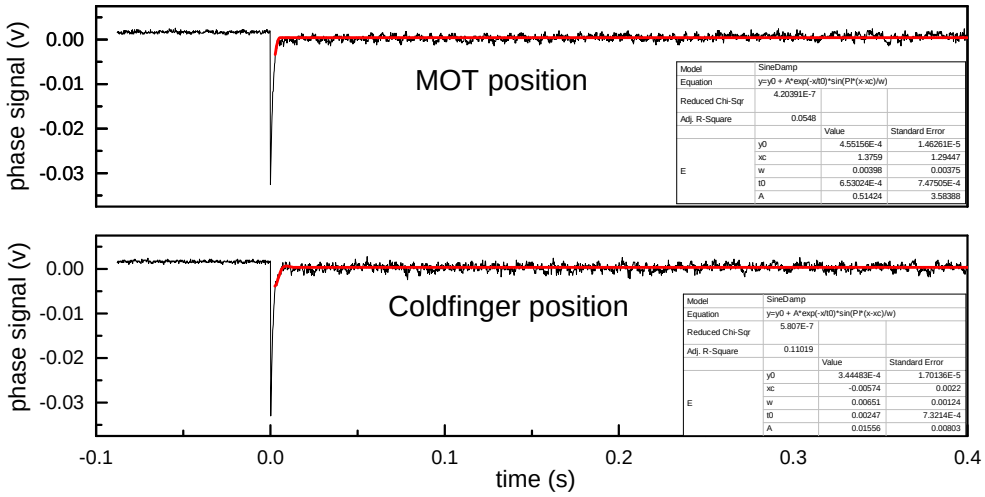

Figure 3.21: Behavior of the fiber length stabilization when the interrogation light is on at 0 ms. The signal is a dc signal, which is generated by mixing down the inloop beat. Upper: at the MOT position without motion. Bottom: at the cold finger position with motion.

power oscillation when we move the stage to the cold finger position. This oscillation with a period of about 14 ms as shown in (Figure 3.22). This motion is not compensated by the fiber length stabilization, thus has to be taken into account.

We have measured how much residual shift of the clock transition due to a residual motion by probing the clock transition at different points on the oscillation profile of the residual motion. In order to do so we have used interleaved stabilizations, both cycles are at cold finger position and both cycles have same cycle time but we shift one with respect to other. The measurement is repeated for different delay time between the cycles to detect the oscillation profile. We have seen clear a sine wave behavior of the residual shift of the clock transition. This means that the residual shift will average out if the clock pulse duration is chosen in such a way as to cover an integer number of periods of the oscillation and the residual shift will be maximum if the clock pulse duration is stopped at a half-integer multiple of periods of the oscillation. The measurements is repeated with different clock pulse duration to see how much the amplitude of the oscillation is vary

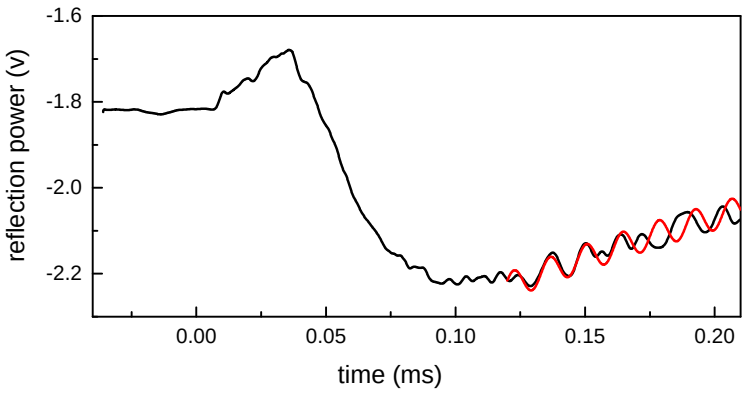

Figure 3.22: Retro-reflection power of the lattice laser while the translation stages move from the MOT to the cold finger positions. The red solid line is a sin wave fit with a period of 14 ms.

with the clock pulse duration as shown in (Figure 3.23), where the fit function is used as

$$y(t) = y_0 + \underbrace{a_0 \left| \left(\frac{\sin(\frac{\pi t_{pulse}}{w})}{t_{pulse}} \right) \right|}_{\text{amplitude}} \sin\left(\frac{2\pi(t - t_0)}{w} \right), \tag{3.27}$$

where t is the delay time between cycles, y_0 is an offset frequency, a_0 is the prefactor of the amplitude A, where A is clock pulse duration t_{pulse} dependence. w is the oscillation period, t_0 is a phase offset. Five measurements have been done with different clock pulse durations as seen in Figure 3.23 together with the fit function (Eq .3.27). From the fit function, we have determined the oscillation period w of 17.5 ms (0.0268) and prefactor $a_0 = 2.64 \times 10^{-14} \pm 4.53 \times 10^{-15}$. After determining the w, and a_0, the amplitude of the Doppler shift can be calculated as a function of the clock pulse duration as seen in (Figure 3.24). The maximum Doppler shift due to shaking of the stages is 24 mHz (or 5.5×10^{-17} fraction shift) with statistical uncertainty of 8×10^{-18}. This shift has to takes into account to explain partially the offset frequency, which has been seen in (Figure 3.19). In next subsection, I will give details on other effects may explain the rest of the shift, e.g., if the atoms in the MOT position seen different effective temperature when the cold finger is cooled.

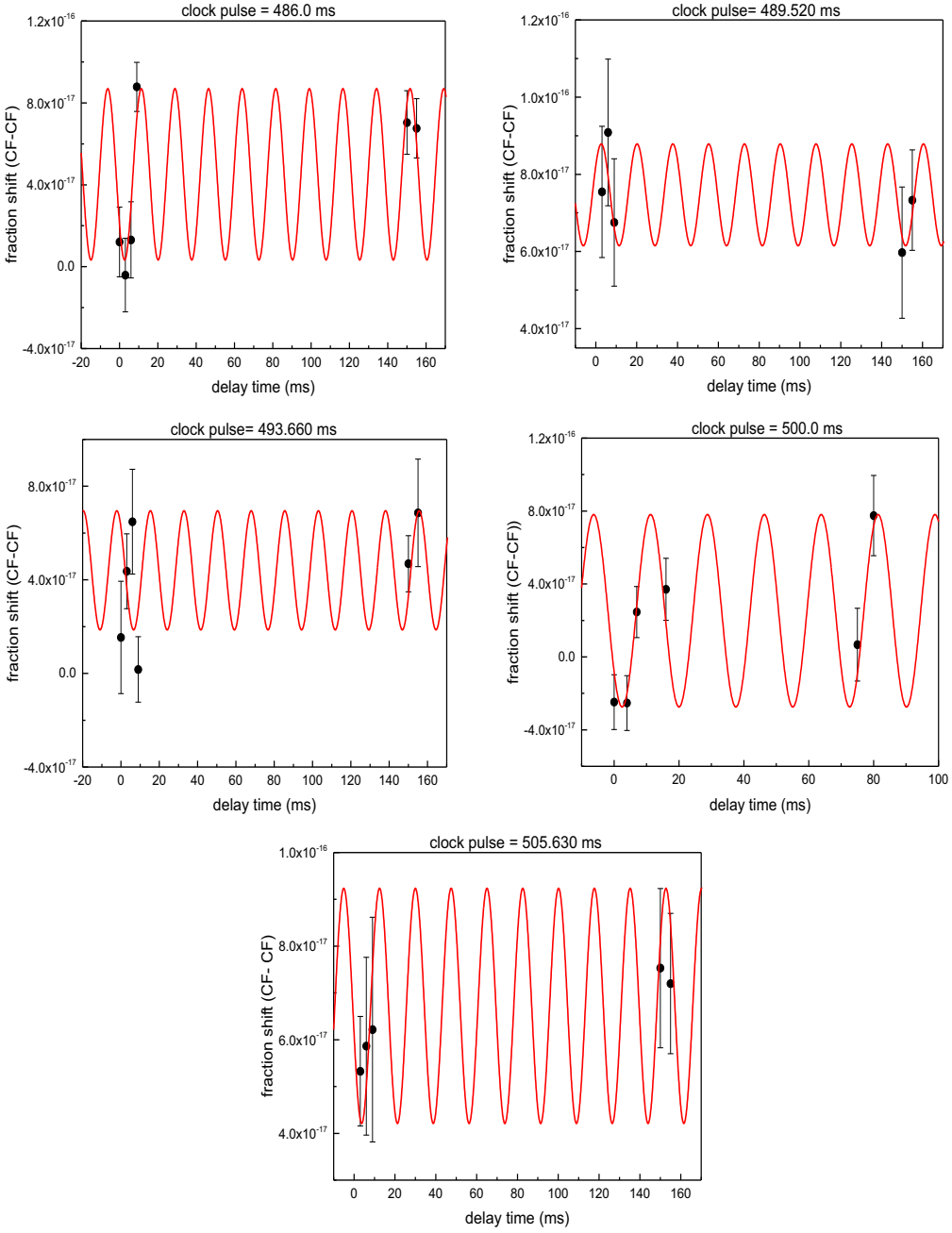

Figure 3.23: Fractional frequency shift between interleaved stabilizations as a function of the delay time for different lengths of the clock pulse (both stabilizations are probing the clock transition at the cold finger position). The red solid lines are the fit function (Eq. 3.27).

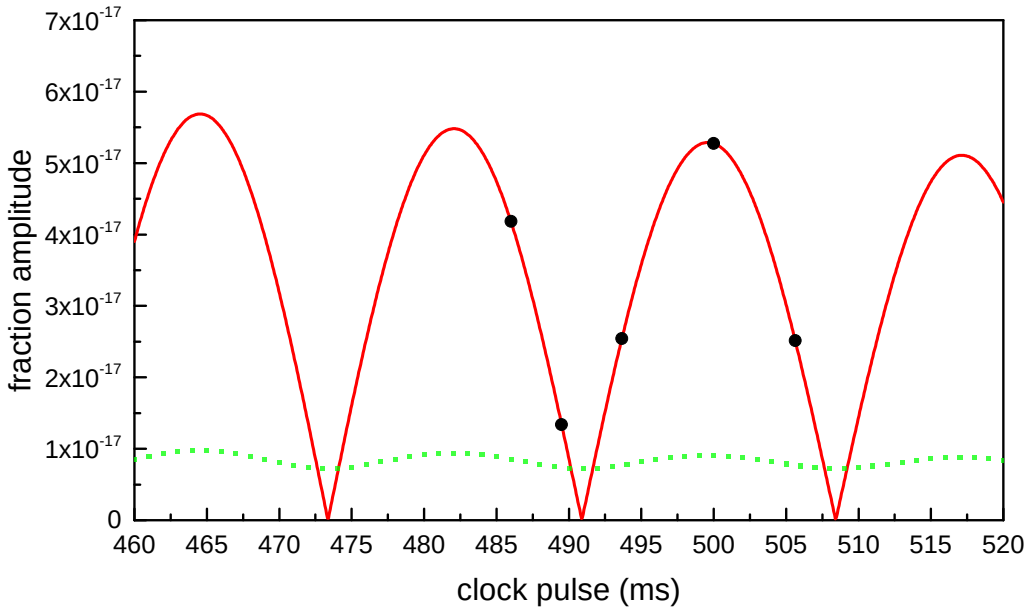

Figure 3.24: Amplitude of the residual shift as a function of the clock pulse duration. The amplitude is determined by using the function of $a_0 \left|\sin\frac{\pi t_{pulse}}{w}\right|$, where $a_0 = 2.64 \times 10^{-14}$, w is the period of the oscillation which is 17.5 ms. The black points are indicated, where we performed the measurements. The green dashed line is the uncertainty of the measurements, which is calculated by using error propagation, the uncertainty of the Doppler shift is 8×10^{-18}, which is limited by the uncertainty of the w and a_0.

Emissivity of the cold finger

The temperature sensors on the cold finger have been shown that the coldest temperature can be reached is about 86 K instead of 77 K, when the cold finger is cooled with Liquid nitrogen. The temperature difference could be due to the emissivity of the cold finger is high, or the cold finger has a thermal contact to the environment, or both. The surface of cold finger (made of copper) has been polished and cleaned to achieve very low emissivity, but while assembling the cold finger, it was on air for about one hour, which may have caused an oxide to form on the surface of the cold finger, thus increasing its emissivity, if the emissivity is still low or not, this will be clear when I discuss the thermal contact (next) and the measurement we did at the MOT position while the cold finger at cryogenic temperature and room temperature, to check if atoms at the MOT position may experience a different effective temperature when the coldfinger is cooled (in the next subsection).

The heat flux (Q) from the environment to the coldfinger has to be taken into account, especially from the back of the coldfinger, where the coldfinger has thermal contact with the main chamber at room temperature. In order to estimate the heat flux to the cold finger, the thermal resistance R of its contact to the environment has to estimate, we apply thermodynamic law (conservation of energy),

$$Q = \frac{(T - T_0)}{R} = -\kappa \frac{dT}{dt}, \tag{3.28}$$

where T is the temperature of cold finger, T_0 temperature of the chamber, and $\kappa = C \cdot m$, where C the heat capacity of the cold finger which is about 385 J/kg $\cdot$ K and m is the cold finger's mass, which is 1.76 kg. The solution of Eq.(3.28) is

$$T(t) = T_0 + Ae^{t/t_c}, \tag{3.29}$$

where $t_c = R \cdot C \cdot m$, which is the time constant. The coldfinger has been shown a behavior as Eq.(3.29) when the cold finger heated up from cryogenic temperature to room temperature, as seen in Figure 3.12, which indicated that the emissivity of the cold finger is still very low, since we did not observed T^4 dependence (radiative heating) during the heating.

The time constant t_c has been measured to be about 7 hours, and then R has been calculated to be about 36 K/W, thus the heating flux is about 5.8 W. The dewar (LN2 tank) is connected to the cold finger via an additional copper rod as seen in Figure (3.6, number (11)). This copper rod is 55 mm long and 10 mm in diameter; and together with the thermal conductivity of the copper (about 400 W/m.K) and the heating flux of the cold finger (5.8 W), a temperature difference of about 8 - 9 K between the cold finger and LN2 reservoir is expected, resulting that the cold finger's emissivity is still very low and in order to clarify that, next subsection I will show the experimental result of how much atoms at the MOT position see a different in the effective temperature while the cold finger at cryogenic or room temperature.

The transportable clock Sr2 as a reference

Our transportable ^{87}Sr lattice clock Sr2 was available to use as a reference clock at the end of 2015. The transportable clock is completely independent from Sr1. The Sr2 is operated at room temperature and used as a reference to check if atoms in the MOT position see different effective temperature when we cool down the cold finger. The effective temperature may change when the cold finger (only 22 mm away from MOT position) at the cryogenic temperature.

In order to check that, we have performed set of comparisons between Sr1 and Sr2, the Sr1 is operated at the MOT position for both measurements but once when the cold finger was at room temperature and the second at cryogenic temperature. The beat signal between the interrogation lasers of the Sr1 and Sr2 (at 30 MHz introduced by a marker AOM) is recorded during the comparisons and figure 3.25 shows the the frequency difference between both clocks after systematic frequency shifts for both clocks have been corrected. The atoms in the MOT position do not see significant different effective temperature when the cold finger is cooled as seen in figure 3.25, thus resulting that the emissivity of the cold finger has to be low.

The second task of the comparison between Sr1 and Sr2 is to measure the BBR shift. In order to measure the BBR shift, two sets of comparisons are required and Sr1 has to operate at the cold finger position. The first comparison, when the cold finger is at room temperature and the difference between (Sr1 (300 K)-Sr2 (300 K)) is measured and correct systematically (without correction from BBR shift). The second comparison, when the

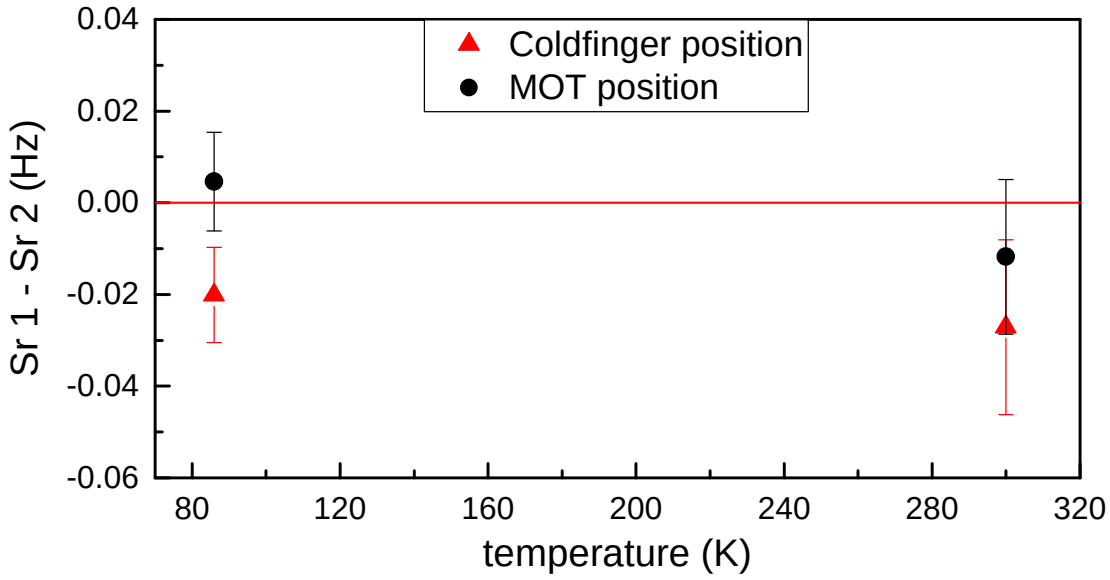

Figure 3.25: The comparison Sr1 against Sr2 at different cold finger temperature. The systematic corrections for both systems are corrected. The black points: The measurements are done at the MOT position while the cold finger at 86 K and 300 K, from these measurements there is no significant shift due to the changing of the effective temperature has been observed, which indicated that the emissivity of the cold finger is low. The red points: The measurements are done at the cold finger, while the cold finger at 86 K and 300 K, all systematic shift has been corrected including the BBR shift. The offset frequency between red and black points is due to the Doppler shift (see Figure 3.24) when the atoms are transported from the MOT to cold finger positions.

cold finger is at cryogenic temperature 86 K, thus the difference between (Sr1 (86 K)-Sr2 (300 K)) is measured also and correct systematically (without correction from BBR shift). The difference between these comparisons is compared with the expectation value of the BBR shift, which is calculated according to Eq.(3.8). Figure 3.26 shows the result of the comparisons. Both comparisons show white frequency noise and average down with square root of the averaging time to a level of 1×10^{-17}. In Figure 3.26 (C) is shown the BBR shift in our system Sr1 (blue point), which is -2115.1 mHz $\pm$ 11 mHz (systematic) $\pm$ 18 mHz (statistical) which agrees very well with the expectation value (blue solid line). The BBR shift in ^{87}Sr atoms for clock transition is measured in our group and Katori group in Japan [Ush15]. In Katori group, BBR shift measurements is not limited by statistical uncertainly, because they used share clock laser for both system Sr1 and Sr2, thus reject the Dick effect. Their instability is one order of magnitude better from our instability in the BBR shift measurements. Our BBR shift measurement together with Katori group measurement are shown in Figure (3.26 (C)), the offset frequency shift between them is because they have different temperatures by 1.3 K at room temperate and by 9 K at cryogenic temperature.

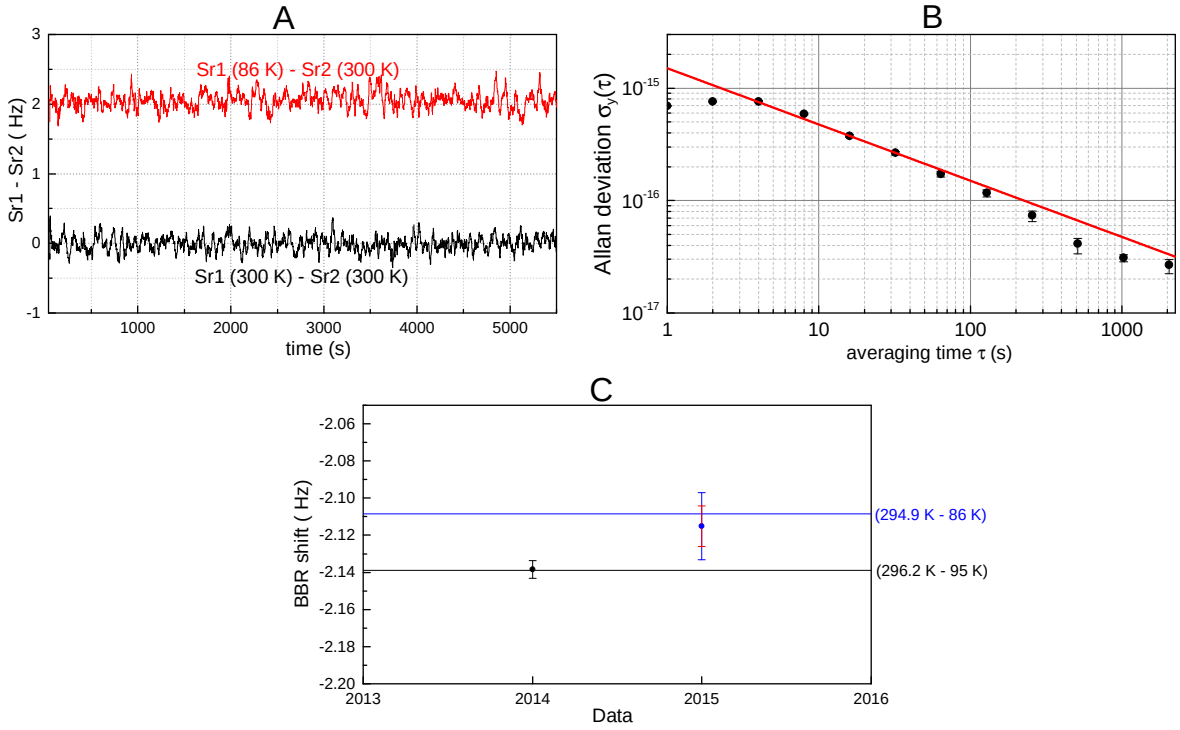

Figure 3.26: Results of the Sr1 against Sr2 comparison. A) Beat signal between the interrogating lasers of the Sr1 and Sr2 at different temperatures of the Sr1 after removing the 30 MHz (introduced by marker AOM). The black line shows the beat signal when both Sr1 and Sr2 are at room temperature. It is close to zero as expected. The red line shows when the Sr1 at 86 K. It is expected to be off by about 2.1 Hz. B) Instability of the beat signal of the Sr1 and Sr2. As Sr1 and Sr2 used independent interrogating lasers, the instability will be limited by the worse one due to the Dick effect. We are limited by the interrogating laser of the transportable system Sr2 to about $1.5 \times 10^{-15}/\sqrt{\tau}$ as you see as a solid red line. C) Observed shift of BBR with the expectation value as a horizontal line, blue point is our measurements with its uncertainty (red: systematic, and blue: statistical). The black point is result of a the measurement in Katori group reported in [Ush15].

	MOT position		Coldfinger position	
Effect	Correction (10^{-18})	Uncertainty (10^{-18})	Correction (10^{-18})	Uncertainty (10^{-18})
BBR shift	4929	12.8	35	< 1
BBR oven	9.4	9.4	0	0
lattice scalar and tensor	-7	9	-7	9
lattice E2/M1	0	3.4	0	3.4
hyperpolarisability	-4.8	1.8	-4.8	1.8
second-order Zeeman	-32	1.3	-20	0.8
cold collisions	0	0.8	0	0.8
background gas collisions	0	4	0	4
tunnelling	0	2	0	2
line pulling	0	2	0	2
interrogation laser	0	0.1	0	0.1
optical path length error	0	0.1	0	0.1
servo error	0	1.7	0	1.7
residual Doppler shift	0	0	0	8
total	4894.6	19.1	3.2	13.2

Table 3.4: Total uncertainty budget for MOT and cold finger positions. All systematic frequency shifts are listed here with their uncertainties.

3.4.5 Conclusion

The origin of the offset frequency, which has been observed by using the MOT position as a reference as shown in Figure 3.8 is understood, it is mostly like due to residual motion of the translation stages (5.5×10^{-17} in fractional unit) and due to some systematic different between the MOT and cold finger position, the second-order Zeeman is different by 1.2×10^{-17}. The magic wavelength of the lattice laser was 2 MHz off, which caused an additional shift of less than 1×10^{-17}.

Table 3.4 summaries all known shifts and their uncertainties at the cold finger position together with that at the MOT position for comparison. At MOT position, the dominant uncertainty is due to the BBR shift which is 12.8×10^{-18}, this uncertainty has been suppressed by more than factor of ten at cold finger position at 86 K. The larger uncertainty contribution at the cold finger is due to the lattice shift (scalar, tensor and higher orders). Accurate measurement of the magic wavelength is required to suppress the uncertainty further [Kat15]. The uncertainty of the residual Doppler shift at cold finger position of 8×10^{-18} is statistical and can be reduced further by more measurements.

Chapter 4

Noise and instability of the clock

In the previous chapter I discussed the accuracy of our optical lattice clock. The other main property with an atomic clock is its instability. I will discuss in this chapter the instability of our system and all noise contributions, which degrade the stability of the lattice clock. The instability of the observed frequency is caused by random fluctuations and drifts over time. The instability of a frequency standard is characterized as follows,

$$\sigma_y(\tau) = \frac{\delta\nu}{\nu_0}\frac{1}{K\sqrt{N}}\sqrt{\frac{T_c}{\tau}}. \tag{4.1}$$

Here, $\delta\nu$ is the observed line width of the clock transition, which usually is the Fourier limit of the interrogation time ($\delta\nu \approx \frac{0.8}{T_\pi}$) [Dic88]. ν_0 is the frequency of the clock transition ${}^1S_0 - {}^3P_0$ which is in our case equal to 429228004229873.04(11) Hz [Gre16]. K is a parameter on the order of 1, that accounts for the line shape. N is the number of atoms. T_c is the cycle time, and τ is the average time. Optical lattice clocks have shown outstanding fractional frequency instabilities that are about two order of magnitude better than microwave atomic clocks and about one order of magnitude better than ion clocks because of the following reasons:

- High Q-factor ($\nu/\Delta\nu$) for better stability of the clock, where ν is the transition frequency and $\Delta\nu$ is the natural linewidth of the transition.
- High signal-to-noise ratio, as optical lattice clocks interrogate tens of hundreds of atoms simultaneously.

Several research groups have observed instabilities in their optical lattice clocks as low as $2 \times 10^{-16}/\sqrt{\tau/\mathrm{s}}$ [Al-15, Nic15, Hin13, Nic12], averaging down to the low 10^{-18}-regime. The improvement of clock stability has a strong impact on the determination of the clock's accuracy as well, since systematic frequency shifts can be evaluated with much higher accuracy in reasonable time. Furthermore, the stability of a clock also determines how practical it is for actual measurements and if, e.g., temporal variations of signals [Der14] can be observed.

The instability of a clock stems from different sources of noise contributing to the error signal detected in the clock cycle, i.e., the estimated frequency offset of the clock laser from the atomic transition, and from the Dick effect [Dic88]. The goal of this chapter is to measure and estimate each noise contribution individually and to determine the instability of our ^{87}Sr optical lattice clock and the dominant noise contribution.

4.1 Detection noise analysis

In this section, the individual noise contributions which degrade the instability of our optical lattice clock are discussed in details. For the sake of simplicity, we express all noise amplitudes in arbitrary units of the data acquisition system labeled 'counts'. The excitation probability signal is a signal which carries information about how much the clock laser is detuned from atomic transition. This signal is used to act upon the clock laser frequency (to lock the clock laser to the atomic transition). Details on cooling and trapping ^{87}Sr atoms as well as state preparation, which are required to prepare an atomic sample have been presented in the chapter 2 and in previous publications [Fal14, Fal11, Lis09].

The ^{87}Sr atoms are transferred in a superposition of the $^1S_0$ and $^3P_0$ states by the clock laser. Atoms in the ground state ($^1S_0$) are then detected by fluorescence from a resonant laser beam in standing-wave configuration on the strong 461 nm cooling transition $^1S_0 - {}^1P_1$. The fluorescence is observed by a photomultiplier tube in current mode. Its signal is amplified and digitized with an analog-to-digital converter of the data acquisition computer. This signal g is, apart from an offset o, proportional to the $^1S_0$ ground state atom number. The radiation pressure removes the atoms from the detection volume within 20 ms. After that, the atoms in the excited clock state ($^3P_0$) are detected after they have been optically pumped within few 100 μs to the $^3P_1$ state by resonant laser beams

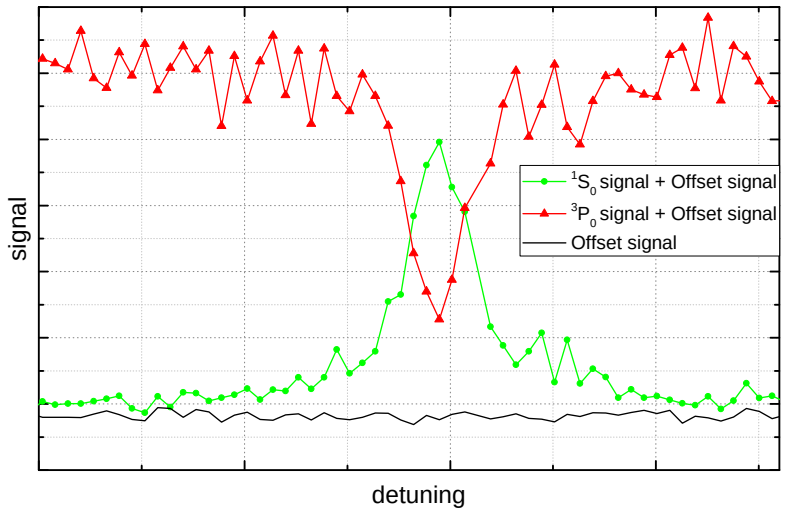

Figure 4.1: Typical spectrum of the $^1S_0 - {}^3P_0$ transition, where the signal here is in arab. unit as function of the detunning of the clock laser around the resonance. The red line shows the signal e, which refers to the atom number in excited state $^3P_0$. The green line shows the signal g, which relate to atom numbers in ground state $^1S_0$. the black line is relate to the offset background o.

(two repumper lasers at 679 nm and 707 nm) for the $^3P_0 - {}^3S_1$ and $^3P_2 - {}^3S_1$ transitions respectively. From the $^3P_1$ state the atoms then decay to the ground state $^1S_0$. The last detection pulse is used to measure the offset signal o due to stray light (S_{stray}), multiplier dark current, and electronic offsets, after removing any remaining atoms. Therefore, each of the signals g, e, and o is a sum of different contributions from fluorescence (S_{fluo}), stray light (S_{stray}), and electronic background (S_{elec}). Figure 4.1 shows typical signals of g, e, and o for a scan across the resonance. From these three signals, the atomic excitation probability p_{e} is estimated as

$$p_{\text{e}} = \frac{e - \overline{o}}{e + g - 2\overline{o}}. \tag{4.2}$$

Here, $\overline{o}$ is the running average of the offset signal o. The excitation probability, in particular its noise, can be related to the corresponding frequency excursion of the interrogation laser via the slope of the spectroscopic signal. For the case of probing the atomic resonance line at a half-width point [Dic88] using Rabi interrogation with a pulse of length T_π, the slope is

$$\frac{\mathrm{d}p_{\text{e}}}{\mathrm{d}\nu} \approx \pm 2\pi \cdot 0.30 \cdot T_\pi \tag{4.3}$$

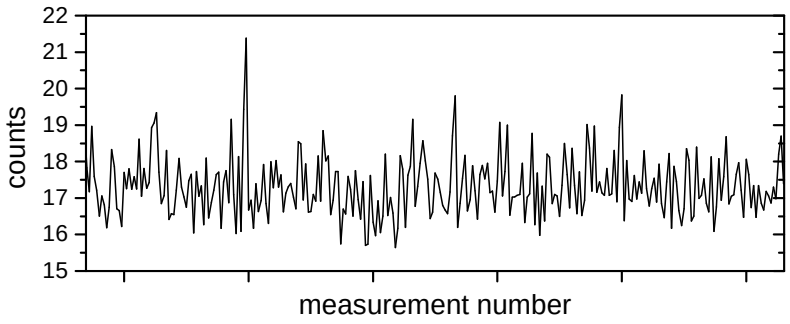

Figure 4.2: Typical electronic offset signal S_{elec} in our system.

with its sign depending on which side of the resonance is probed. A Ramsey interrogation scheme with free precession time T_{Ramsey} and short excitation pulses leads to a steeper slope of

$$\frac{\mathrm{d}p_{\mathrm{e}}}{\mathrm{d}\nu} \approx \pm 2\pi \cdot 0.5 \cdot T_{\mathrm{Ramsey}}. \tag{4.4}$$

4.1.1 Electronic noise

The electronic noise appear due to amplifier, digitizer, and dark current noise. In order to measure the electronic noise, our experiment was operated in a normal sequence but without atoms and without laser light being present. The signal, which is still detected by the photomultiplier is due to the electronic noise. The signal has been record as you see in Figure 4.2. The electronic noise will be present in the three signals, g, e, and o, but not in $\overline{o}$ (it is suppressed by averaging to a negligible level in $\overline{o}$). The standard deviation of the signal is $\sigma_{\mathrm{elec}} = 0.82$ counts, while the amplitude of the electronic offset signal $S_{\mathrm{elec}} \approx 18$ counts. We assumed that the electronic noise in the three signals g, e, and o is independent and we applied the error propagation method to calculate the total contribution of the electronic noise as follows,

$$\sigma_{p_{\mathrm{e}}(ele)} = \sqrt{\left(\frac{\mathrm{d}p_{\mathrm{e}}}{\mathrm{d}g}\sigma_{ele}\right)^2 + \left(\frac{\mathrm{d}p_{\mathrm{e}}}{\mathrm{d}e}\sigma_{ele}\right)^2 + \left(\frac{\mathrm{d}p_{\mathrm{e}}}{\mathrm{d}o}\sigma_{ele}\right)^2} \tag{4.5}$$

where,

$$\begin{aligned}\frac{\mathrm{d}p_\mathrm{e}}{\mathrm{d}g} &= \frac{\overline{o}-e}{(g+e-2\overline{o})^2}\\ \frac{\mathrm{d}p_\mathrm{e}}{\mathrm{d}e} &= \frac{g-\overline{o}}{(g+e-2\overline{o})^2}\\ \frac{\mathrm{d}p_\mathrm{e}}{\mathrm{d}\overline{o}} &= \frac{e-g}{(g+e-2\overline{o})^2}.\end{aligned} \tag{4.6}$$

The total contribution of the electronic noise depends on the fluorescence signal as shown together with shot noise contribution in Figure 4.4,

$$\sigma_{p_\mathrm{e}(ele)} \propto \frac{1}{S_\mathrm{fluo}}. \tag{4.7}$$

4.1.2 Photon shot noise

Shot noise is a result of the discrete nature of the detection of the photons, in particular, shot noise arises from the fluctuation in the detected photocurrent due to the fundamental randomness of the photon flux. Detection of photons obeys a pure Poissonian distribution, meaning that photons are completely uncorrelated which is true for classical light which we used in our laboratory (without any squeezed light [Xia87]). Thus if N photons are detected in a given period, this leads to a noise of $\sqrt{N}$. In our detection, a finite number of photons is collected by the photomultiplier tube. Thus, the signals g and e will suffer from a shot noise contribution. In order to measure the shot noise contribution, we have investigated the photon shot noise using an external flashlight as a shot noise–limited light source. For the observed white noise, the first point of the Allan deviation of the recorded data is equal to their standard deviation; we use this value as a measure of the noise to remove the influence of slow intensity variations of the flashlight (as may have happened during the measurements). The measurements were performed for different signal amplitudes. The electronic background S_elec (discussed in the previous subsection) must be removed to extract the actual 'fluorescence' signal S_fluo, i.e., the signal stemming only from detected photons. The resulting 'fluorescence' noise contribution σ_sn is shown in Fig. 4.3. The expected $\sqrt{S_\mathrm{fluo}}$-dependence of the noise amplitude σ_sn is well reproduced. From a fit we find,

$$\sigma_\mathrm{sn}(S_\mathrm{fluo}) = 0.59(2)\sqrt{S_\mathrm{fluo}}, \tag{4.8}$$

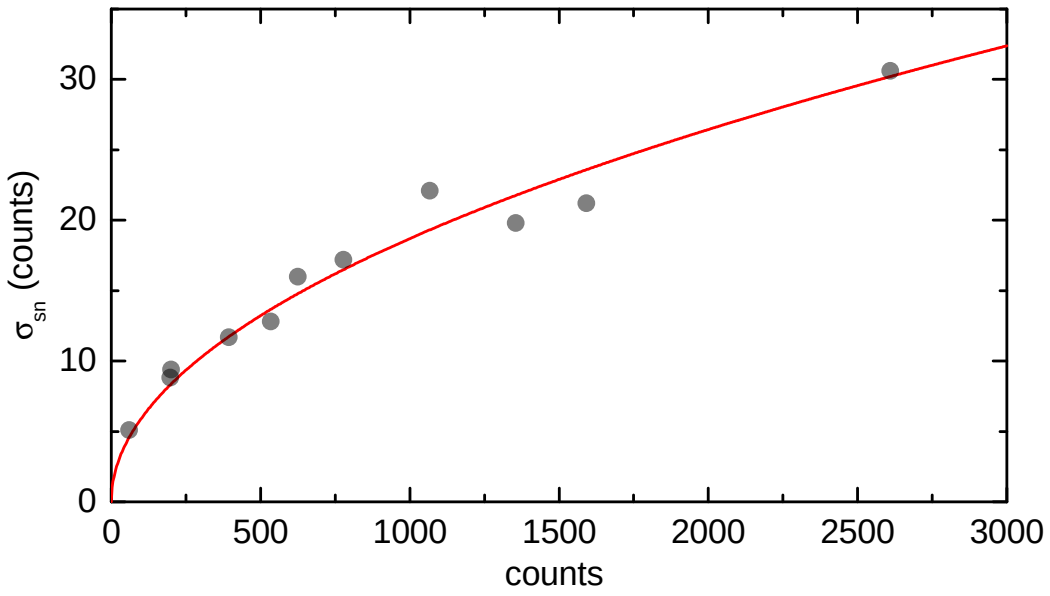

Figure 4.3: Shot noise level σ_{sn} as function of the 'fluorescence' signal S_{fluo}.. As expected shot noise level scales as $\sqrt{S_{\mathrm{fluo}}}$.

which corresponds to $S_{\mathrm{fluo}} = 0.35(3)$ counts per detected photon. Fluorescence shot noise will be present in the signals g and e with an amplitude depending on the fluorescence contribution S_{fluo} to these signals. The electronic offset S_{elec} is not subject to shot noise. As in the previous subsection, we applied the error propagation method to calculate the total contribution of the shot noise for g and e as follows

$$\sigma_{p_{\mathrm{e}}(sn)} = \sqrt{\left(\frac{\mathrm{d}p_{\mathrm{e}}}{\mathrm{d}g}\sigma_{sn}\right)^2 + \left(\frac{\mathrm{d}p_{\mathrm{e}}}{\mathrm{d}e}\sigma_{sn}\right)^2}, \tag{4.9}$$

The total noise contribution of the shot noise depends on the fluorescence signal as shown in Figure 4.4, The shot noise is proportional to the square root of the signal, thus the suppression of the shot noise scales with the inverse of the square root of the signal.

$$\sigma_{p_{\mathrm{e}}(sn)} \propto \frac{\sqrt{S_{\mathrm{fluo}}}}{S_{\mathrm{fluo}}} \propto \frac{1}{\sqrt{S_{\mathrm{fluo}}}}. \tag{4.10}$$

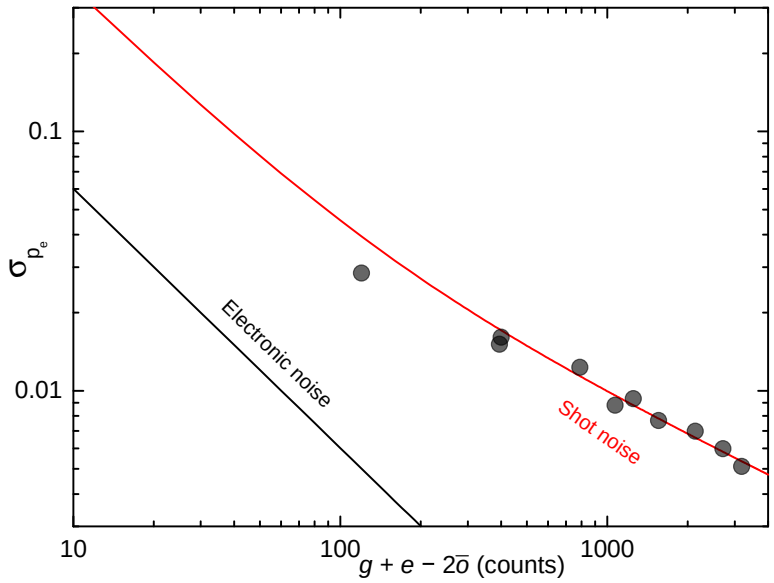

Figure 4.4: Total contribution of the shot noise (red solid line) to the excitation probability noise σ_{p_e} as function of the 'fluorescence' signal S_{fluo}. The suppression scales as $\propto \frac{1}{\sqrt{S_{\text{fluo}}}}$. The black solid line is the electronic noise contribution.

4.1.3 Detection laser noise

Intensity fluctuation

Intensity fluctuations of the detection laser at the position of the atoms lead to additional noise through the fluctuations of the spontaneous emission rate as long as the transition is not strongly saturated. The scattering rate γ of atoms in the presence of detection laser can written as

$$\gamma(s,\delta) = \frac{\Gamma}{2}\frac{s}{1+s+(\frac{2\delta}{\Gamma})^2}, \tag{4.11}$$

where Γ is the decay rate from the $^1P_1$ excited state to the $^1S_0$ ground state, $s = \frac{I}{I_{sat}}$ is the saturation parameter of the detection laser beam (with the intensity I of the detection beam and I_{sat} is the saturation intensity), and δ is the laser detuning from atomic transition.

We avoid high intensity (the saturated regime), since the radiation pressure–induced heating of the atoms reduces the reasonable interaction time and thus the detected signal. This loss of signal is not compensated by the higher photon scattering rate, and the detection would be less efficient.

Intensity fluctuations may arise from two sources, power fluctuation and pointing instability of the detection laser. We measured the power fluctuations of the detection laser beam in a similar procedure as for the shot noise measurements, except that we used stray light from the detection laser instead of an external flashlight. From these measurements we have found that, the dependence of the noise level on the detection beam power is very similar to the one presented in Fig. 4.3. In particular, we have observed no significant noise contribution with a linear dependence on laser power and thus conclude that laser power noise on short time scales, which would result in such a contribution, can be neglected. This is corroborated further by direct measurements of the laser power. Our detection beam is delivered by a fiber and collimated to a diameter of about 2 mm, the setup comprises only a short free-space path on the order of 50 cm; we have analyzed its pointing instability and found it to be negligible on relevant time scales. We also note that the shot noise of the detection beam with a power of about 400 μW is negligible.

Laser stray light (S_{stray}) adds a shot-noise contribution to the signals g and e according to Eq. 4.8, whereas its noise contribution to the offset is suppressed by the use of $\overline{o}$.

Frequency fluctuation

The transition ${}^1S_0 - {}^1P_1$ is used to derived spectroscopic signal with a resonant beam at 461 nm. The light beam is generated from a frequency-doubled diode laser system that also produces the laser beams for laser cooling and Zeeman slowing. The fundamental frequency of the laser system is stabilized to a high-finesse, 10 cm long ultra-low expansion (ULE) glass resonator. This ULE resonator has a resonance line width of less than 100 kHz; we estimate in-lock frequency fluctuations on the kilohertz level from the in-loop error signal. The laser line width of the resonator is very narrow compared to the 32 MHz line width of the ${}^1S_0 - {}^1P_1$ detection transition, frequency noise of the detection laser does not contribute significantly to the detection noise.

4.1.4 Quantum projection noise

Quantum projection noise is a fundamental limit of the atomic clock stability for uncorrelated states of the atom. It arises when an atom is prepared in a superposition of the

two states $|0\rangle$ and $|1\rangle$. During and due to detection the projection of the superposition of the states will collapse onto one of the states, thus the result of the measurements cannot be predicted with certainty. Let us consider a two-level system with states $|0\rangle$ and $|1\rangle$, ground state and excited state, respectively and separated by $\hbar\omega_{01}$, e.g., in an atom or an ion. The internal state can be prepared in superposition of the eigenstates by interrogating with an electromagnetic field with frequency ω, the coupling between the internal states in present of the electromagnetic field has the following matrix element,

$$\langle\Psi_0|S|\Psi_1\rangle = \hbar b e^{iwt}. \tag{4.12}$$

After a time t of interaction between the atom and the electromagnetic field, the atom will be in a superposition state as follows [Ita93],

$$|\Psi(t)\rangle = C_0(t)\,|\Psi_0\rangle + C_1(t)\,|\Psi_1\rangle \tag{4.13}$$

where $|C_0(t)|^2$ and $|C_1(t)|^2$ are the probabilities to find the atom in state $|\Psi_0\rangle$ and in state $|\Psi_1\rangle$

$$|\Psi(t)\rangle = [i\frac{\omega_{01}-\omega}{\Omega}\sin(\frac{\Omega t}{2}) + \cos(\frac{\Omega t}{2})]e^{i\frac{1}{2}(\omega_{01}-\omega)t}\,|\Psi_0\rangle - i\frac{2b}{\Omega}\sin(\frac{\Omega t}{2})e^{i\frac{1}{2}(\omega_{01}-\omega)t}\,|\Psi_1\rangle \tag{4.14}$$

were ω_{01} is the atomic frequency and $\Omega = \sqrt{(\omega_{01}-\omega^2)+(2b)^2}$.

If $\omega_{01} = \omega$ then we will get

$$|C_0(t)|^2 = p_0 = \cos^2(\frac{\Omega t}{2}) \tag{4.15}$$

and

$$|C_1(t)|^2 = p_1 = \sin^2(\frac{\Omega t}{2}). \tag{4.16}$$

By varying the pulse area Ωt we can change the excitation probability from 0 through 1 for state ψ_0 (ground state) and state ψ_1 (excited state). The interesting part here is that if the excitation probability is 50 % for ground and excited states, then the result of the measurement cannot be predicted with certainty, because the wave function of the atom is collapses (reduced) into one of the eigenstates due to the detection process. The variance of the excitation probability can be calculated as follows,

$$\begin{aligned}\sigma^2(p_\mathrm{e}) &= \left\langle (\hat{p}_\mathrm{e} - \langle \hat{p}_\mathrm{e} \rangle)^2 \right\rangle \\ &= \left\langle (\hat{p}_\mathrm{e}^2 - 2\langle \hat{p}_\mathrm{e} \rangle \hat{p}_\mathrm{e} + (\langle \hat{p}_\mathrm{e} \rangle)^2) \right\rangle \\ &= \left\langle \hat{p}_\mathrm{e}^2 \right\rangle - \langle \hat{p}_\mathrm{e} \rangle^2 \end{aligned} \tag{4.17}$$

Using projection operator $\hat{p}_\mathrm{e} \equiv |e\rangle\langle e|$ we find $\hat{p}_\mathrm{e}^2 = (|e\rangle\langle e|)(|e\rangle\langle e|) = |e\rangle\langle e| = \hat{p}_\mathrm{e}$ where $\langle e|e\rangle = 1$. This leads with Eq. (4.17)

$$\sigma^2(p_\mathrm{e}) = \langle p_\mathrm{e} \rangle - \langle p_\mathrm{e} \rangle^2, = \langle p_\mathrm{e} \rangle (1 - \langle p_\mathrm{e} \rangle) = p_\mathrm{e}(1 - p_\mathrm{e}) \tag{4.18}$$

For many atoms N, Eq. (4.18) can be rewrite as,

$$\begin{aligned}\sigma^2(p_\mathrm{e}) &= N p_\mathrm{e}(1 - p_\mathrm{e}) \\ \sigma(p_\mathrm{e}) &= \sqrt{N p_\mathrm{e}(1 - p_\mathrm{e})}. \end{aligned} \tag{4.19}$$

As you see from Eq. (4.19), the measurement will have maximum uncertainty if the excitation probability p_e equal to 0.5 and the uncertainty reaches a minimum at excitation probability 0 and 1. The Figure 4.5 is shown total noise of the excitation probability with difference excitation probability (the excitation probability is calculated according to Eq. (4.2)). The black line corresponds to p_e close to 0 (meaning all atoms are in ground state), this leads to a minimal noise contribution from QPN. The same is the case p_e close to 1 (blue line) where all atoms are in excited state. When p_e close to 0.5 this leads to a maximum noise contribution from QPN (red line). Of course what you see in Figure 4.5 is the total noise of excitation probability, this means there is an influence from other noises.

At p_e close to 0.5, when clock laser is detuned from resonance $\omega_\mathrm{l} = \omega_0$ to mid of fringe $\omega_\mathrm{l} = \omega_0 \pm \frac{1}{2}\mathrm{FWHM}$, thus p_e will be sensitive to clock laser noise. This usually exploited in a stabilization sequence (the clock laser is locked at the fringe of the line $p_\mathrm{e} = 0.5$), at that point, QPN and clock laser noise are at maximum. In order to separate QPN from clock laser noise and to see its $\sqrt{N}$ dependence as in Eq.(4.19), the clock laser noise has to be suppressed. In order to become insensitive to frequency noise of the clock laser, we prepared a coherent superposition state by using a resonant $\pi/2$-Rabi

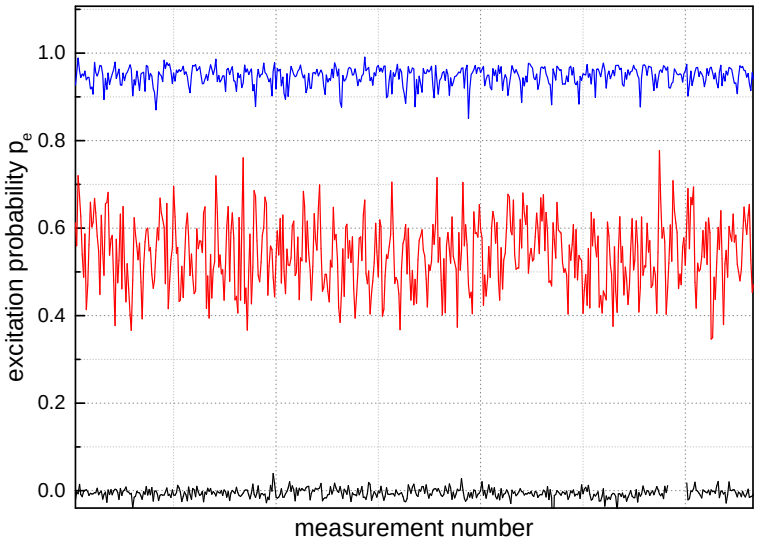

Figure 4.5: This figure shows the observed noise of excitation probability when the clock transition is probed at different positions of the resonance curve.

pulse instead of Rabi excitation with a π-pulse at a half-width frequency detuning. A pulse length of $T_{\pi/2} = 10.5$ ms was chosen. Figure 4.6 shows the total noise in our system for both cases when atoms are sensitive (insensitivity) to the frequency noise of the interrogation laser. The excitation probability is determined according to Eq. 4.2 and the noise of the excitation probability σ_{p_e} is determined by the standard deviation of the excitation probability. Fig. 4.7 is showing the noise of the excitation probability σ_{p_e} (in case of a resonant $\pi/2$-Rabi pulse, where clock laser frequency noise is mostly suppressed) multiplied by the signal amplitude $g + e - 2\overline{o}$ as a function of the signal amplitude $g + e - 2\overline{o}$. To which extent quantum projection noise is dominant in our setup and if residual laser frequency noise affected the data will only become apparent with the combined noise analysis in next section.

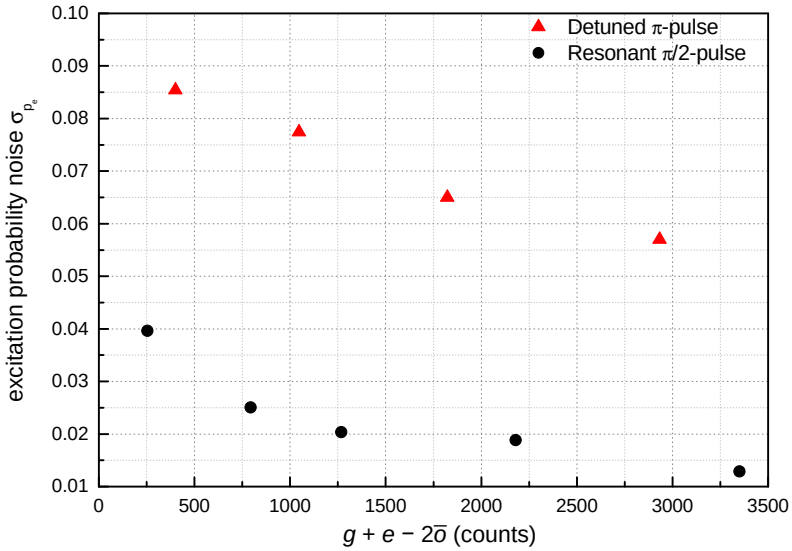

Figure 4.6: Observed noise of the excitation probability as a function of atom number. Red triangles show data with clock laser noise obtained by preparing a coherent superposition state by Rabi excitation with a π-pulse at a half-width frequency detuning with a pulse length of $T_\pi = 21$ ms. Black circles show data with suppressed clock laser noise by preparing a coherent superposition state by using a resonant $\pi/2$-Rabi pulse with a pulse length of $T_{\pi/2} = 10.5$ ms.

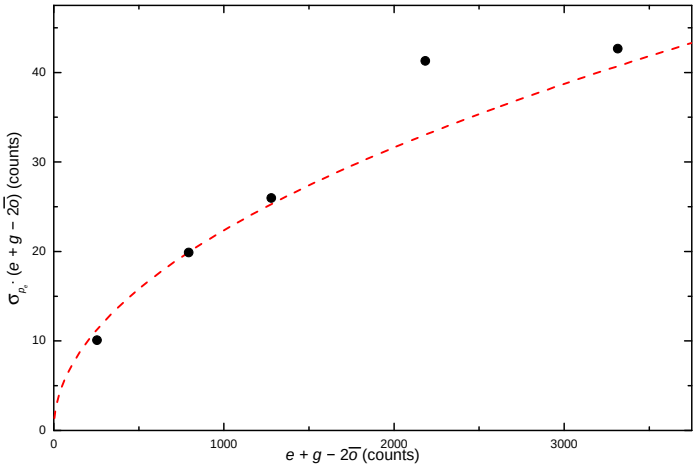

Figure 4.7: Excitation probability noise with suppressed laser frequency noise σ_{p_e} at $p_e = 0.5$ multiplied by the signal amplitude $g + e - 2\bar{o}$ as a function of atom numbers. Atoms are prepared in a superposition of $^1S_0$ and $^3P_0$ states by a frequency-insensitive resonant $\pi/2$-pulse. The dashed line shows a fit according to Eq. 4.19.

4.1.5 Detection noise model

Measuring each noise individually allows us to develop a noise model and to determine which type of noise limits our system. Our model is based on the following assumptions:

- Independent contributions to p_e from QPN and other noise sources.
- QPN leads to anti-correlated noise in g and e.
- Noise on $\overline{o}$ is suppressed to a negligible level by averaging.

Then we can write the total noise as follows

$$\sigma_{p_\mathrm{e}} = \sqrt{\sum_i \left(\frac{\mathrm{d}p_\mathrm{e}}{\mathrm{d}g}\sigma_{g,i}\right)^2 + \sum_i \left(\frac{\mathrm{d}p_\mathrm{e}}{\mathrm{d}e}\sigma_{e,i}\right)^2 + \frac{\sigma^2_\mathrm{QPN}}{N^2}}. \tag{4.20}$$

Figure 4.8 shows contributions from all noise sources (except clock laser noise) to the excitation probability noise σ_{p_e} as function to the atom number. We see that the noise model agrees very well with the observed measurements noise (see Figure 4.7). The QPN has been calculated by Eq. 4.19 for σ_{p_e} and using a conversion factor of 0.65 between the atom number and counts. From this analysis, our system is QPN limited if more than 200 counts ($0.65 \cdot 200$ atoms) are used. Operating our lattice clock with 300 atoms leads to excitation probability noise $\sigma_{p_\mathrm{e}} = 0.03$. To relate the excitation probability noise σ_{p_e} to the frequency noise of the stabilization's error signal, we use Eq. 4.3 with a typical pulse duration of 640 ms, thus frequency instability is calculated to be about $6 \times 10^{-17}/\sqrt{\tau/\mathrm{s}}$. This result is without taking into account the degradation of the instability due to frequency noise of the interrogation laser, which going to be my next subsection.

4.2 Clock laser noise (Dick effect)

In the previous section I discussed the noise contributions due to the state detection; now we will discuss the noise contribution from the interrogation laser. The Dick effect [Dic88] is known as an aliasing of the interrogation laser noise by the atoms. Normal operation of atomic clocks consists of two phases as you see in Figure 4.9, a preparation phase, where

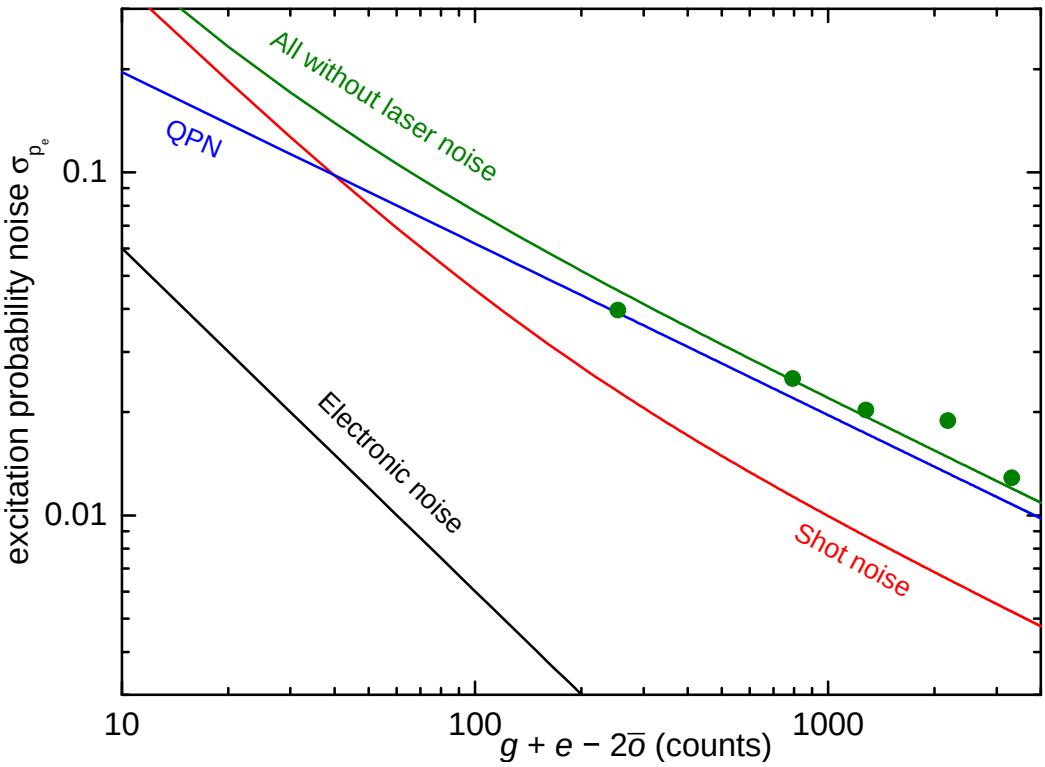

Figure 4.8: The figure shows the excitation probability noise as a function of the total atom number. The green points represent the total experimental noise of the excitation probability with suppressed sensitivity to laser frequency noise ($\pi/2$-pulses, as described in the text). The green solid line represents the summed noise according to Eq. 4.20. The good agreement with the experimental data demonstrates the completeness of the model and the absence of laser noise in the data. The blue solid line shows the calculated QPN with a detection efficiency of 0.65 atoms/count. The red solid line depicts the shot noise, the calculation includes the noise of a typical background of 70 counts due to detection laser stray light. The black solid line represents the electronic noise.

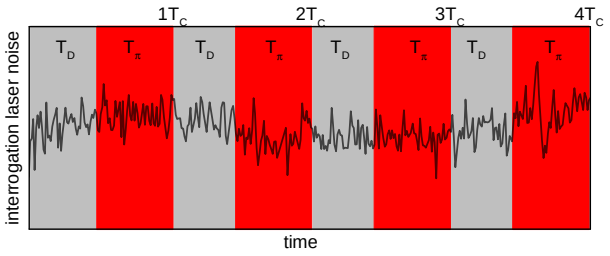

Figure 4.9: Simplified picture of the normal sequence of our optical lattice clock. Each single cycle T_c consist of a preparation phase T_D, called dark time, and an interrogation phase T_π. During the dark time T_D there is no information on laser frequency noise, since interrogating laser is off during the dark time.

atoms are cooled, trapped, and detected. The second phase is the interrogation of the clock transition. During the preparation phase, the information about the interrogation laser noise is lost (since the interrogation laser does not interact with the atoms) [Wes10b]. Only during the interrogation phase we observed the interrogation laser frequency noise. This means that we compensated the laser noise only partially. In order to suppress the Dick effect, the obvious solution is to a build better laser, which has low spectral laser frequency noise. Such ideas require pre-stabilization of the interrogation laser to a reference cavity (like passive cavities are common used [Häf15b, Kes12]). The second approach is the reject the Dick effect as common mode noise by synchronously operating two independent atomic clocks with a shared interrogation laser [Hin13, Ush15]. The third approach is to use multi-Ramsey sequence, to enhance the duty cycle at a given clock laser performance by interrogation time beyond the coherence time of the clock laser, this methods has been tested with our clock (in preparation), and a similar approach is suggested in [Hum16].

4.2.1 Sensitivity function

The sensitivity function $w(t)$ is used to describe the change in excitation probability due to frequency noise of the interrogation laser

$$\delta p_e = \frac{1}{2}\int_0^T 2\pi\ \delta\nu\,(t)\cdot w\,(t)\,\mathrm{d}t. \tag{4.21}$$

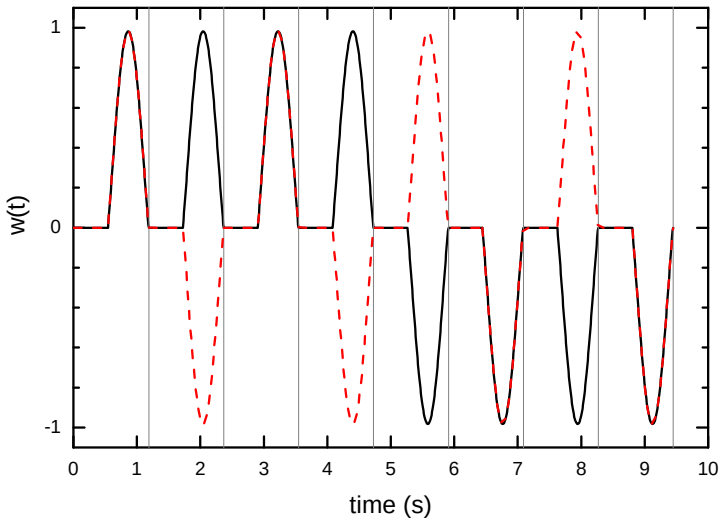

Figure 4.10: Sensitivity function $w(t)$ of interleaved stabilizations with parameters $T_c = T_\pi + T_D = 1.18$ s ($T_\pi = 0.64$ s, $T_D = 0.54$ s). The solid line shows for the case of a lumped interleaved arrangement, where the sign is reversed between the first and last four. The dashed line shows a distributed arrangement for an interleaved interrogation. Vertical grey lines indicate multiples of T_c.

In case of Rabi interrogation with a π pulse of length T_π centered at $t = \frac{T_\pi}{2}$ the sensitivity function can be as written [Fal12],

$$w(t) = \begin{cases} \sin^2\vartheta \ \cos\vartheta \times [(1-\cos\Omega_2)\sin\Omega_1 \ + (1-\cos\Omega_1)\sin\Omega_2] & \text{during pulse,} \\ 0 & \text{elsewhere} \end{cases} \tag{4.22}$$

with

$$\vartheta = \frac{\pi}{2} - \arctan\left(2T_\pi\Delta\right) \tag{4.23}$$

and

$$\begin{aligned} \Omega_1 &= \pi\sqrt{1+(2T_\pi\Delta)^2} \times \frac{t}{T_\pi} \\ \Omega_2 &= \pi\sqrt{1+(2T_\pi\Delta)^2} \times \frac{T_\pi - t}{T_\pi}, \end{aligned} \tag{4.24}$$

where Δ is the detuning of the interrogation laser from resonance. The Fourier components of the sensitivity function can be written as,

$$g_{\mathrm{k}}(t) \;=\; \int_0^T w(t) e^{\frac{-2i\pi kt}{T}} \mathrm{d}t. \tag{4.25}$$

for k=0,

$$g_0(t) \;=\; \int_0^T w(t) \mathrm{d}t. \tag{4.26}$$

Figure 4.10 shows time-domain sensitivity function according to (Eq. 4.22) (for Rabi interrogation) for the case of interleavd stabilization, which consists of eight pulses with dead time in between. As you see the sensitivity function $w(t)$ is zero during the dead time and it is behavior like a sine wave square during the interrogation time according to (Eq. 4.22).

4.2.2 Dick effect for our interrogation laser

The frequency instability caused by frequency aliasing of the interrogation laser can be estimated as [Dic88, San98],

$$\sigma^2_{y,\mathrm{Dick}}(\tau) = \frac{1}{\tau} \frac{1}{|g_0|^2} \sum_{k=1}^{\infty} S_y(k/T) \, |g_k|^2 \,, \tag{4.27}$$

where $T = nT_{\mathrm{c}}$, and n is the number of interrogations in each stabilization cycle. The cycle duration T_{c} consists of the preparation time T_{D} and the interrogation time T_π. S_y is the laser's single-sided power spectral density. It has been presented in [Häf15b] by a three-cornered-hat comparisons with other lasers. g_k are the Fourier coefficients of the sensitivity function $w(t)$ Eqs.(4.25, 4.26) and it is normalized by the dc Fourier coefficient g_0. For interleaved stabilizations, the frequency noise of the interrogation laser is correlated between the interleaved stabilizations. Thus the Dick effect cannot be treated independently for each of the stabilizations. The Dick effect for the difference between the two interleaved stabilization has been derived and then Eq.(4.27) is evaluated for

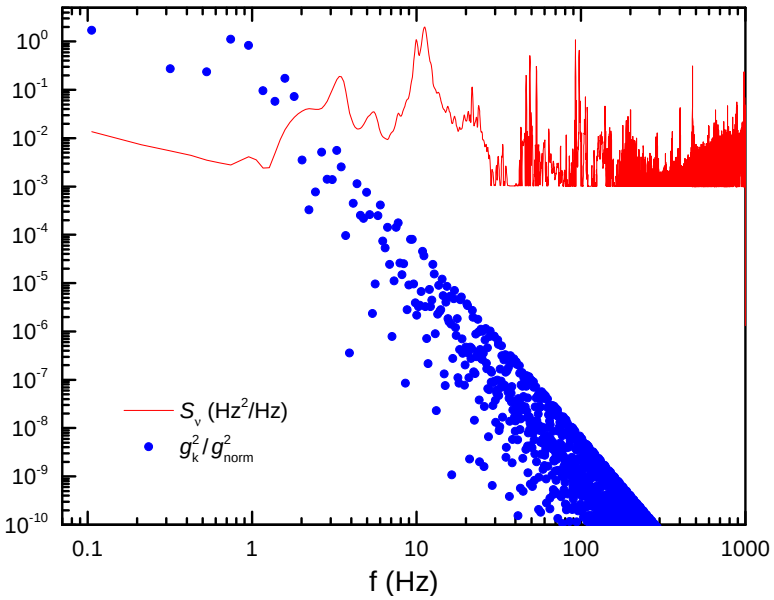

Figure 4.11: The figure shows the spectral power density of frequency fluctuations $S_\nu = \nu_0^2 S_y$ of the interrogation laser (red line), measured by three-cornered-hat comparisons with other lasers. The blue circles are Fourier components g_k^2/g_{norm}^2 for $k > 0$ for interleaved stabilizations using our experimental parameter values mentioned in the text.

interleaved stabilization with τ=1 s, and $T_c = T_\pi + T_D = 1.18$ s ($T_\pi = 0.64$ s, $T_D = 0.54$ s,) and replacing g_0 by g_{norm}, where g_{norm} can be written as,

$$g_{\text{norm}} = \int_0^T \frac{1}{2} |w(t)| \, \mathrm{d}t. \tag{4.28}$$

Figure 4.11 shows single-sided power spectral density of the frequency fluctuation (red line). The blue points are the normalized Fourier coefficients g_k in case of an interleaved stabilization for the experimental parameter mentioned above. The partial sum noise contribution due to Dick effect is plotted in Figure 4.12 for different stabilization scenarios. For interleaved stabilizations with lumped interleaved arrangement (blue filled circles), the Dick effect has a larger influence on the instability of our system, which is dominated by noise at frequencies between 1 to 10 Hz. The influence of the Dick effect in interleaved stabilizations can be suppress by 20 % (red open circles) by modifying the distribution sequence of the cycles instead of a lumped arrangement (as seen in Figure 4.10), this can be done by interleaving the interrogation sequences of each stabilization in-

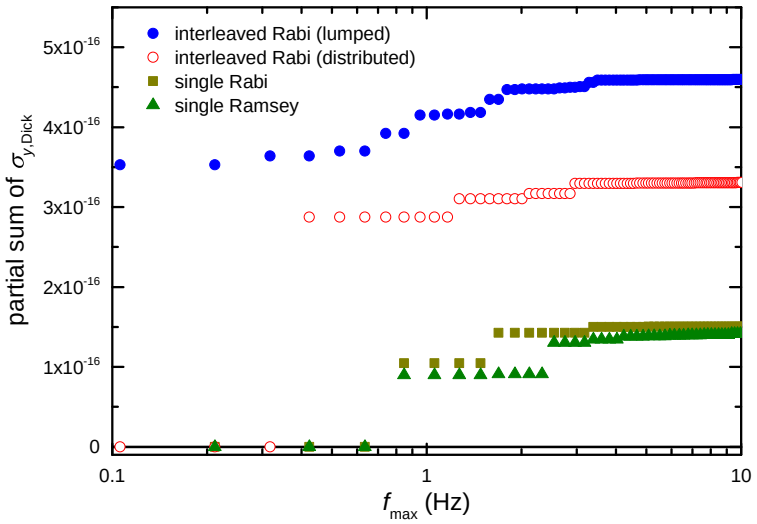

Figure 4.12: Partial sums of the Dick effect contribution to the frequency instability as a function of the maximum Fourier frequency components $f_{max} = \frac{k_{max}}{T}$ for different stabilization scenarios (described in the text).

stead of arranging them in blocks of four. For a single stabilization (dark yellow squares) using Rabi interrogation g_1, g_2, and g_3 are zero because of the symmetry of the single stabilization but g_4 is not zero and it is the dominant one in a single stabilization. The green triangles show the alternative case of using Ramsey interrogation with $\pi/2$ pulses of 100 ms in length.

4.3 Total instability of our ^{87}Sr lattice clock

Now we are at a point where we can estimate how much the total instability of our ^{87}Sr lattice clock, based on our detection noise model and the Dick effect analysis by adding them in quadrature

$$\sigma_{y,Total} = \sqrt{\sigma^2_{y,\mathrm{Dick}} + \sigma^2_{y,\mathrm{Detection}}}. \tag{4.29}$$

In order to measure our instability in a single stabilization (operation mode) we have to compare our clock with other clocks that have the same (or better) instability. Unfortunately, we do not have this opportunity in our laboratory yet. We overcome this problem by comparing by performing a self-comparsion using by interleaved stabilization (details

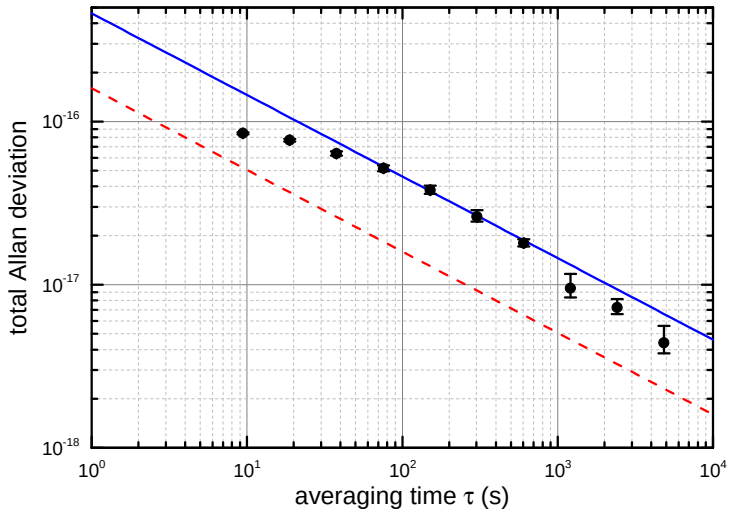

Figure 4.13: Instability of our ^{87}Sr lattice clock as function of average time. Black circles are observed instability for the difference between two interleaved stabilizations. Blue solid line $4.7 \times 10^{-16}/\sqrt{\tau}$ is the instability inferred from our analysis for interleaved stabilizations. Red dashed line $1.6 \times 10^{-16}/\sqrt{\tau}$ is the instability for the single stabilization (operation mode).

on the interleaved stabilization in section 2.6). The instability in interleaved stabilization mode is represented in Figure 4.13 by the Allan deviation of the difference signal between both stabilizations. It has instability of $4.7 \times 10^{-16}/\sqrt{\tau}$ with 360 atoms and cycle parameters $T_c = T_\pi + T_D = 1.18$ s ($T_\pi = 0.64$ s, $T_D = 0.54$ s). Comparing with our analysis of the Dick effect and detection noise model, it agrees very well (blue solid line), where the Dick effect induced instability is $4.6 \times 10^{-16}/\sqrt{\tau}$ (see blue points in Figure 4.12) and the detection noise adds $\sqrt{2}\times\ 6 \times 10^{-17}/\sqrt{\tau}$ (from detection noise model see 4.1.5). We treat the detection noise (in interleaved stabilizations) as uncorrelated which introduces the factor $\sqrt{2}$. From this result, we can estimate the instability in a single stabilization (operation mode) with 300 atoms to be $1.6 \times 10^{-16}/\sqrt{\tau}$ (red dashed line in figure 4.13), with a contribution of $1.5 \times 10^{-16}/\sqrt{\tau}$ from the Dick effect (see dark yellow points in Figure 4.12) and $6 \times 10^{-17}/\sqrt{\tau}$ from the detection noise model.

Chapter 5

Applications of optical clocks

In previous two chapters I discussed the accuracy and instability of the optical lattice clock. During this chapter I will present some applications of the optical clocks. Time and frequency measurements have very large range of applications both in fundamental science and technologies. Some of these applications require the state of the art technology, for example a redefinition of the SI second [Rie15, Gil11], test of laws of physics (like time variation of the some fundamental constant [Pei04, Ros08, Hun14]), test of the special and general relativity [Sch09, Cho10], space clock missions [Sch06], and dark matter and dark energy [Der14, Arv15].

The chapter is organized as following; first I will present the absolute frequency measurements of the clock transition $^1S_0 - {}^3P_0$ in ^{87}Sr. Then I will present comparisons between the Sr clocks at PTB (Braunschweig) and SYRTE (Paris) via a fiber link and after that I will present frequency ratio measurements between our clock and a single $^{171}Yb^+$ ion clock [Hun16], which have been carried out at PTB.

5.1 Absolute frequency measurements

During this section [CIP15], absolute frequency measurements of the $^1S_0 - {}^3P_0$ transition in ^{87}Sr atoms are presented, We measured it in 2011, 2012, 2014, and 2015 (last two of them was during my PhD time). Absolute frequency measurements of the $^1S_0 - {}^3P_0$ transition and the agreements between them and between the measurements performed in different

laboratories worldwide are an essential step for redefinition the second based on optical clocks. ^{87}Sr atom is recommended by the CIPM as one of a secondary representation of the second [CIP15].

During next subsections I will give short introduction on the frequency comb, which is an essential tool in these measurements. Then I will give details on the absolute frequency measurements done on 2012 and 2015. For absolute frequency measurements on 2011 can be found in [Fal11] and for 2014 measurement, it is similar to 2015 measurement.

5.1.1 Frequency comb

Frequency comb is an accurate tool to measure high frequencies like in visible range. It is used to determine frequency ratios, both between two optical and optical-microwave. I will discuss very briefly general concept of the frequency comb, more details can be found in [Hän06, Cun01, For07]. The frequency comb is a mode-locked femotsecond (fs) pulsed laser. It generates series of pulses with a repetition rate f_{rep}, which is given by the inverse of the round trip time inside the cavity laser. These train of pulses have two degrees of freedom; the repetition rate and the relative phase between the envelope packet and the carrier wave, which called it, the carrier envelope offset f_{CEO}. In order to convert from time domain to frequency domain, a Fourier transform is applied to the laser output, thus the pulses are transformed to a comb of many frequencies. The spacing between them is given by the repetition rate. The frequency of any comb mode can be written as,

$$\nu_m = m f_{rep} + f_{CEO}. \tag{5.1}$$

Here m is an integer number (in order of 10^6). The repetition rate (f_{rep}) can be measured accurately with a photodetector (the repetition rate is between 100 MHz to 1 GHz). The shift of the frequency comb f_{CEO} can be also measured as following: A comb mode in the frequency spectrum of the comb at $\nu_m = m f_{ref} + f_{CEO}$ is frequency doubled by a nonlinear crystal. The frequency doubled has then a frequency of $\nu_{2m} = 2m f_{ref} + f_{CEO}$, thus the difference between $2\nu_m - \nu_{2m}$ is equal to f_{CEO}. Thus both f_{rep} and f_{CEO} can be measured and stabilized at high level of precision and accuracy. Now any unknown laser

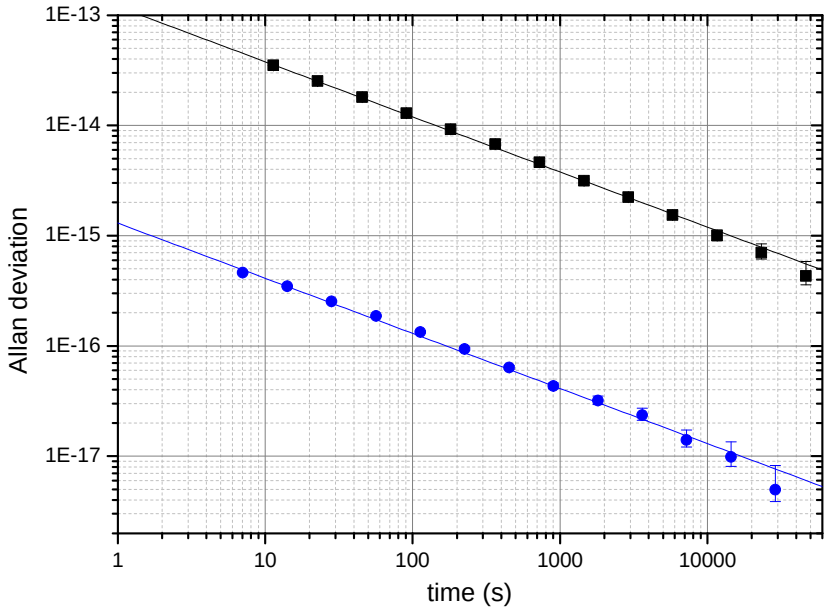

Figure 5.1: Allan deviation of the frequency measurements: The black squares are the instability of the Cs − Yb^+ ratio, which averaging down with $1.2 \times 10^{-13}/\sqrt{\tau}$ (black line). The blue circles are the instability of the Sr clock of $1.3 \times 10^{-15}/\sqrt{\tau}$ (blue line) for an interleaved stabilization from [Fal14].

frequency can be measured by measured beat signal f_{beat} between the unknown laser and nearest mode comb. The laser frequency is determined as following,

$$\nu = m f_{\mathrm{rep}} + f_{\mathrm{CEO}} \pm f_{\mathrm{beat}}, \tag{5.2}$$

where f_{beat} is the heterodyne beat frequency, which can be positive or negative sign.

In our laboratory, the frequency comb is a 1.5 μm Er-doped femtosecond fiber frequency comb with repetition rate f_{rep} = 250 MHz and f_{CEO}= 25 MHz and m = 1694020 (for the clock laser 698 nm). f_{rep} and f_{CEO} are stabilized to 100 MHz reference signal from H-Maser. The H-Maser is calibrated continuously by the CSF1 and CSF2 primary Cs fountain clocks [Wey01, Wey02, Ger10, Wey12].

5.1.2 December 2012 measurement of the $^1S_0 - {}^3P_0$ transition

From 12 to 18 December 2012, the frequency of the $^1S_0 - {}^3P_0$ transition of the ^{87}Sr atom was measured. In order to measure the frequency of the $^1S_0 - {}^3P_0$ transition related to

the SI unit, The frequency has to compare to the CSF1 and CSF2 primary Cs fountain clocks [1]. This comparison between Cs and Sr clocks has been performed via frequency comb. The uncertainty of these measurements is limited statistically due to Cs fountain clocks (instability of the Cs fountain clock is two order of magnitude higher than the Sr lattice clock). Long averaging time is required to reduce the statistical uncertainty of the measurements, for this reason the single ion clock $^{171}Yb^{+}$ based on the $^{2}S_{1/2}(F = 0) -^{2} F_{7/2}(F = 3)$ transition [Hun12b, Hun12a, Hun16] is used as a flywheel to bridge gaps in the operation of the Sr lattice clock (at that time the up time of the single ion clock $^{171}Yb^{+}$ was better than Sr lattice clock), thus extension the averaging time for $Cs - Sr$ ratio is possible if the $Sr - Yb^{+}$ ratio is more stable than $Sr - Cs$ ratio.

The SCF1 and CSF2 were running about 98% and during that time, the single ion clock $^{171}Yb^{+}$ has overlapping time with Cs fountain clocks of approximately 350 000 s. The Sr lattice clock has overlapping time of 165 000 s with Cs fountain clocks. The result of the single ion clock $^{171}Yb^{+}$ against Cs fountains is showing white frequency noise dependence (averaging with $\frac{1}{\sqrt{\tau}}$) with statistical uncertainty of 2.5×10^{-16} for CSF1 and 2×10^{-16} for CSF2 (as seen in Figure 5.1) and the systematic uncertainty is 7.3×10^{-16} for CSF1 and 4×10^{-16} for CSF2. The averaging of the systematic and statistical uncertainties is lead to 3.9×10^{-16}. During this time, the frequency ratio between the single ion clock $^{171}Yb^{+}$ and ^{87}Sr lattice clock was measured with averaging time of 165 000 s, the statistical uncertainty of the frequency ratio was 1.3×10^{-17} and it was averaging down clearly with $\frac{1}{\sqrt{\tau}}$ dependence. Now, from these measurements. Thus the averaging time of the $Sr - Cs$ ratio with 165 000 s could extend by $Sr - Yb^{+} - Cs$ ratios to 350 000 s because of better instability of $Sr - Yb^{+}$ ratio. The absolute frequency of the $^{1}S_0 - {}^{3}P_0$ transition in ^{87}Sr atoms was measured to be 429 228 004 229 873.13 (17) Hz. The total uncertainty (statistical and systematic) of this measurements is 0.17 Hz. The dominated uncertainty is due to Cs fountain clocks during the comparison between $^{171}Yb^{+}$ against Cs clocks, which was 0.166 Hz. The systematic uncertainty of the ^{87}Sr lattice clock was 0.022 Hz. The statistical uncertainty of the frequency ratio between ^{87}Sr lattice clock against $^{171}Yb^{+}$ clock was 0.0056 Hz and transfer link has uncertainty of 0.0043 Hz and the gravitational red shift due to the height difference between the ^{87}Sr atoms and Cs

[1] The primary Cs fountain clocks CSF1, CSF2, and H-Masers are used in these measurements from our colleagues at Time and Frequency department 4.4 at PTB (group of Dr. Stefan Weyers).

atoms has been corrected with in 6 mm uncertainty (which caused negligible effect in frequency 0.3 mHz). All these uncertainties are added in quadrature to be 0.17 Hz.

5.1.3 June 2015 measurement of the $^1S_0 - {}^3P_0$ transition

In June 2015, the frequency of the $^1S_0 - {}^3P_0$ transition of ^{87}Sr atoms was again measured. The ^{87}Sr lattice clock had been improved both in accuracy and stability, the systematic uncertainty had been evaluated to be 1.9×10^{-17} (details see chapter 3). The instability had also reduced by using a new ultrastable interrogation laser [Häf15b], thus the instability of $1.6 \times 10^{-16}/\sqrt{\tau}$ has been estimated (more details on chapter 4). For this absolute frequency measurement, the statistical uncertainty of the measurements is reduced because of two reasons, first of all the measurements itself was almost one month long with an uptime of about 70% (operation time of the Sr lattice clock). The second of all we used a H-maser as a flywheel to cover gaps in the operation of the Sr lattice clock, thus longer averaging time can be apply. The total statistical uncertainty can be written as the following,

$$\sigma_{\text{statistical}} = \sqrt{\sigma^2_{\text{Sr}}(T_{\text{Sr}}) + \sigma^2_{\text{Cs}}(T_{\text{ext.}}) + \sigma^2_{\text{ext.}}(T_{\text{ext.}})}, \tag{5.3}$$

where $\sigma_{\text{Sr}}(T_{\text{Sr}})$ is the statistical uncertainty of the Sr clock measurements, $\sigma_{\text{Cs}}(T_{\text{ext.}})$ is the statistical uncertainty of the Cs fountain clock measurements with extension time ($T_{\text{ext.}}$), $\sigma_{\text{ext.}}(T_{\text{ext.}})$ is an additional uncertainty due to the extrapolation of the mean flywheel frequency of the H-maser when the averaging time is extended from T_{Sr} to $T_{\text{ext.}}$. $\sigma_{\text{ext.}}(T_{\text{ext.}})$ is calculated with a model which uses the flywheel's spectrum of the frequency fluctuation $S(f)$ with help of Parseval's theorem as following: The averaging $\overline{\text{y}_{\text{T}_\text{i}}}$ of the normalized flywheel frequency over a gate time T_i can be written as,

$$\overline{\text{y}_{\text{T}_\text{i}}} = \int_{-\infty}^{+\infty} y(t) g_{T_i}(t) dt, \tag{5.4}$$

where $y(t)$ is the fractional frequency of the H-maser ($\frac{\delta\nu}{\nu_0}$). $g_{\text{T(t)}}$ is the weighting function, which can be written as,

$$g_T(t) = \begin{cases} 1/T_i & \text{for } t \in T_i \\ 0 & \text{elsewhere} \end{cases}. \tag{5.5}$$

The difference of the mean flywheel frequency averaged for two sets of period like T_1 and T_2 is written as,

$$\delta y_{\text{ext}} = \overline{\text{y}_{\text{T}_2}} - \overline{\text{y}_{\text{T}_1}}. \tag{5.6}$$

The uncertainty of the $\sigma_{\text{ext.}}(T_{\text{ext.}})$ associate with the extrapolating the mean flywheel frequency of the maser due to time extension from $T1$ to $T2$ can be written as following,

$$\sigma^2_{\text{ext.}}(T_{\text{ext.}}) = \langle(\delta y_{\text{ext.}})^2\rangle. \tag{5.7}$$

By using Parseval's theorem, we can rewrite Eq. 5.7 in the frequency domain as

$$\sigma^2_{\text{ext.}}(T_{\text{ext.}}) = \int_0^\infty S(f)\,|G(f)|^2\,\mathrm{d}f, \tag{5.8}$$

where $G(f)$ is the Fourier transform of the weighting function, which is written as,

$$G(f) = \int_{-\infty}^{\infty} g(t)\exp(-2\pi\mathrm{i}\,ft)\mathrm{d}t, \tag{5.9}$$

$S(f)$ is the single sided power spectral density of the H-maser frequency fluctuation, which has been estimated by converting the noise contributions of the instability of the H-maser to the spectral power density. The instability for shot term is obtained from the direct comparison between H-maser and Sr lattice clock during the campaign. The instability of mid term is obtained by maser-maser comparisons and for long term instability is obtained from maser-Cs fountain clock compassion. The instability of the H-maser is modeled by assuming three leading noise types. The flicker floor noise is $3\times10^{-16}\cdot\tau^0$ and the white frequency noise is $3.5\times10^{-14}\times\tau^{-1/2}$ [Vor12, Par99] and white phase noise is $1.18\times10^{-13}\times\tau^{-1}$. These noise added in quadrature. The instability of the clocks which were involve in the measurements campaign are present in Figure 5.2. The extension time helps us to reduce the statistical uncertainty of the measurement below systematic uncertainty of the CSF2 ($u_B(\text{CSF2}) = 3.1\times10^{-16}$) and CSF1 ($u_B(\text{CSF1}) = 3\times10^{-16}$), thus this measurement for first time at PTB is not limited be statistical uncertainty. Further more, the uncertainty of the measurement is further reduced by combing the systematic uncertainties of CSF2, CSF1, yielding the Sr clock transition frequency of 429228004229873.04(11) Hz.

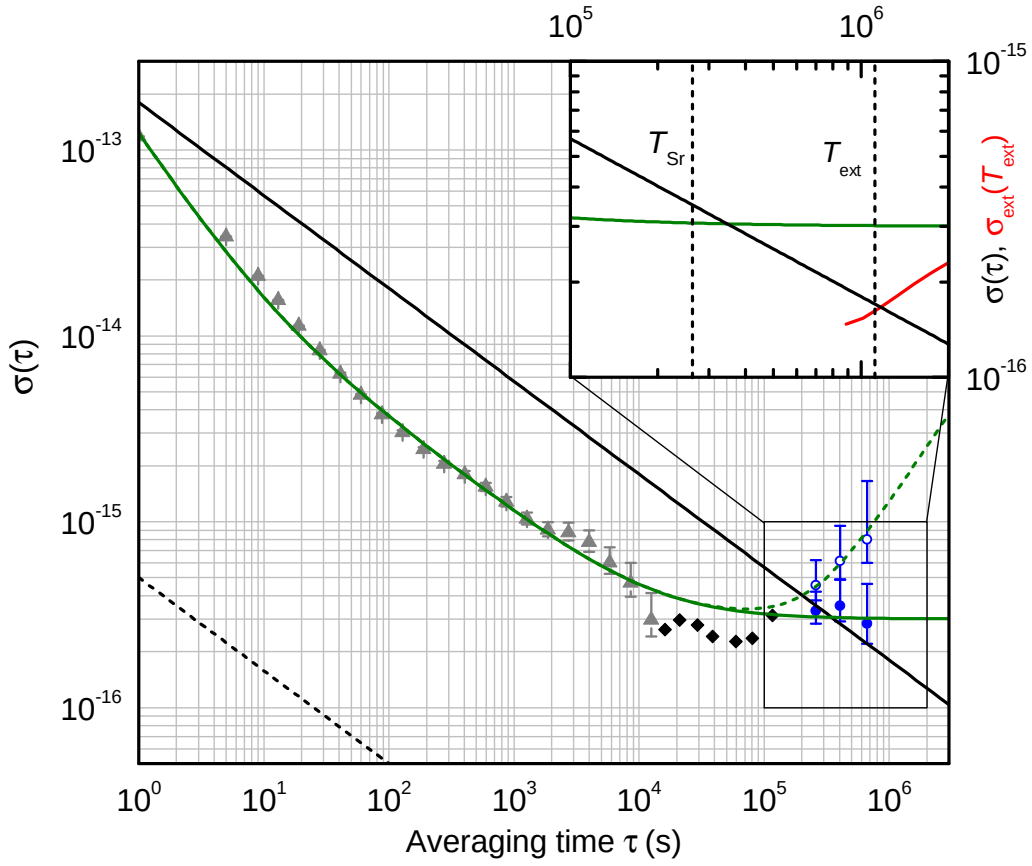

Figure 5.2: The instability of different clocks during the measurements campaign 2014 are presented. The dashed black line is the instability of Sr lattice clock. The solid black line is the instability of fountain clock CSF2. The triangles are the instability maser as inferred from the comparison with the Sr clock. The diamonds are the instability maser. The open circles are the instability maser against fountain clocks. The filled cycles are the same as the open circles but without linear drift. The sold green line reflects the noise model for the H-maser with linear drift removed and dashed green line with linear frequency drift. The insert figure is shown the additional uncertainty (red line) when we used H-maser as a flywheel to extend the time from $T_{\mathrm{Sr}} = 267000$ s to $T_{\mathrm{ext.}} = 10^6$ s. The vertical dashed lines shown the optimum extrapolation measurement times, the extension time is select to be in optimum with reasonable contribution of the $\sigma_{\mathrm{ext.}}(T_{\mathrm{ext.}})$. Adapted from our publication [Gre16].

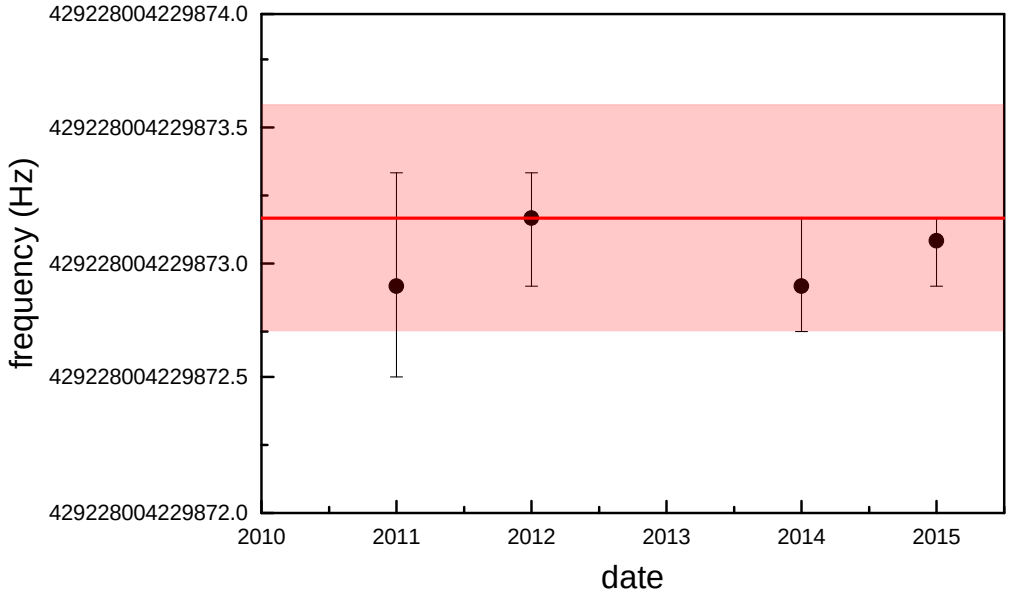

Figure 5.3: Absolute frequency measurements of the ${}^1S_0 - {}^3P_0$ transition in ^{87}Sr atoms are shown. The red solid line is the frequency recommended by the CIPM for the secondary representation of the second based on the ^{87}Sr lattice clocks [CIP15] with assigned uncertainty indicate by the red shade area.

5.1.4 Summary

The absolute frequency measurements of the clock transition based on ${}^1S_0 - {}^3P_0$ transition in ^{87}Sr are measured four times over 5 years. The result is shown in Figure 5.3, the absolute frequency measurements are agreed with frequency recommended by the CIPM for the secondary representation of the second based on the ^{87}Sr optical lattice clocks [CIP15]. The measurements of 2014 and 2015, where H-maser was used as flywheel to bridge gaps in the Sr clock operation, agreed very well with previous measurements which indicate that, the reliability to use a flywheel oscillator (for example H-maser) to extrapolate measurement times is promising.

Figure 5.4 is shown the comparison between our absolute frequency measurements and absolute frequency measurements which is done in somewhere else. There is well good agreement between most of them and frequency recommended by the CIPM for the secondary representation of the second based on the ^{87}Sr lattice clocks [CIP15].

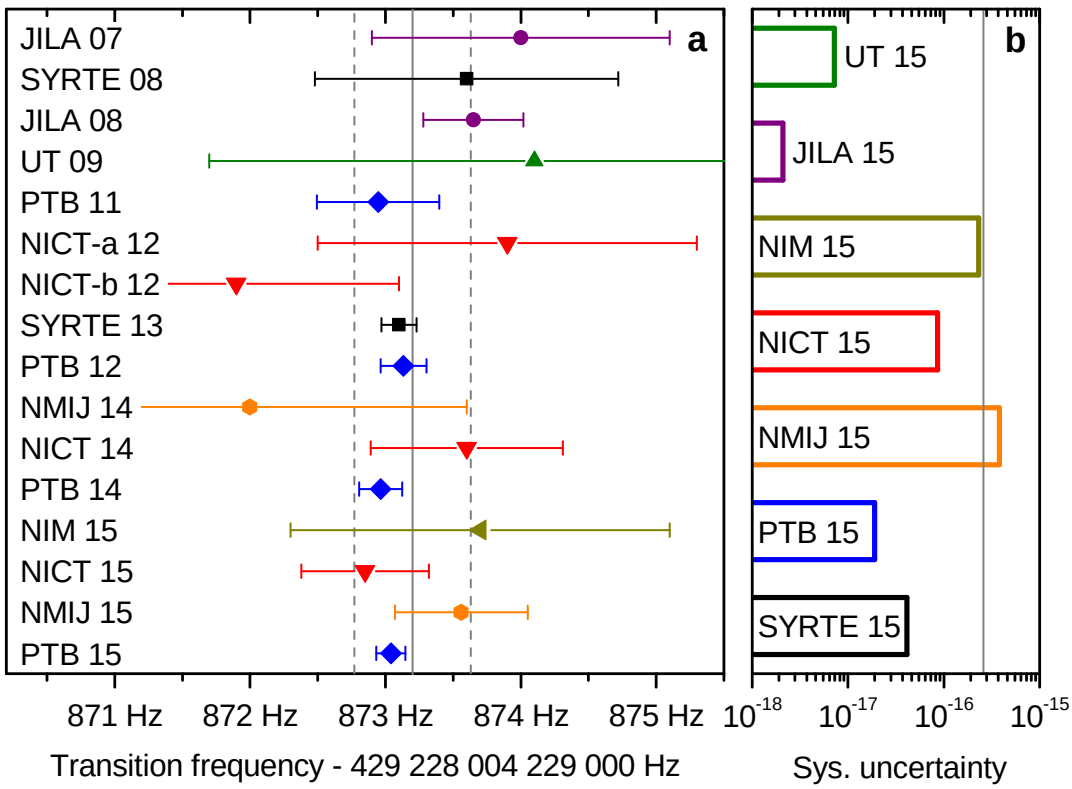

Figure 5.4: Comparison of the absolute frequencies of the ${}^1S_0 - {}^3P_0$ transition is shown. The blue square points are our measurements same as in Figure 5.3. The rest of the points are taken from these publications [Boy07b,Bai08,Cam08,Hon09, Yam12, Mat12, Le 13, Aka14, Hac14, Lin15, Hac15, Tan15]. The gray vertical line is the the frequency recommended by the CIPM for the secondary representation of the second based on the ^{87}Sr lattice clocks [CIP15] with assigned uncertainty indicate by the dash vertical lines.

5.2 Comparison Sr(PTB) against Sr(OP) via fiber link

Over decades satellite-based links [Bau06] have been used for time and frequency transfer worldwide. This technique is cheap, reliable, covers the entire world, and the accuracy and the stability of the link are suitable for microwave clocks. However in the last decade, optical clocks have been shown an accuracy and a stability two orders of magnitude better than the microwave clocks. In order to compared the optical clocks separate by considerable distant (countries scale), an accurate and stable frequency link better than satellite-based link is required. Direct comparison of high accuracy and stability optical clocks is extremely useful for fundamental applications and techniques, e.g., when measuring two similar optical clocks separate by a distance, the general relativistic frequency shift make clocks sensors of the gravitation potential difference [Bje85], which gives us new way to establish, e.g., long-distance height reference frames.

5.2.1 Optical link Braunschweig-Paris

I will mention shortly the optical fiber link between PTB Braunschweig and SYRTE Paris, more details on the fiber link on the Germany side can be found in [Rau14b, Rau14a, Dro15, Rau15]. The France part is discussed in [Ber14, Chi15, Lop15, Ste15]. Figure 5.5 shows the path of the optical link between the national metrology institutes PTB and SYRTE, where two Sr optical lattice clocks are compared directly. The German link consists of a pair of the telecommunication fiber from Braunschweig to Strasbourg (at Université de Strasbourg) with a distance of 710 km. The link have three of the narrow band fiber Brillouin amplifiers to recovered the signal which is attenuated during the transmission over fiber lengths of hundreds of km (the attenuation of the signal in the silica telecommunication for 1550 nm is about 0.2 dB/km). The transfer frequency of 194.4 THz (1550 nm) is produced from a laser which is locked to a cavity. The optical link is phase stabilized by using a Michelson interferometer [Rau14b, Pre12]. The France link consists of the two parallel fiber links (the fiber from the France academic network) from Paris to Strasbourg (705 km), repeater laser stations (RLSs) and broad-band amplifiers. The transfer frequency and phase stabilization are similar as on the Germany link.

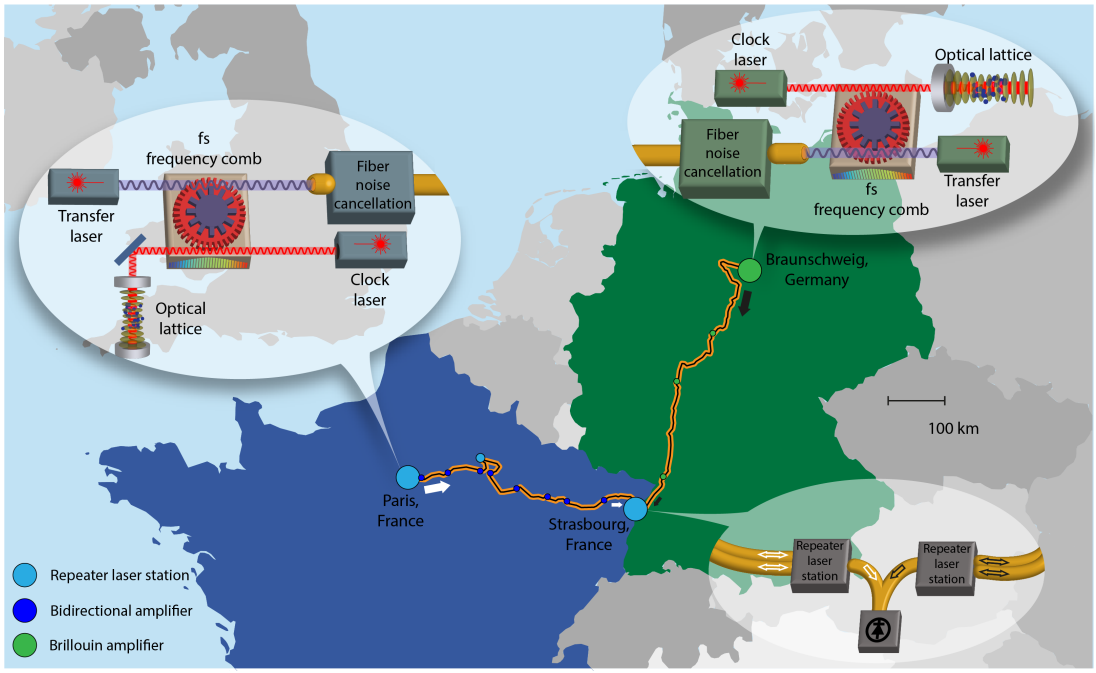

Figure 5.5: Schematic of the two ways fiber link between PTB Braunschweig and SYRTE Paris. On the Germany side there are three amplification stations (highlighted by green points). In France side there are eight amplification stations (highlighted by blue points). The simplified setups which are involve in campaign for both institutes are show in the insets. The beat transfer between PTB-SYRTE is measured in Strasbourg. Adapted from our publication [Lis16].

5.2.2 March and June 2015 measurements

After the optical link between PTB and SYRTE has been build and characterized by my colleagues from PTB and SYRTE, two direct comparisons have been performed between the Sr lattice clocks at both sides [2]. During the measurements, both Sr lattice clocks are running at the same time, with a systematic uncertainty of 1.9×10^{-17} for $\mathrm{Sr}_{\mathrm{PTB}}$ and 4×10^{-17} for $\mathrm{Sr}_{\mathrm{SYRTE}}$ with instability of $5 \times 10^{-16}/\sqrt{\tau}$ for $\mathrm{Sr}_{\mathrm{PTB}}$ and about $1 \times 10^{-15}/\sqrt{\tau}$ for $\mathrm{Sr}_{\mathrm{SYRTE}}$. The frequency ratio of the Sr lattice clocks is measured as following:

- The frequency ratio between the Sr lattice clock and transfer laser is determined locally by frequency comb.
- Light from the laser frequency at 194.4 THz (1542 nm) is sent from PTB and SYRTE to the Strasbourg.
- At Strasbourg the beat note between the two transfer lasers is measured.
- The frequency ratio of $\mathrm{Sr}_{\mathrm{PTB}}/\mathrm{Sr}_{\mathrm{SYRTE}}$ is determined by combining the frequency ratios from Braunschweig, Strasbourg and Paris as following

$$\frac{\nu_{\mathrm{Sr}}^{\mathrm{PTB}}}{\nu_{\mathrm{Sr}}^{\mathrm{SYRTE}}} - 1 \approx \left(\frac{\delta\nu}{\nu_0}\right)_{\mathrm{Sr}}^{\mathrm{PTB}} - \left(\frac{\delta\nu}{\nu_0}\right)_{\mathrm{Sr}}^{\mathrm{SYRTE}}, \tag{5.10}$$

  where $\delta\nu = \nu(t) - \nu_0$, $\nu(t)$ is the frequency measured at time t and ν_0 is the nominal frequency. The combing frequency ratio can be written as,

$$= \underbrace{\left(\frac{\delta\nu}{\nu}\right)_{\mathrm{Sr}}^{\mathrm{PTB}} - \left(\frac{\delta\nu}{\nu}\right)_{\mathrm{Trans}}^{\mathrm{PTB}}}_{\text{Braunschweig}} + \underbrace{\left(\frac{\delta\nu}{\nu}\right)_{\mathrm{Trans}}^{\mathrm{PTB}} - \left(\frac{\delta\nu}{\nu}\right)_{\mathrm{Trans}}^{\mathrm{SYRTE}}}_{\text{Strasbourg}} + \underbrace{\left(\frac{\delta\nu}{\nu}\right)_{\mathrm{Trans}}^{\mathrm{SYRTE}} - \left(\frac{\delta\nu}{\nu}\right)_{\mathrm{Sr}}^{\mathrm{SYRTE}}}_{\text{Paris}} \tag{5.11}$$

Figure 5.6 shows the averaged deviation of the $\frac{\nu_{\mathrm{Sr}}^{\mathrm{PTB}}}{\nu_{\mathrm{Sr}}^{\mathrm{SYRTE}}} - 1$ for measurements in March and June 2015 (145 hours accumulated data). The March measurements are divided to length of 6000 s and June measurements to length of 125000 s for determining the statistical

[2] These comparisons are joint measurement campaigns between PTB (our Sr lattice clock group, fiber link group and frequency comb group) and SYRTE (Sr lattice clock group, fiber link group and frequency comb group). All names of my colleagues who participated in these campaigns from both sides are listed in [Lis16].

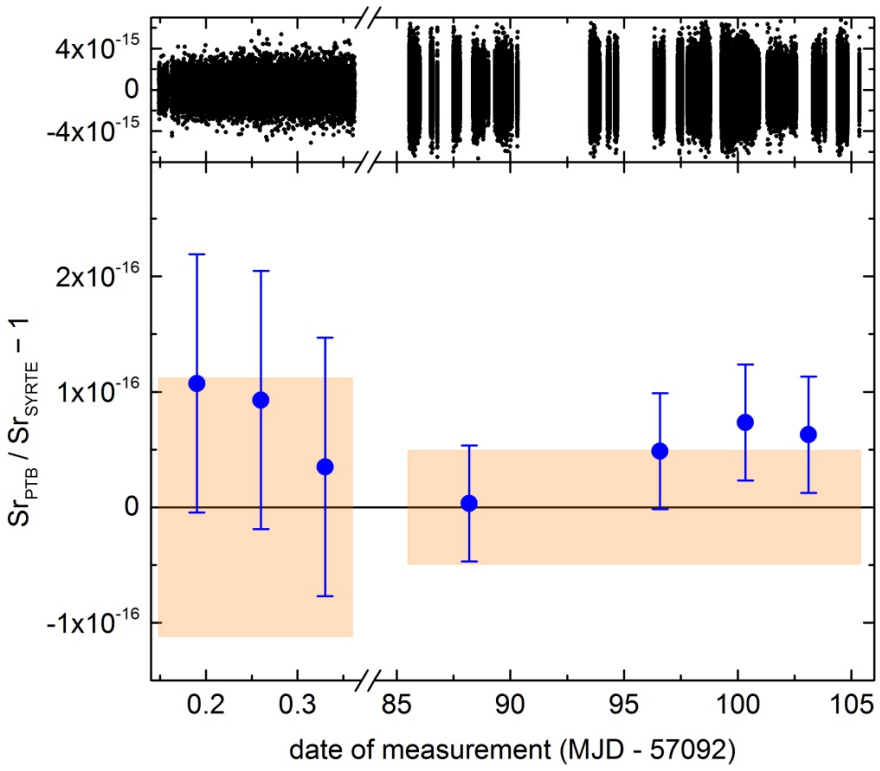

Figure 5.6: The frequency ratio $\mathrm{Sr}_{\mathrm{PTB}}$ against $\mathrm{Sr}_{\mathrm{SYRTE}}$. TOP: Raw data of the measurement campaigns. BOTTON: March measurements have been averaged to length of 6000 s and 125000 s for June measurements. The total uncertainty (systematic and statistical) is shown, the systematic uncertainty is dominating. The shaded area represents a $\pm\sigma$ interval uncertainty around the expectation value (zero). Adapted from our publication [Lis16].

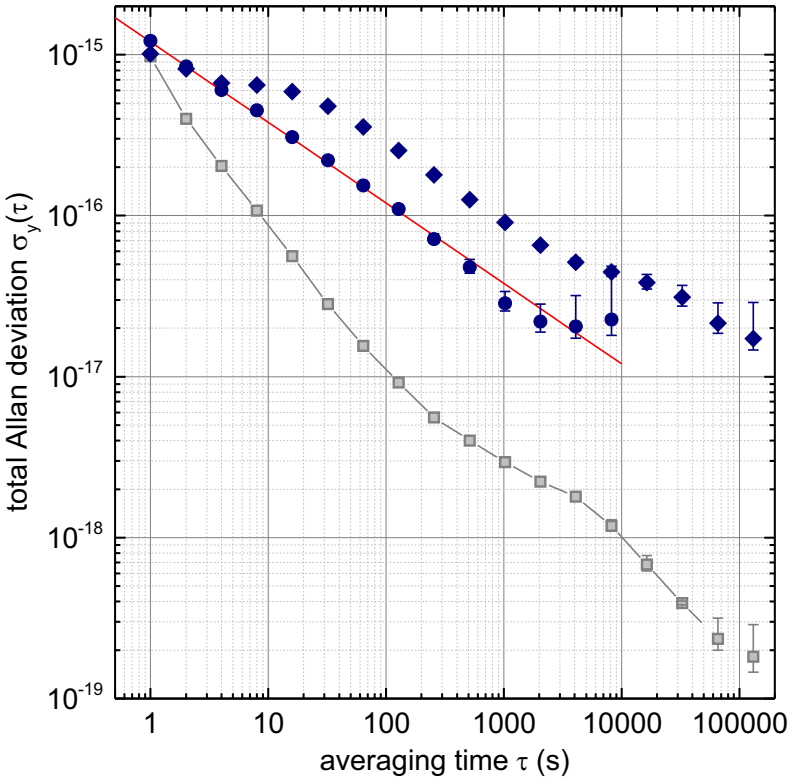

Figure 5.7: Instability of the clock comparison (Sr_{PTB} against Sr_{SYRTE}) as function of the averaging time τ. The blue circles show the instability for March measurements averaging down with $1 \times 10^{-15}/\sqrt{\tau}$. The blue squares are the instability for June measurements averaging down with $3 \times 10^{-15}/\sqrt{\tau}$. The gray squares are the link instability. Adapted from our publication [Lis16].

uncertainty of the measurements. Both measurements show very good clock agreement, after the systematic frequency shifts for both Sr clocks and the synchronization offsets of the counters are corrected. The gravitation redshift has be corrected and I will give some details on how we determined the gravitation redshift in next subsection. The fractional offset frequency between the Sr lattice clocks is 4.7×10^{-17} with uncertainty of $\pm 5 \times 10^{-17}$ last measurement (as seen in Table 5.1). During the first measurement campaign, the frequency counters have larger uncertainty because the counters in Strasbourg and Paris were not synchronized with the local realization of the Coordinated Universal Time (UTC) and the transfer laser was drifting by 2 Hz s^{-1}, the synchronization between them was derived indirectly as written in [Rau14a] and the frequency offset was derived with 1×10^{-16} uncertainty. During the second measurement campaign, the counters were synchronized and the drift of the transfer laser was below 50 mHz s^{-1}, thus the uncertainty of the counter synchronization has negligible contribution to the uncertainty of the second campaign. Figure 5.7 shows the instability of the measurement campaigns. The instability shows for long averaging time a white frequency noise behavior that falls off with the square root of the averaging time. The March measurements show an instability of $1 \times 10^{-15}/\sqrt{\tau}$, and $3 \times 10^{-15}/\sqrt{\tau}$ for June measurements (the different instability is due to some changing in the experimental parameters). The instability of the link has negligible contribution for the measurements, within 2000 s the link instability reaches 2×10^{-17} statistical uncertainty. This level of precision and accuracy of a remote frequency comparison is for first time achieve worldwide. This measurement is one order of magnitude better than any possible comparison done against primary cesium clocks. Direct comparison optical-optical clocks with this precision is an important step for the redefinition the SI-second based on an optical clock and also open new area of research capabilities.

Gravitation redshift

A clock in a gravitational potential U is running slower by a factor of $1 + U/c^2$, where c is the speed of light, compare to a clock with zero gravitational potential. This effect is well know as the gravitational redshift [Ein11]. This effect had to be taken into account during the measurement campaigns the Sr lattice clock at PTB is higher by 25 m from the Sr

Ratio $\frac{\mathrm{Sr_{PTB}}}{\mathrm{Sr_{SYRTE}}}$	March 2015 Campaign 10^{-17}	June 2015 Campaign 10^{-17}
Systematics $\mathrm{Sr_{SYRTE}}$	4.1	4.1
Systematics $\mathrm{Sr_{PTB}}$	2.1	1.9
Statistical uncertainty	2	2
fs combs	0.1	0.1
Link uncertainty	<0.1	0.03
Counter synchronization	10	< 0.01
Gravity potential correction	0.4	0.4
Total	11.2	5.0

Table 5.1: The table shows the total uncertainty of the frequency ratio $\frac{\mathrm{Sr_{PTB}}}{\mathrm{Sr_{SYRTE}}}$. Adapted from our publication [Lis16].

lattice clock at SYRTE, thus the frequency difference between them due to gravitational potential difference is,

$$\mathrm{Sr_{SYRTE}} = \mathrm{Sr_{PTB}} - \frac{\Delta U}{\mathrm{c}^2}, \tag{5.12}$$

where ΔU is the gravitational potential difference between Sr lattice clocks at PTB and SYRTE. In order to correct the redshift the the gravitational potential difference has to be calculated. There are two methods to determine the gravitational potential difference. First by so called the geometric leveling technique which is accurate and easy to realize on short distances, the accuracy of this technique within 1 mm for short distances and the accuracy decrease with longer distance (a few 1000 km).

The second method is based on the Global Navigation Satellite System (GNSS) and the gravity modeling (geoid). This method requires precise GNSS positions and gravity field modeling results for the points of the interest. The gravitational potential difference between Sr lattice clocks at PTB and SYRTE by combining the two methods. For the PTB side, the GNSS/geoid method gives us the potential at a marker in the Sr laboratory which is 763.75 $\mathrm{m^2/s^2}$ from marker to the atom position we used the geometric leveling method. The height difference between the marker and Sr atoms is 0.542 ($\pm$4) m, thus the gravitational potential at Sr atoms is derived. In a similar way the gravitational potential at SYRTE has been determined. The gravitational potential difference between Sr atoms at PTB and SYRTE is 224.14 $\mathrm{m^2/s^2}$, which causes a frequency shift between them of 1.06 Hz or fractional shift of 2.472×10^{-15} with an uncertainty of 4×10^{-17}.

5.3 Search for variation of α

Some of cosmological models suggest that the fundamental constants may vary over time since the early Universe [Uza03, Kar04]. Thus it is important to check whether fundamental constants vary or not, thus better understanding low-energy world. There are many fundamental constants, like the fine structure constant α, the electron-proton mass ratio $\frac{m_e}{m_p}$, etc. I will focus on placing limits on possible variation of α, which is characterize the strength of the electromagnetic interaction (which describes the interaction between electrons and photons) $\alpha = e^2/\hbar c$. It is also important to see if a variation of the fine structure constant over time exists. There are three methods which can used to put a limits on the variation of the fine structure constant α; quasar spectra, the Oklo uranium mine, and atomic clocks. More details on the first two methods can be found in [Web01, Web11, Sri04, Shl76, Dam96] and I will put more details on the third method, which we used to search for a possible variation of α.

5.3.1 Atomic clock

An interesting applications of atomic clocks are to test the fundamental constants. This method much better than first two methods for determining the variation of α due to high precision, low systematic uncertainty, and it is easier to control systematic errors. By optical clocks we can probe the temporal variation of α, which make the result easier to interpret compared to the first two methods (where both temporal and spatial variation of α are involve). The measurement is done by measuring the ratio between two optical clocks and the measurement has to be repeated after some time. Optical clocks are a very good choice to search for variations of α because the frequency ratio between two optical clocks are depend only on α. In contrast, hyperfine transitions depend on α and $\frac{m_e}{m_p}$. The electronic transition frequency can be written as following,

$$f = R_y.C.F(\alpha), \tag{5.13}$$

where $R_y = \frac{m_e e^2}{8\epsilon^2 h^3}$ is the Rydberg constant in frequency units. C is a constant depending on the atomic state properties, which are assumed to be constant with time. $F(\alpha)$ is a dimensionless function of α, which takes into account the relativistic contributions to the

energy level of the atomic states. The relative temporal variation of the frequency f can be written as [Pei04],

$$\frac{\delta \ln f}{\delta t} = \frac{\delta \ln R_y}{\delta t} + A\frac{\delta \ln \alpha}{\delta t} \tag{5.14}$$

where $\frac{\delta \ln R_y}{\delta t}$ is a variation which is common for all electronic transition frequencies. The last term is relate to the variation of α over time which is under investigation. The sensitivity factor A for this variation is calculated for relevant transitions by relativistic Hartree-Fock calculations [Dzu99, Dzu09]. Now, it is important to choose two optical clocks with different sensitivity factor A, ideally with large difference. In our case we have used two very different optical clocks, one based on the $^1S_0 - {}^3P_0$ transition of many ^{87}Sr atoms confined in an optical lattice. The sensitivity factor of this transition is very small $A = 0.062$ [Fla09] while for the other clock based on the $^2S_{1/2} - {}^2F_{7/2}$ electric octupole (E3) transition of the single $^{171}Yb^+$ [Hun12b, Hun16] the sensitivity factor $A = -6$ is comparatively large. The frequency ratio [3] between them has been measured in 2010, 2012 and 2015. The instability of the 2015 measurement is shown in Figure 5.8. The instability of the ratio measurement is $4.4 \times 10^{-15}/\sqrt{\tau}$ limited by the single $^{171}Yb^+$ ion due to clock's quantum projection noise limit. More than 80 hours of data are recorded during the measurement in 2015, which reduced the statistical uncertainty to 1.3×10^{-17}. The frequency ratio of the two clocks is determined with total uncertainty of (2.2×10^{-17}). The frequency ratio is determined to be,

$$\frac{^{171}\mathrm{Yb}^+}{^{87}\mathrm{Sr}} = 1.495991618544900642(36). \tag{5.15}$$

This frequency ratio has been measured also in 2012 and in 2010. These measurements are used to check if the frequency ratio and thus the fine structure constant is constant over time. Figure 5.9 shows how much the frequency ratio has been varied due to the variation of the fine structure constant over time. Taking into account the sensitivity of the clocks to α [Fla09] and the time between the measurements we have derived the most stringent limit on a potential linear drift of the fine structure constant α over time to be $-0.67(47) \times 10^{-17}$ per year. Table 5.2 shows the frequency ratio measurements for

[3] These measurements are joint measurements between Quantum Optics and Unit of Length department 4.3 (our Sr lattice clock group and frequency comb group) and Time and Frequency department 4.4 (Yb^+ ion clock group and frequency comb group).

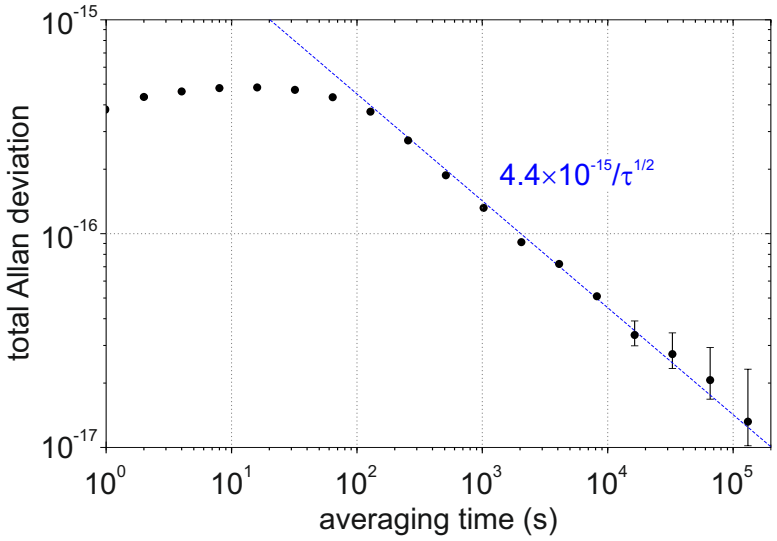

Figure 5.8: The instability of the frequency ratio of the optical clocks as function of averaging time for the 2015 measurement. The dashed line shows an instability of $4.4 \times 10^{-15}/\sqrt{\tau}$.

Probe clock	Reference clock	$\frac{1}{\alpha}\frac{\delta\alpha}{\delta t}$	Reference
$^{171}Yb^{+}$	$^{199}Hg^{+a}$	$-22.0 \pm 39 \times 10^{-17}$	[Pei06]
^{87}Rb	^{133}Cs	$-4.00 \pm 16 \times 10^{-17}$	[Mar03]
H	$^{199}Hg^{+a}$	$-90 \pm 290 \times 10^{-17}$	[Fis04]
$^{27}Al^{+}$	$^{199}Hg^{+}$	$-1.60 \pm 2.3 \times 10^{-17}$	[Ros08]
$^{171}Yb^{+}$	^{133}Cs	$-2.00 \pm 2.0 \times 10^{-17}$	[Hun14]
$^{171}Yb^{+}$	^{87}Sr	$-0.67 \pm 0.47 \times 10^{-17}$	This work

Table 5.2: Table of the limits on the temporal variation of the fine structure constant α by using the atomic clocks.

different kind of the clocks to check if the fine structure constant α is constant or not.

In the future, more frequency ratio measurements with high precision and accuracy (on the level of 10^{-18}) are an important to put new stringent limit on a potential linear drift of the fine structure constant α over time.

5.4 Summary

During this chapter, several high-accuracy measurements have been performed with our clock. The absolute frequency of the clock transition was measured to be 429 228 004

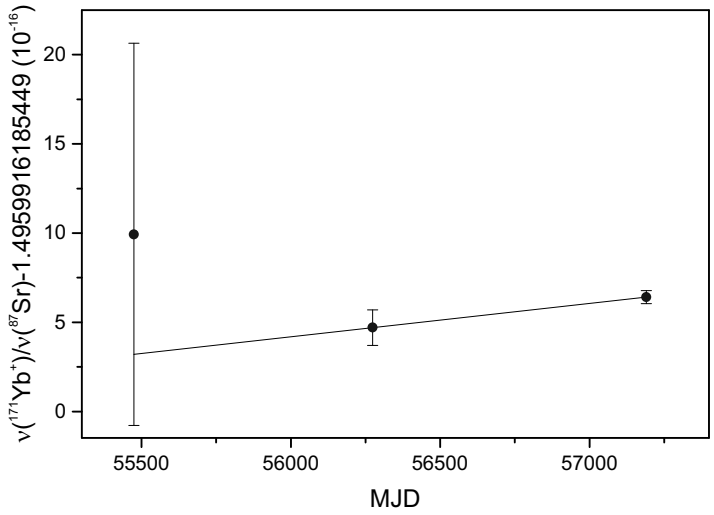

Figure 5.9: The frequency ratio of the $\frac{^{171}\mathrm{Yb}^{+}}{^{87}\mathrm{Sr}}$ is plotted as function of the time. The solid line is the linear fit and the significant deviation of the slope from zero is indicate a nonzero frequency drift rate due to fine structure constant. MJD: Modified Julian Date.

229 873.04 (11) Hz [Gre16], with significant improvement of the uncertainty of the measurements due to longer measurements and using H-Maser as flywheel to cover gaps in the operation of the Sr clock, and the uncertainty of the measurements is further reduced by combing the systematic uncertainties of CSF2, CSF1. The absolute frequency measurements are agreed with frequency recommended by the CIPM for the secondary representation of the second based on the ^{87}Sr optical lattice clocks [CIP15] and with measurements performed in different laboratories.

Comparisons between the Sr clocks at PTB (Braunschweig) and SYRTE (Paris) via a fiber link [Rau15,Lop15] have been performed, and the fractional offset frequency between them has been measured to be $(4.7 \pm 5.0) \times 10^{-17}$ [Lis16]. Such comparisons over large distances are an important step towards a redefinition of the SI second based on an optical transition.

Optical frequency ratio measurements between our clock and a single $^{171}\mathrm{Yb}^{+}$ ion clock [Hun16] at PTB have been carried out in 2010, 2012, and 2015. These measurements are used to check if the frequency ratio and thus the fine structure constant is constant over time. From these measurements, we have derived the most stringent limit on a

potential linear drift of α over time to be -0.67×10^{-17} per year with an uncertainty of $\pm 0.47 \times 10^{-17}$.

Chapter 6

Summary and Outlook

6.1 Summary

During this work, the uncertainty of the blackbody radiation (BBR) shift has been reduced by more than order of magnitude (from 1.2×10^{-17} to less 1×10^{-18}, in fractional unit), thus making, the uncertainty of BBR shift has negligible contribution to the uncertainty of the clock. This reduction in the uncertainty was possible by modifying the vacuum chamber, by instilling the cold finger (see 3.4) 22 mm away from the MOT position, which allows us to interrogate atoms inside a well controlled environment at cryogenic temperature. Thus, the BBR shift is reduced (according to (Eq.3.8)) and its uncertainty as well. The total systematic uncertainty of the clock has been evaluated (see Table 3.4) to be 1.3×10^{-17} at cryogenic temperature.

For the instability of the clock, the detection noise of the clock is measured and a model linking noise and clock instability has been developed. The noise model is showing that in our lattice clock the quantum projection noise is reached if more than 130 atoms are interrogated. By using the noise model together with the degradation due to the Dick effect reflecting the frequency noise of the interrogation laser, the instability of the clock is estimated to be $1.6 \times 10^{-16}/\sqrt{\tau/\mathrm{s}}$ [Al-15] which is the lowest instability is published so far.

During this work, several measurements have been preformed with the clock:

- The absolute frequency of the clock transition ha been measured several times. The Sr clock transition frequency is measured to be 429 228 004 229 873.04 (11) Hz [Gre16], with significantly improvement of the uncertainty of the measurements due to longer measurements and using H-Maser as flywheel to cover any gap in the operation of the Sr clocks, and by combing the systematic uncertainties of SCF2, and SCF1. These measurements have excellent agreement with measurements performed in different laboratories.

- Ratio measurements between our clock and single $^{171}Yb^{+}$ ion clock both at PTB have be performed, These measurements are used to check if the frequency ratio and thus the fine structure constant is constant α over time. From these measurement the most stringent limit on a potential linear drift of α over time to be -0.67×10^{-17} per year with uncertainty of $\pm 0.47 \times 10^{-17}$ (not published yet).

- Further more, Comparisons between the Sr clock PTB against the Sr clock SYRTE via fiber link was performed with a fraction offset between them of $(4.7 \pm 5.0) \times 10^{-17}$ [Lis16]. Such kind of comparison of two dully independent optical clocks with longer distance was a first and an important step for redefinition of the SI second based on optical transition.

6.2 Outlook

In our experiment, we have evaluated the final uncertainty budget of the clock to be 1.3×10^{-17} at cryogenic temperature. It is limited by the uncertainty due to magic wavelength of the lattice laser (see table 3.4) as the lattice trap is nearly horizontal, thus deep lattice depth is required to hold atoms against gravity and to suppress the tunneling, resulting in a large uncertainty of the AC stark shift of the lattice laser. We decided to upgraded the vacuum chamber. The new design is shown in Figure 6.1, which is designed by our post-doc Sören Dörscher. The following issues has been take into account with new design;

- The lattice trap going to be vertical, thus relaxing the problems with tunneling, which allows us to operate the clock with shallow lattice depth to reduce the uncertainty due to AC Stark shift.

- Possibility to operate the clock at any temperatures between 77 K to 300 K.
- Atoms will be interrogated in the MOT position, thus no transport of the atoms is required as in the coldfinger, resulting in a better duty cycles, thus better stability and high reliability.
- Better vacuum pressure, which is an important issue for longer lattice lifetime which is going to be an requirement for longer interrogation times (more than 1 s interrogation time).
- Lasers used for cooling and trapping are going to be compact and reliable. This is aiming to increase uptime of the clock.

Figure 6.2 shows a cross section of the new chamber. The internal chamber made of a copper for providing homogenous temperature surrounding the atomic sample due to high thermal conductivity. The block of copper has dimension of 110.5 mm $\times$ 100.5 mm $\times$ 52.5 mm (length, width, and depth). The chamber has accesses for all beams for MOT, lattice trap, interrogation, and detection. Incoming BBR from the outer vacuum chamber is blocked by a two BK7 windows with a thickness of 5 mm each to suppress blackbody radation shift to level below than 1×10^{-18} in fractional unit. The copper is connected to a cryocooler (which is omitted in Figure 6.2) to cool the inner chamber to any temperature between 77 K and 300 K. The chamber has additional access for a build-up lattice cavity (nearly horizontal), which is going to be used for developing highly controlled quantum state engineering by squeezing and entanglement. Moreover, the atomic oven and Zeeman slower access are blocked by mechanical rotation shutters during the interrogation, which can be cooled down to cryogenic temperature to avoid additional BBR shift from the oven and from the Zeeman slower port. All parts of the new chamber are ordered and we expect to assemble them at the end of this year/ beginning of the next year. We are looking forwards to characterize the clock with level of 1×10^{-18} in fractional units.

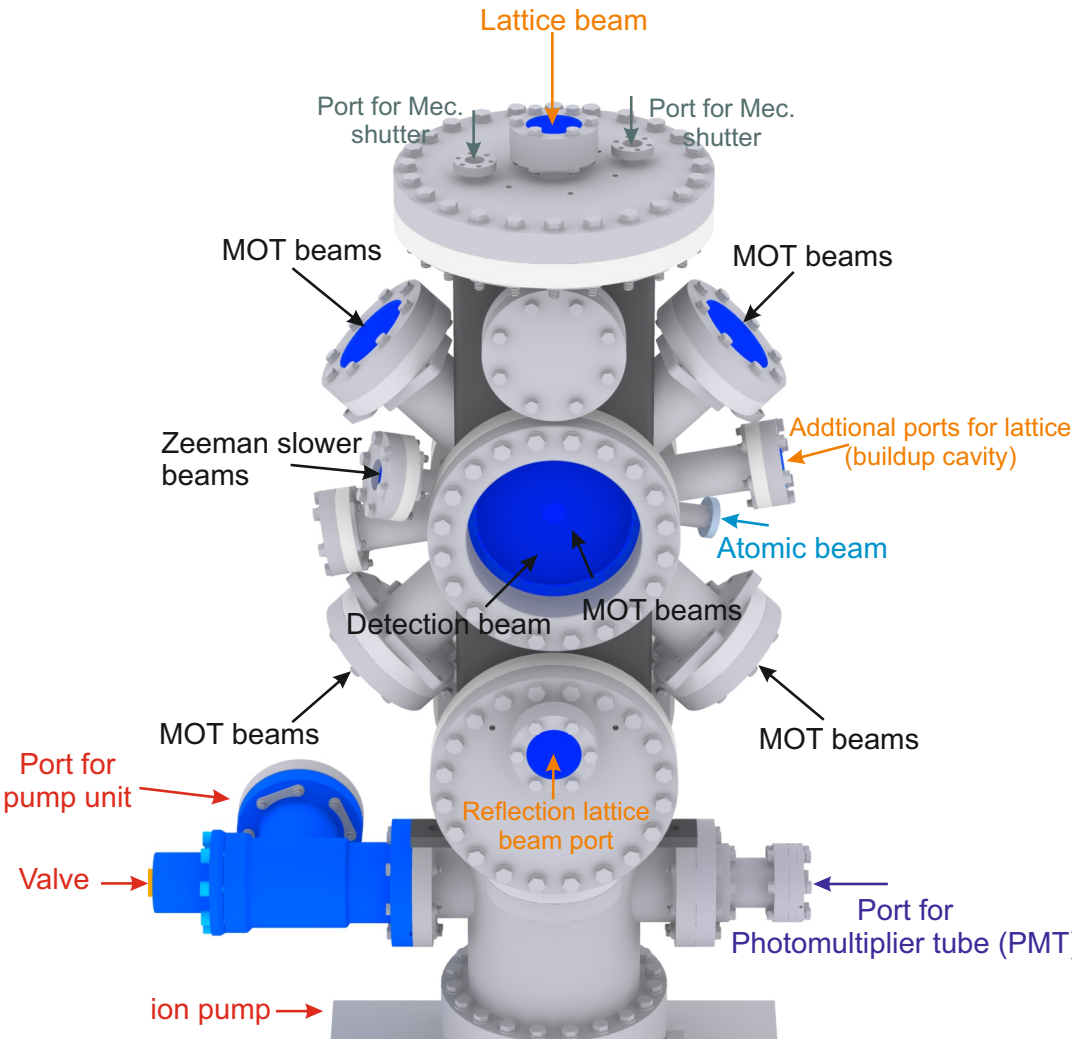

Figure 6.1: Overview of the new vacuum chamber (from CAD).

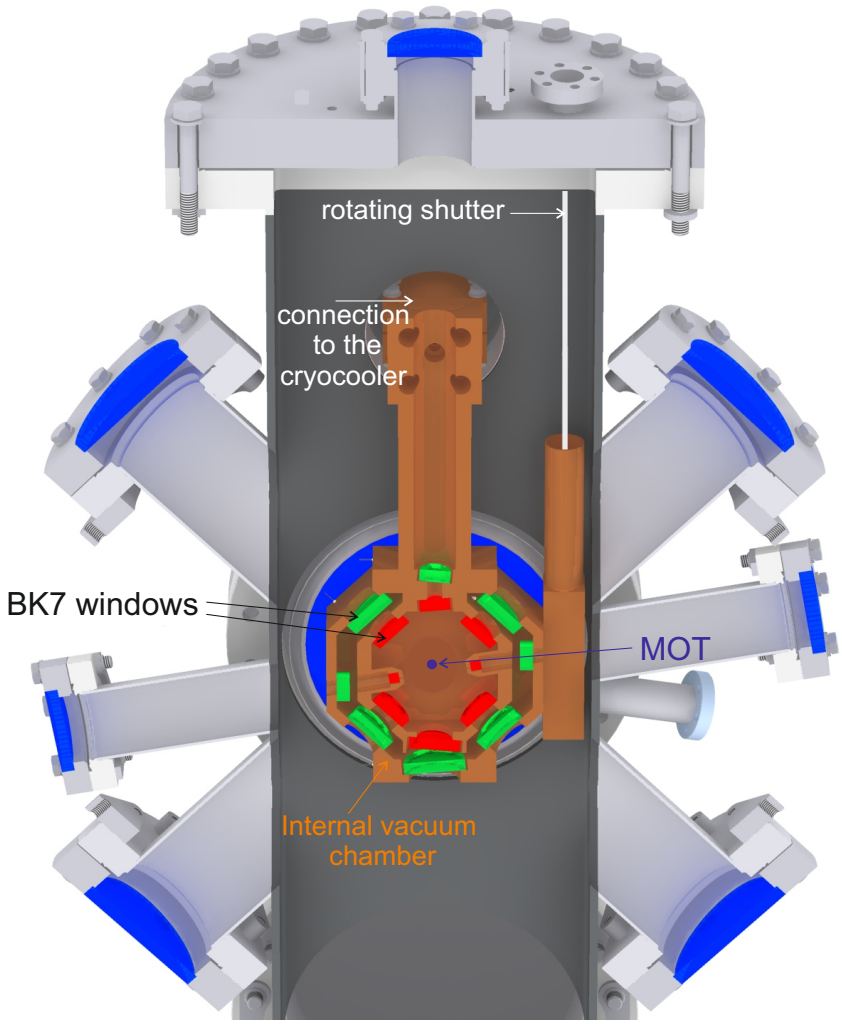

Figure 6.2: A cross section of the chamber (CAD). The internal chamber made of a copper with a dual-layer for homogeneous thermal environment. BK7 windows are indicated by green and red. The cryocooler is connected to the internal chamber from the back.

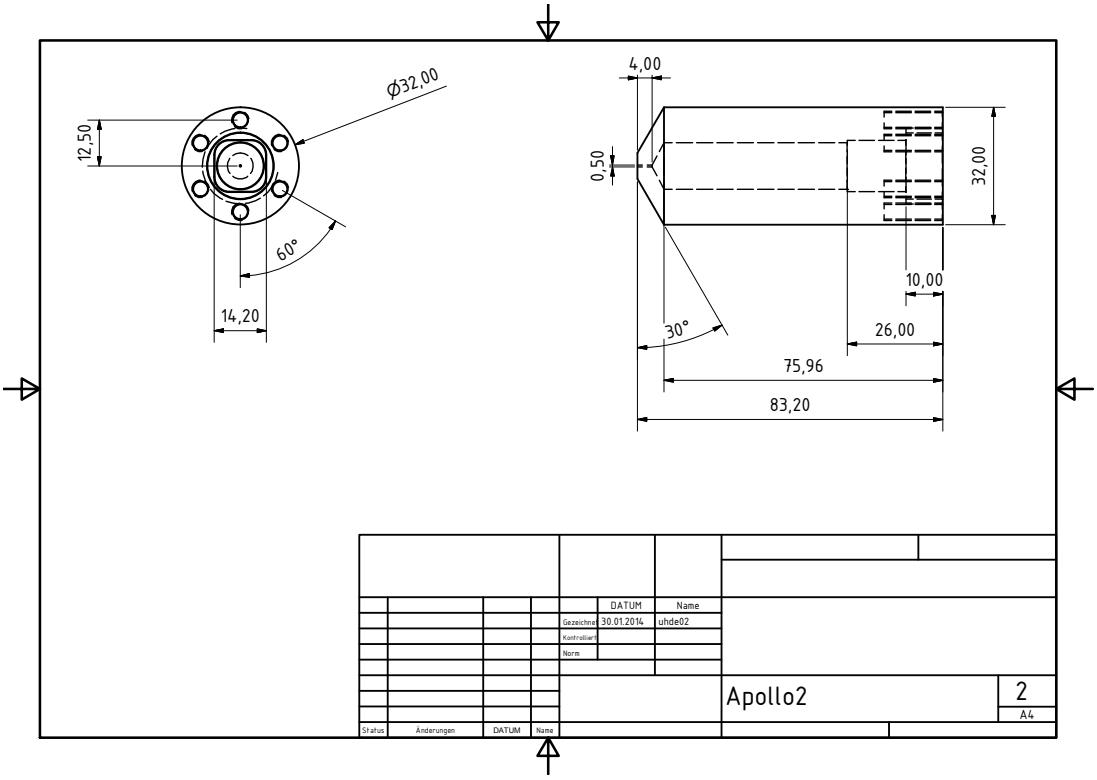

Figure 6.3: Cold finger design with the lengths.

Appendix

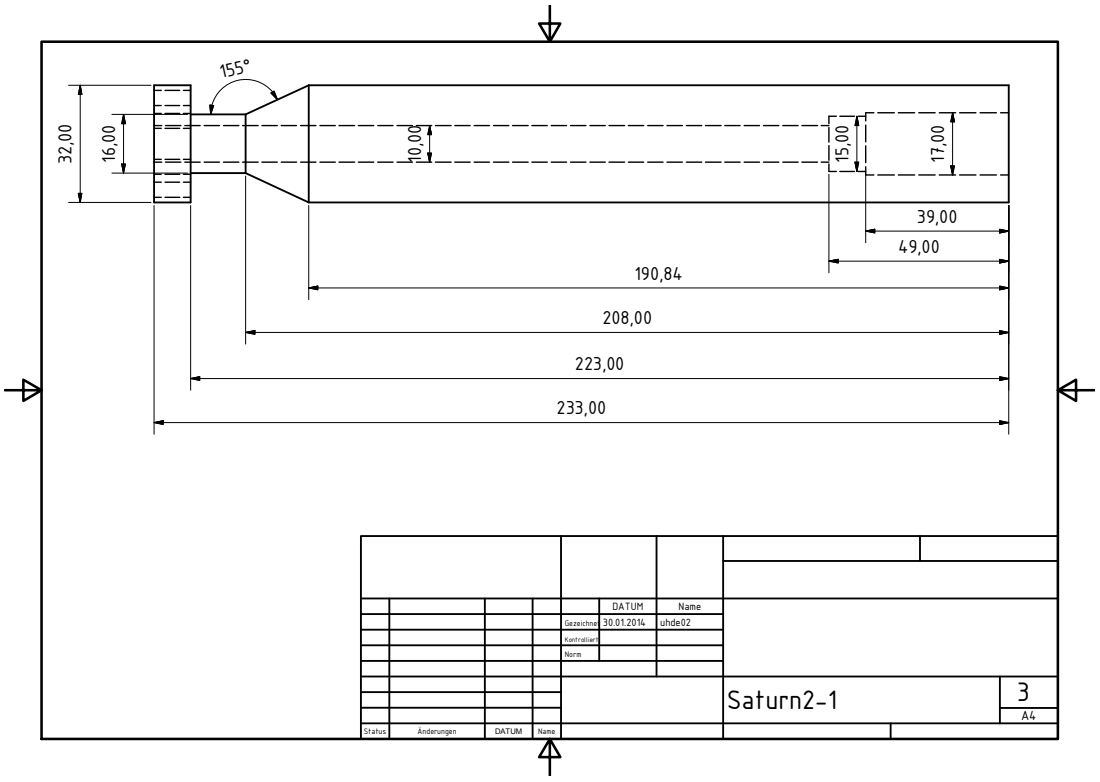

Figure 6.4: Extended the cold finger.

Bibliography

[Aka14] Daisuke Akamatsu, Hajime Inaba, Kazumoto Hosaka, Masami Yasuda, Atsushi Onae, Tomonari Suzuyama, Masaki Amemiya and Feng-Lei Hong, "Spectroscopy and frequency measurement of the ^{87}Sr clock transition by laser linewidth transfer using an optical frequency comb", Appl. Phys. Express **7**, 012401 (2014).

[Al-15] Ali Al-Masoudi, Sören Dörscher, Sebastian Häfner, Uwe Sterr and Christian Lisdat, "Noise and instability of an optical lattice clock", Phys. Rev. A **92**, 063814 (2015).

[Arv15] Asimina Arvanitaki, Junwu Huang and Ken Van Tilburg, "Searching for dilaton dark matter with atomic clocks", Phys. Rev. D **91**, 015015 (2015).

[Bai08] X. Baillard, M. Fouché, R. Le Targat, P. G. Westergaard, A. Lecallier, F. Chapelet, M. Abgrall, G. D. Rovera, P. Laurent, P. Rosenbusch, S. Bize, G. Santarelli, A. Clairon, P. Lemonde, G. Grosche, B. Lipphardt and H. Schnatz, "An optical lattice clock with spin-polarized ^{87}Sr atoms", Eur. Phys. J. D **48**, 11 (2008).

[Bau06] A. Bauch, J. Achkar, S. Bize, D. Calonico, R. Dach, R. Hlavać, L. Lorini, T. Parker, G. Petit, D. Piester, K. Szymaniec and P. Uhrich, "Comparison between frequency standards in Europe and the USA at the 10^{-15} uncertainty level", Metrologia **43**, 109 (2006).

[Bau12] A. Bauch, S. Weyers, D. Piester, E. Staliuniene and W. Yang, "Generation of UTC(PTB) as a fountain-clock based time scale", Metrologia **49**, 180 (2012).

[Bel14] K. Beloy, N. Hinkley, N. B. Phillips, J. A. Sherman, M. Schioppo, J. Lehman, A. Feldman, L. M. Hanssen, C. W. Oates and A. D. Ludlow, "An atomic clock with 1×10^{-18} room-temperature blackbody Stark uncertainty", Phys. Rev. Lett. **113**, 260801 (2014).

[Ber14] Anthony Bercy, Fabio Stefani, Olivier Lopez, Christian Chardonnet, Paul-Eric Pottie and Anne Amy-Klein, "Two-way optical frequency comparisons at 5×10^{-21} relative stability over 100-km telecommunication network fibers", Phys. Rev. A **90**, 061802 (2014).

[Bje85] Arne Bjerhammar, "On a relativistic geodesy", Bulletin Géodésique **59**, 207 (1985).

[Bla09] S. Blatt, J. W. Thomsen, G. K. Campbell, A. D. Ludlow, M. D. Swallows, M. J. Martin, M. M. Boyd and J. Ye, "Rabi spectroscopy and excitation inhomogeneity in a one-dimensional optical lattice clock", Phys. Rev. A **80**, 052703 (2009).

[Bor05] Christian J. Bordé, "Base units of the SI, fundamental constants and modern quantum physics", Phil. Trans. R. Soc. A **363**, 2177 (2005).

[Boy07a] Martin M. Boyd, *High Precision Spectroscopy of Strontium in an Optical Lattice: Towards a New Standard for Frequency and Time*, PhD thesis Graduate School of the University of Colorado 2007.

[Boy07b] Martin M. Boyd, Andrew D. Ludlow, Sebastian Blatt, Seth M. Foreman, Tetsuya Ido, Tanya Zelevinsky and Jun Ye, "^{87}Sr lattice clock with inaccuracy below 10^{-15}", Phys. Rev. Lett. **98**, 083002 (2007).

[Boy07c] Martin M. Boyd, Tanya Zelevinsky, Andrew D. Ludlow, Sebastian Blatt, Thomas Zanon-Willette, Seth M. Foreman and Jun Ye, "Nuclear Spin Effects in Optical Lattice Clocks", Phys. Rev. A **76**, 022510 (2007).

[Bre33] G. Breit and Lawrence A. Wills, "Hyperfine Structure in Intermediate Coupling", Phys. Rev. **44**, 470 (1933).

[Cam08] Gretchen K. Campbell, Andrew D. Ludlow, Sebastian Blatt, Jan W. Thomsen, Michael J. Martin, Marcio H. G. de Miranda, Tanya Zelevinsky, Martin M. Boyd, Jun Ye, Scott A. Diddams, Thomas P. Heavner, Thomas E. Parker and Steven R. Jefferts, "The absolute frequency of the ^{87}Sr optical clock transition", Metrologia **45**, 539 (2008).

[Chi15] Nicola Chiodo, Nicolas Quintin, Fabio Stefani, Fabrice Wiotte, Emilie Camisard, Christian Chardonnet, Giorgio Santarelli, Anne Amy-Klein, Paul-Eric Pottie and Olivier Lopez, "Cascaded optical fiber link using the Internet network for remote clocks comparison", Opt. Express **23**, 33927 (2015).

[Cho10] C. W. Chou, D. B. Hume, J. C. J. Koelemeij, D. J. Wineland and T. Rosenband, "Frequency Comparison of Two High-Accuracy Al^+ Optical Clocks", Phys. Rev. Lett. **104**, 070802 (2010).

[Chu85] S. Chu, L. Hollberg, J. E. Bjorkholm, A. Cable and A. Ashkin, "Three-Dimensional Viscous Confinement and Cooling of Atoms by Resonance Radiation Pressure", Phys. Rev. Lett. **55**, 48 (1985).

[CIP13] "Report of the 101$^{\text{th}}$ Meeting of the Comité International des Poids et Mesures (CIPM)", Bureau International des Poids et Mesures (BIPM), Sevres, Paris Cedex 2013.

[CIP15] "Report of the 104$^{\text{th}}$ Meeting of the Comité International des Poids et Mesures (CIPM)", Bureau International des Poids et Mesures (BIPM), Sevres, Paris Cedex 2015.

[Cla91] A. Clairon, C. Salomon, S. Guellati and W. D. Phillips, "Ramsey Resonance in a Zacharias Fountain", Europhys. Lett. **16**, 165 (1991).

[Cun01] Steven T. Cundiff, Jun Ye and John L. Hall, "Optical frequency synthesis based on mode-locked lasers", Rev. Sci. Instrum. **72**, 3749 (2001).

[Dam96] Thibault Damour and Freeman Dyson, "The Oklo bound on the time variation of the fine-structure constant revisited", Nucl. Phys. B **480**, 37 (1996).

[Deg05] Carsten Degenhardt, Hardo Stoehr, Christian Lisdat, Guido Wilpers, Harald Schnatz, Burghard Lipphardt, Tatiana Nazarova, Paul-Eric Pottie, Uwe Sterr, Jürgen Helmcke and Fritz Riehle, "Calcium optical frequency standard with ultracold atoms: Approaching 10^{-15} relative uncertainty", Phys. Rev. A **72**, 062111 (2005).

[Der14] A. Derevianko and M. Pospelov, "Hunting for topological dark matter with atomic clocks", Nature Physics **10**, 933 (2014).

[Dic53] R. H. Dicke, "The Effect of Collisions upon the Doppler Width of Spectral Lines", Phys. Rev. **89**, 472 (1953).

[Dic88] G. John Dick, "Local oscillator induced instabilities in trapped ion frequency standards", in , *Proceedings of* 19th *Annu. Precise Time and Time Interval Meeting, Redendo Beach, 1987* (U.S. Naval Observatory, Washington, DC, 1988) , S. 133–147.

[Dro15] Stefan Droste, Christian Grebing, Julia Leute, Sebastian M. F. Raupach, Arthur Matveev, Theodor W. Hänsch, Andreas Bauch, Ronald Holzwarth and Gesine Grosche, "Characterization of a 450 km baseline GPS carrier-phase link using an optical fiber link", New J. Phys. **17**, 083044 (2015).

[Dzu99] V. A. Dzuba, V. V. Flambaum and J. K. Webb, "Calculations of the relativistic effects in many-electron atoms and space-time variation of fundamental constants", Phys. Rev. A **59**, 230 (1999).

[Dzu09] V. A. Dzuba and V. V. Flambaum, "Atomic calculations and search for variation of the fine-structure constant in quasar absorption spectra", Can. J. Phys. **87**, 15 (2009).

[Ein11] A. Einstein, "Über den Einfluß der Schwerkraft auf die Ausbreitung des Lichtes", Annalen der Physik **35**, 898 (1911).

[Ess55] L. Essen and J. V. L. Parry, in "The Caesium Frequency Standard", *NPL News* (1955).

[Fal11] St. Falke, H. Schnatz, J. S. R. Vellore Winfred, Th. Middelmann, St. Vogt, S. Weyers, B. Lipphardt, G. Grosche, F. Riehle, U. Sterr and Ch. Lisdat, "The ^{87}Sr optical frequency standard at PTB", Metrologia **48**, 399 (2011).

[Fal12] Stephan Falke, Mattias Misera, Uwe Sterr and Christian Lisdat, "Delivering pulsed and phase stable light to atoms of an optical clock", Appl. Phys. B **107**, 301 (2012).

[Fal14] Stephan Falke, Nathan Lemke, Christian Grebing, Burghard Lipphardt, Stefan Weyers, Vladislav Gerginov, Nils Huntemann, Christian Hagemann, Ali Al-Masoudi, Sebastian Häfner, Stefan Vogt, Uwe Sterr and Christian Lisdat, "A strontium lattice clock with 3×10^{-17} inaccuracy and its frequency", New J. Phys. **16**, 073023 (2014).

[Far81] John W. Farley and William H. Wing, "Accurate calculation of dynamic Stark shifts and depopulation rates of Rydberg energy levels induced by blackbody radiation. Hydrogen, helium, and alkali-metal atoms", Phys. Rev. A **23**, 2397 (1981).

[Fis04] M. Fischer, N. Kolachevsky, M. Zimmermann, R. Holzwarth, T. Udem, T. W. Hänsch, M. Abgrall, J. Grünert, I. Masimovic, S. Bize, H. Marion, F. Pereira Dos Santos, P. Lemonde, G. Santarelli, P. Laurent, A. Clairon, C. Salomon, M. Haas, U. D. Jentschura and C. H. Keitel, "New Limits on the Drift of Fundamental Constants from Laboratory Measurements", Phys. Rev. Lett. **92**, 230802 (2004).

[Fla09] V V Flambaum and V A Dzuba, "Search for variation of the fundamental constants in atomic, molecular, and nuclear spectra", Can. J. Phys. **87**, 25 (2009).

[For07] T. M. Fortier, N. Ashby, J. C. Bergquist, M. J. Delaney, S. A. Diddams, T. P. Heavner, L. Hollberg, W. M. Itano, S. R. Jefferts, K. Kim, F. Levi, L. Lorini, W. H. Oskay, T. E. Parker, J. Shirley and J. E. Stalnaker, "Precision Atomic Spectroscopy for Improved Limits on Variation of the Fine Structure Constant and Local Position Invariance", Phys. Rev. Lett. **98**, 070801 (2007).

[Gal79] T. F. Gallagher and W. E. Cooke, "Interactions of Blackbody Radiation with Atoms", Phys. Rev. Lett. **42**, 835 (1979).

[Ger10] V. Gerginov, N. Nemitz, S. Weyers, R. Schröder, R. D. Griebsch and R. Wynands, "Uncertainty evaluation of the caesium fountain clock PTB-CSF2", Metrologia **47**, 65 (2010).

[Gib13] Kurt Gibble, "Scattering of Cold Atom Coherences by Hot Atoms: Frequency Shifts from Background Gas Collisions", Phys. Rev. Lett. **110**, 180802 (2013).

[Gil11] Patrick Gill, "When should we change the definition of the second?", Phil. Trans. R. Soc. A **369**, 4109 (2011).

[Gre16] C. Grebing, A. Al-Masoudi, S. Dörscher, S. Häfner, V. Gerginov, S. Weyers, B. Lipphardt, F. Riehle, U. Sterr and C. Lisdat, "Realization of a timescale with an accurate optical lattice clock", Optica **3**, 563 (2016).

[GUM08] "Evaluation of measurement data – Guide to the expression of uncertainty in measurement", JCGM 100:2008 2008.

[Guo10] Kai Guo, Guangfu Wang and Anpei Ye, "Dipole polarizabilities and magic wavelengths for a Sr and Yb atomic optical lattice clock", Journal of Physics B: Atomic, Molecular and Optical Physics **43**, 135004 (2010).

[Hac14] H. Hachisu, M. Fujieda, S. Nagano, T. Gotoh, A. Nogami, T. Ido, St. Falke, N. Huntemann, C. Grebing, B. Lipphardt, Ch. Lisdat and D. Piester, "Direct comparison of optical lattice clocks with an intercontinental baseline of 9 000 km", Opt. Lett. **39**, 4072 (2014).

[Hac15] Hidekazu Hachisu and Tetsuya Ido, "Intermittent optical frequency measurements to reduce the dead time uncertainty of frequency link", Jpn. J. Appl. Phys. **54**, 112401 (2015).

[Häf15a] Sebastian Häfner, *Ultrastabile Lasersysteme für Weltraum- und Boden-Anwendungen*, PhD thesis Leibniz Universität Hannover 2015.

[Häf15b] Sebastian Häfner, Stephan Falke, Christian Grebing, Stefan Vogt, Thomas Legero, Mikko Merimaa, Christian Lisdat and Uwe Sterr, "8×10^{-17} fractional laser frequency instability with a long room-temperature cavity", Opt. Lett. **40**, 2112 (2015).

[Hai07] Jan Haisma, Nico Hattu, J. T. C. M. (Dook) Pulles, Esther Steding and Jan C. G. Vervest, "Direct bonding and beyond", Appl. Opt. **46**, 6793 (2007).

[Hän75] T. W. Hänsch and A. L. Schawlow, "Cooling of gases by laser radiation", Opt. Commun. **13**, 68 (1975).

[Hän06] Theodor W. Hänsch, "Nobel Lecture: Passion for precision", Rev. Mod. Phys. **78**, 1297 (2006).

[Hin13] N. Hinkley, J. A. Sherman, N. B. Phillips, M. Schioppo, N. D. Lemke, K. Beloy, M. Pizzocaro, C. W. Oates and A. D. Ludlow, "An atomic clock with 10^{-18} instability", Science **341**, 1215 (2013).

[Hon09] F.-L. Hong, M. Musha, M. Takamoto, H. Inaba, S. Yanagimachi, A. Takamizawa, K. Watabe, T. Ikegami, M. Imae, Y. Fujii, M. Amemiya, K. Nakagawa, K. Ueda and H. Katori, "Measuring the frequency of a Sr optical lattice clock using a 120 km coherent optical transfer", Opt. Lett. **34**, 692 (2009).

[Hum16] David B. Hume and David R. Leibrandt, "Probing beyond the laser coherence time in optical clock comparisons", Phys. Rev. A **93**, 032138 (2016).

[Hun12a] N. Huntemann, B. Lipphardt, M. Okhapkin, Chr. Tamm, E. Peik, A. V. Taichenachev and V. I. Yudin, "A generalized Ramsey excitation scheme with suppressed light shift", Phys. Rev. Lett. **109**, 213002 (2012).

[Hun12b] N. Huntemann, M. Okhapkin, B. Lipphardt, S. Weyers, Chr. Tamm and E. Peik, "High-accuracy optical clock based on the octupole transition in $^{171}Yb^{+}$", Phys. Rev. Lett. **108**, 090801 (2012).

[Hun14] N. Huntemann, B. Lipphardt, Chr. Tamm, V. Gerginov, S. Weyers and E. Peik, "Improved limit on a temporal variation of m_p/m_e from comparisons of Yb^+ and Cs atomic clocks", Phys. Rev. Lett. **113**, 210802 (2014).

[Hun16] N. Huntemann, C. Sanner, B. Lipphardt, Chr. Tamm and E. Peik, "Single-Ion Atomic Clock with 3×10^{-18} Systematic Uncertainty", Phys. Rev. Lett. **116**, 063001 (2016).

[Ita82] Wayne M. Itano, L. L. Lewis and D. J. Wineland, "Shift of $^2S_{1/2}$ hyperfine splittings due to blackbody radiation", Phys. Rev. A **25**, 1233 (1982).

[Ita93] W. M. Itano, J. C. Bergquist, J. J. Bollinger, J. M. Gilligan, D. J. Heinzen, F. L. Moore, M. G. Raizen and D. J. Wineland, "Quantum projection noise: Population fluctuations in two-level systems", Phys. Rev. A **47**, 3554 (1993) See Also: Erratum Phys. Rev. A 51, 1717 (1995).

[Jes99] James Jespersen and Jane Fitz-Randolph, "From Sundials to Atomic Clocks", Technical report NIST 1999.

[Kar04] edited by S. G. Karshenboim and E. Peik, *Astrophysics, Clocks and Fundamental Constants*, *Lecture Notes in Physics*, Vol.648, (Springer, Berlin, Heidelberg, New York, 2004) .

[Kat03] Hidetoshi Katori, Masao Takamoto, V. G. Pal'chikov and V. D. Ovsiannikov, "Ultrastable Optical Clock with Neutral Atoms in an Engineered Light Shift Trap", Phys. Rev. Lett. **91**, 173005 (2003).

[Kat09] Hidetoshi Katori, Koji Hashiguchi, E. Yu. Il'inova and V. D. Ovsiannikov, "Magic Wavelength to Make Optical Lattice Clocks Insensitive to Atomic Motion", Phys. Rev. Lett. **103**, 153004 (2009).

[Kat15] Hidetoshi Katori, V. D. Ovsiannikov, S. I. Marmo and V. G. Palchikov, "Strategies for reducing the light shift in atomic clocks", Phys. Rev. A **91**, 052503 (2015).

[Kes12] T. Kessler, C. Hagemann, C. Grebing, T. Legero, U. Sterr, F. Riehle, M. J. Martin, L. Chen and J. Ye, "A sub-40-mHz-linewidth laser based on a silicon single-crystal optical cavity", Nature Photonics **6**, 687 (2012).

[Kov04] Jean Kovalevsky and Terence J. Quinn, "The international system of units (SI) ", C. R. Physique **5**, 799 (2004).

[Le 13] R. Le Targat, L. Lorini, Y. Le Coq, M. Zawada, J. Guéna, M. Abgrall, M. Gurov, P. Rosenbusch, D. G. Rovera, B. Nagórny, R. Gartman, P. G. Westergaard, M. E. Tobar, M. Lours, G. Santarelli, A. Clairon, S. Bize, P. Laurent, P. Lemonde and J. Lodewyck, "Experimental realization of an optical second with strontium lattice clocks", Nature Com. **4**, 2109 (2013).

[Lem05] Pierre Lemonde and Peter Wolf, "Optical lattice clock with atoms confined in a shallow trap", Phys. Rev. A **72**, 033409 (2005).

[Lev99] Judah Levine, "Introduction to time and frequency metrology", Rev. Sci. Instrum. **70**, 2567 (1999).

[Lin15] Yi-Ge Lin, Qiang Wang, Ye Li, Fei Meng, Bai-Ke Lin, Er-Jun Zang, Zhen Sun, Fang Fang, Tian-Chu Li and Zhan-Jun Fang, "First Evaluation and Frequency Measurement of the Strontium Optical Lattice Clock at NIM", Chin. Phys. Lett. **32** (2015).

[Lis09] Ch. Lisdat, J. S. R. Vellore Winfred, T. Middelmann, F. Riehle and U. Sterr, "Collisional Losses, Decoherence, and Frequency Shifts in Optical Lattice Clocks with Bosons", Phys. Rev. Lett. **103**, 090801 (2009).

[Lis16] C. Lisdat, G. Grosche, N. Quintin, C. Shi, S. M. F. Raupach, C. Grebing, D. Nicolodi, F. Stefani, A. Al-Masoudi, S. Dörscher, S. Häfner, J. L. Robyr, N. Chiodo, S. Bilicki, E. Bookjans, A. Koczwara, S. Koke, A. Kuhl, F. Wiotte, F. Meynadier, E. Camisard, M. Abgrall, M. Lours, T. Legero, H. Schnatz, U. Sterr, H. Denker, C. Chardonnet, Y. Le Coq, G. Santarelli, A. Amy-Klein, R. Le Targat, J. Lodewyck, O. Lopez and P.-E. Pottie, "A clock network for geodesy and fundamental science", Nature Com. **7**, 12443 (2016).

[Lod12] Jerôme Lodewyck, Michal Zawada, Luca Lorini, Mikhail Gurov and Pierre Lemonde, "Observation and cancellation of a perturbing dc Stark shift in strontium optical lattice clocks", IEEE Trans. Ultrason. Ferroelectr. Freq. Control **59**, 411 (2012).

[Lop15] Olivier Lopez, Fabien Kéfélian, Haifeng Jiang, Adil Haboucha, Anthony Bercy, Fabio Stefani, Bruno Chanteau, Amale Kanj, Daniele Rovera, Joseph Achkar, Christian Chardonnet, Paul-Eric Pottie, Anne Amy-Klein and Giorgio Santarelli, "Frequency and time transfer for metrology and beyond using telecommunication network fibres", C. R. Physique **16**, 531 (2015) Special Issue: The measurement of time / La mesure du temps.

[Lor08] L. Lorini, N. Ashby, A. Brusch, S. Diddams, R. Drullinger, E. Eason1and T. Fortier, P. Hastings, T. Heavner, D. Hume, W. Itano, S. Jefferts, N. Newbury, T. Parker, T. Rosenband, J. Stalnaker, W. Swann, D. Wineland and J. Bergquist, "Recent atomic clock comparisons at NIST", Eur. Phys. J. Special Topics **163**, 19 (2008).

[Lud08a] A. D. Ludlow, T. Zelevinsky, G. K. Campbell, S. Blatt, M. M. Boyd, M. H. G. de Miranda, M. J. Martin, J. W. Thomsen, S. M. Foreman, Jun Ye, T. M. Fortier, J. E. Stalnaker, S. A. Diddams, Y. Le Coq, Z. W. Barber, N. Poli, N. D. Lemke, K. M. Beck and C. W. Oates, "Sr lattice clock at 1×10^{-16} fractional uncertainty by remote optical evaluation with a Ca clock", Science **319**, 1805 (2008).

[Lud08b] Andrew D. Ludlow, *The Strontium Optical Lattice Clock: Optical Spectroscopy with Sub-Hertz Accuracy*, PhD thesis University of Colorado, Boulder 2008.

[Lur62] A. Lurio, M. Mandel and R. Novick, "Second-Order Hyperfine and Zeeman Corrections for an (sl) Configuration", Phys. Rev. **126**, 1758 (1962).

[Mai60] T. H. Maiman, "Stimulated Optical Radiation in Ruby", Nature **187**, 493 (1960).

[Mar03] H. Marion, F. Pereira Dos Santos, M. Abgrall, S. Zhang, Y. Sortais, S. Bize, I. Maksimovic, D. Calonico, J. Grünert, C. Mandache, P. Lemonde, G. Santarelli, Ph. Laurent, A. Clairon and C. Salomon, "Search for Variations of Fundamental Constants using Atomic Fountain Clocks", Phys. Rev. Lett. **90**, 150801 (2003).

[Mat12] Kensuke Matsubara, Hidekazu Hachisu, Ying Li, Shigeo Nagano, Clayton Locke, Asahiko Nohgami, Masatoshi Kajita, Kazuhiro Hayasaka, Tetsuya Ido and Mizuhiko Hosokawa, "Direct comparison of a Ca^+ single-ion clock against a Sr lattice clock to verify the absolute frequency measurement", Opt. Express **20**, 22034 (2012).

[Met99] Harold J. Metcalf and Peter van der Straten, *Laser Cooling and Trapping*, (Springer, New York, Berlin, Heidelberg, 1999) .

[Mid11] Th. Middelmann, Ch. Lisdat, St. Falke, J. S. R. Vellore Winfred, F. Riehle and U. Sterr, "Tackling the blackbody shift in a strontium optical lattice clock", IEEE Trans. Instrum. Meas. **60**, 2550 (2011).

[Mid12a] Thomas Middelmann, Stephan Falke, Christian Lisdat and Uwe Sterr, "High Accuracy Correction of Blackbody Radiation Shift in an Optical Lattice Clock", Phys. Rev. Lett. **109**, 263004 (2012).

[Mid12b] Thomas Middelmann, Stephan Falke, Christian Lisdat and Uwe Sterr, "Long range transport of ultra cold atoms in a far-detuned one-dimensional optical lattice", New J. Phys. **14**, 073020 (13pp) (2012).

[Mid13] Thomas Middelmann, *Bestimmung des Einflusses thermischer Strahlung auf eine optische Strontium-Gitteruhr*, PhD thesis Fakultät für Mathematik und Physik der Gottfried Wilhelm Leibniz Universität Hannover 2013.

[Mit10] J. Mitroy and J. Y. Zhang, "Dispersion and polarization interactions of the strontium atom", Mol. Phys. **108**, 1999 (2010).

[Muk03] Takashi Mukaiyama, Hidetoshi Katori, Tetsuya Ido, Ying Li and Makoto Kuwata-Gonokami, "Recoil-Limited Laser Cooling of Sr Atoms near the Fermi Temperature", Phys. Rev. Lett. **90**, 113002 (2003).

[Naf07] Mira Naftaly and Robert E. Miles, "Terahertz Time-Domain Spectroscopy for Material Characterization", Proc. IEEE **95**, 1658 (2007).

[Nic12] T.L. Nicholson, M.J. Martin, J.R. Williams, B.J. Bloom, M. Bishof, M.D. Swallows, S.L. Campbell and J. Ye, "Comparison of Two Independent Sr Optical Clocks with 1×10^{-17} Stability at 10^3 s", Phys. Rev. Lett. **109**, 230801 (2012).

[Nic15] T. L. Nicholson, S. L. Campbell, R. B. Hutson, G. E. Marti, B. J. Bloom, R. L. McNally, W. Zhang, M. D. Barrett, M. S. Safronova, G. F. Strouse, W. L. Tew and J. Ye, "Systematic evaluation of an atomic clock at 2×10^{-18} total uncertainty", Nature Com. **6**, 6896 (2015).

[Par99] Thomas E. Parker, "Hydrogen Maser Ensemble performance and Characterization of Frequency Standards", in , *Proceedings of the 1999 Joint Meeting of the European Frequency and Time Forum and The IEEE International Frequency Control Symposium* (1999) , S. 173–176.

[Pei04] E. Peik, B. Lipphardt, H. Schnatz, T. Schneider, Chr. Tamm and S. G. Karshenboim, "Limit on the Present Temporal Variation of the Fine Structure Constant", Phys. Rev. Lett. **93**, 170801 (2004).

[Pei06] E. Peik, B. Lipphardt, H. Schnatz, Chr. Tamm, S. Weyers and R. Wynands, "Laboratory Limits on Temporal Variations of Fundamental Constants: An Update", arXiv:physics/0611088 Proceedings of the 11th Marcel Grossmann Meeting, Berlin, 2006 (2006).

[Pei10] Ekkehard Peik, "Fundamental constants and units and the search for temporal variations", Nuclear Physics B (Proc. Suppl.) **203–204**, 18 (2010).

[Phi85] William D. Phillips, Jon V. Prodan and Harold J. Metcalf, "Laser cooling and electromagnetic trapping of neutral atoms", J. Opt. Soc. Am. B **2**, 1751 (1985).

[Por06] Sergey G. Porsev and Andrei Derevianko, "Multipolar theory of blackbody radiation shift of atomic energy levels and its implications for optical lattice clocks", Phys. Rev. A **74**, 020502 (2006).

[Pre12] K. Predehl, G. Grosche, S. M. F. Raupach, S. Droste, O. Terra, J. Alnis, Th. Legero, T. W. Hänsch, Th. Udem, R. Holzwarth and H. Schnatz, "A 920-Kilometer Optical Fiber Link for Frequency Metrology at the 19th Decimal Place", Science **336**, 441 (2012).

[Ram83] Norman F. Ramsey, "History of Atomic Clocks", J. Res. NBS **88**, 301 (1983).

[Rau14a] S. M. F. Raupach and G. Grosche, "Chirped Frequency Transfer: A Tool for Synchronization and Time Transfer", IEEE Trans. Ultrason. Ferroelectr. Freq. Control **61**, 920 (2014).

[Rau14b] S. M. F. Raupach, A. Koczwara and G. Grosche, "Optical frequency transfer via a 660 km underground fiber link using a remote Brillouin amplifier", Opt. Express **22**, 26537 (2014).

[Rau15] Sebastian M. F. Raupach, Andreas Koczwara and Gesine Grosche, "Brillouin amplification supports 1×10^{-20} accuracy in optical frequency transfer over 1400 km of underground fibre", Phys. Rev. A **92**, 021801(R) (2015).

[Rie15] Fritz Riehle, "Towards a redefinition of the second based on optical atomic clocks", C. R. Physique **16**, 506 (2015) Special issue: The measurement of time / La mesure du temps.

[Ros08] T. Rosenband, D. B. Hume, P. O. Schmidt, C. W. Chou, A. Brusch, L. Lorini, W. H. Oskay, R. E. Drullinger, T. M. Fortier, J. E. Stalnaker, S. A. Diddams, W. C. Swann, N. R. Newbury, W. M. Itano, D. J. Wineland and J. C. Bergquist, "Frequency Ratio of Al^+ and Hg^+ Single-Ion Optical Clocks; Metrology at the 17th Decimal Place", Science **319**, 1808 (2008).

[Rus24] H. N. Russell and F. A. Saunders, "New Regularities in the Spectra of the Alkaline Earths", Astrophys. J. **61**, 38 (1924).

[Saf10] Marianna S. Safronova, Dansha Jiang, Bindiya Arora, Charles W. Clark, Mikhail G. Kozlov, Ulyana I. Safronova and Walter R. Johnson, "Black-Body Radiation Shifts and Theoretical Contributions to Atomic Clock Research", IEEE Trans. Ultrason. Ferroelectr. Freq. Control **57**, 94 (2010).

[San98] Giorgio Santarelli, Claude Audoin, Ala'a Makdissi, Philippe Laurent, G. John Dick and André Clairon, "Frequency Stability Degradation of an Oscillator Slaved to a Periodically Interrogated Atomic Resonator", IEEE Trans. Ultrason. Ferroelectr. Freq. Control **45**, 887 (1998).

[Sch96] H. Schnatz, B. Lipphardt, J. Helmcke, F. Riehle and G. Zinner, "First Phase-Coherent Frequency Measurement of Visible Radiation", Phys. Rev. Lett. **76**, 18 (1996).

[Sch99] C. Schwob, L. Jozefowski, B. de Beauvoir, L. Hilico, F. Nez, L. Julien, F. Biraben, O. Acef and A. Clairon, "Optical Frequency Measurement of the $2S - 12D$ Transitions in Hydrogen and Deuterium: Rydberg Constant and Lamb Shift Determinations", Phys. Rev. Lett. **82**, 4960 (1999) Erratum in [Sch01].

[Sch01] C. Schwob, L. Jozefowski, B. de Beauvoir, L. Hilico, F. Nez, L. Julien, F. Biraben, O. Acef and J.-J. Zondyand A. Clairon, "Erratum: Optical Frequency Measurement of the $2S-12D$ Transitions in Hydrogen and Deuterium: Rydberg Constant and Lamb Shift Determinations", Phys. Rev. Lett. **86**, 4193 (2001) Erratum in: Phys. Rev. Lett. **86**, 4193 (2006).

[Sch06] S. Scheithauer and C. Lämmerzahl, "Analytical Solution for the Deformation of a Cylinder under Tidal Gravitational Forces", arXiv:physics/0606250 (2006).

[Sch09] S. Schiller, G. Tino, P. Gill, C. Salomon, U. Sterr, E. Peik, A. Nevsky, A. Görlitz, D. Svehla, G. Ferrari, N. Poli, L. Lusanna, H. Klein, H. Margolis, P. Lemonde, P. Laurent, G. Santarelli, A. Clairon, W. Ertmer, E. Rasel, J. Müller, L. Iorio, C. Lämmerzahl, H. Dittus, E. Gill, M. Rothacher, F. Flechner, U. Schreiber, V. Flambaum, Wei-Tou Ni, Liang Liu, Xuzong Chen, Jingbiao Chen, Kelin Gao, L. Cacciapuoti, R. Holzwarth, M. Heß and W. Schäfer, "Einstein Gravity Explorer – a medium-class fundamental physics mission", Experimental Astronomy **23**, 573 (2009).

[Shl76] A. I. Shlyakther, "Direct test of the constancy of fundamental nuclear constants", Nature **264**, 340 (1976).

[Sia08] C. Sias, H. Lignier, Y. P. Singh, A. Zenesini, D. Ciampini, O. Morsch and E. Arimondo, "Observation of Photon-Assisted Tunneling in Optical Lattices", Phys. Rev. Lett. **100**, 040404 (2008).

[Sri04] R. Srianand, H. Chand, P. Petitjean and B. Aracil, "Limits on the Time Variation of the Electromagnetic Fine-Structure Constant in the Low Energy Limit from Absorption Lines in the Spectra of Distant Quasars", Phys. Rev. Lett. **92**, 121302 (2004).

[Ste15] Fabio Stefani, Olivier Lopez, Anthony Bercy, Won-Kyu Lee, Christian Chardonnet, Giorgio Santarelli, Paul-Eric Pottie and Anne Amy-Klein, "Tackling the Limits of Optical Fiber Links", J. Opt. Soc. Am. B **32**, 787 (2015).

[Str77] U. Strom and P. C. Taylor, "Temperature and frequency dependences of the far-infrared and microwave optical absorption in amorphous materials", Phys. Rev. B **16**, 5512 (1977).

[Tai07] A. V. Taichenachev, V. I. Yudin and C. W. Oates, "Optical lattice polarization effects on magnetically induced optical atomic clock transition", Phys. Rev. A **76**, 023806 (2007).

[Tai08] A. V. Taichenachev, V. I. Yudin, V. D. Ovsiannikov, V. G. Pal'chikov and C. W. Oates, "Frequency Shifts in an Optical Lattice Clock Due to Magnetic-Dipole and Electric-Quadrupole Transitions", Phys. Rev. Lett. **101**, 193601 (2008).

[Tak03] Masao Takamoto and Hidetoshi Katori, "Spectroscopy of the $^1S_0 \rightarrow ^3P_0$ Clock Transition of ^{87}Sr in an Optical Lattice", Phys. Rev. Lett. **91**, 223001 (2003).

[Tan15] Takehiko Tanabe, Daisuke Akamatsu, Takumi Kobayashi, Akifumi Takamizawa, Shinya Yanagimachi, Takeshi Ikegami, Tomonari Suzuyama, Hajime Inaba, Sho Okubo, Masami Yasuda, Feng-Lei Hong, Atsushi Onae and Kazumoto Hosaka, "Improved frequency measurement of the $^1S_0$-$^3P_0$ clock transition in ^{87}Sr using a Cs fountain clock as a transfer oscillator", J. Phys. Soc. Jpn. **84**, 115002 (2015).

[Tel96] "Absolute Measurement of optical frequencies", edited by M. Ohtsu, M. Ohtsu, (1996).

[Ush15] Ichiro Ushijima, Masao Takamoto, Manoj Das, Takuya Ohkubo and Hidetoshi Katori, "Cryogenic optical lattice clocks", Nature Photonics **9**, 185 (2015).

[Uza03] Jean-Philippe Uzan, "The fundamental constants and their variation: observational and theoretical status", Rev. Mod. Phys. **75**, 403 (2003).

[Vel10] Joseph Sundar Raaj Vellore Winfred, *Investigation of collisional losses and decoherence in a 1-D optical lattice clock with ^{88}Sr*, PhD thesis Fakultät für Mathematik und Physik der Gottfried Wilhelm Leibniz Universität Hannover 2010.

[Vog15] Stefan Vogt, *Eine transportable optische Gitteruhr basierend auf Strontium*, PhD thesis QUEST-Leibniz-Forschungsschule der Universität Hannover 2015.

[Vor12] V. Vorontsov, A. Belyaev and N. Demidov, "Design of the active hydrogen maser new model (VCH-1003M) using microwave cavity frequency switching technique for cavity auto tuning", in , *Materials of the VI symposium "metrology of time and space" 2012* (2012).

[Web01] J. K. Webb, M. T. Murphy, V. V. Flambaum, V. A. Dzuba, J. D. Barrow, C. W. Churchill, J. X. Prochaska and A. M. Wolfe, "Further evidence for cosmological evolution of the fine structure constant", Phys. Rev. Lett. **87**, 091301 (2001).

[Web11] Stephen Webster and Patrick Gill, "Force-insensitive optical cavity", Opt. Lett. **36**, 3572 (2011).

[Wei94] M. Weitz, A. Huber, F. Schmidt-Kaler, D. Leibfried and T. W. Hänsch, "Precision Measurement of the Hydrogen and Deuterium 1S ground state Lamb shift", Phys. Rev. Lett. **72**, 328 (1994).

[Wes10a] Philip Westergaard, *Horloge à réseau optique au Strontium : en quête de la performance ultime*, PhD thesis Ecole nationale supérieure des telecommunications 2010.

[Wes10b] Philip G. Westergaard, Jeŕôme Lodewyck and Pierre Lemonde, "Minimizing the Dick effect in an optical lattice clock", IEEE Trans. Ultrason. Ferroelectr. Freq. Control **57**, 623 (2010).

[Wes11] P. G. Westergaard, J. Lodewyck, L. Lorini, A. Lecallier, E. A. Burt, M. Zawada, J. Millo and P. Lemonde, "Lattice-Induced Frequency Shifts in Sr Optical Lattice Clocks at the 10^{-17} Level", Phys. Rev. Lett. **106**, 210801 (2011).

[Wey01] S. Weyers, U. Hübner, R. Schröder, Chr. Tamm and A. Bauch, "Uncertainty evaluation of the atomic caesium fountain CSF1 of the PTB", Metrologia **38**, 343 (2001).

[Wey02] S. Weyers, A. Bauch, R. Schröder and Chr. Tamm, "The Atomic Caesium Fountain CSF1 of PTB", in , *Frequency Standards and Metrology, Proceedings of the Sixth Symposium*, edited by P. Gill, (World Scientific, Singapore, 2002) , S. 64–71.

[Wey12] S. Weyers, V. Gerginov, N. Nemitz, R. Li and K. Gibble, "Distributed cavity phase frequency shifts of the caesium fountain PTB-CSF2", Metrologia **49**, 82 (2012).

[Win75] D. Wineland and H. Dehmelt, "Proposed 10^{14} $\Delta\nu/\nu$ laser fluorescence spectroscopy on Tl^+ mono-ion oscillator III", Bull. Am. Phys. Soc. **20**, 637 (1975).

[Win79] D. J. Wineland and Wayne M. Itano, "Laser cooling of atoms", Phys. Rev. A **20**, 1521 (1979).

[Xia87] Min Xiao, Ling-An Wu and H. J. Kimble, "Precision Measurement beyond the Shot-Noise Limit", Phys. Rev. Lett. **59**, 278 (1987).

[Yam12] Atsushi Yamaguchi, Nobuyasu Shiga, Shigeo Nagano, Ying Li, Hiroshi Ishijima, Hidekazu Hachisu, Motohiro Kumagai and Tetsuya Ido, "Stability Transfer between Two Clock Lasers Operating at Different Wavelengths for Absolute Frequency Measurement of Clock Transition in ^{87}Sr", Appl. Phys. Express **5**, 022701 (2012).

CV

Ali Al-masoudi

PERSONAL DATA

First name	Ali
Surname	AL-Masoudi
Birthday	04.07.1986
marital status	Single
E-Mail	ali.al-masoudi@ptb.de

EDUCATION

Since 02/2013	PhD student at Physikalisch-Technische Bundesanstalt (PTB) Braunschweig
10/2010 - 12/2012	Master Student at Department of Physics / Heinrich Heine Universität Düsseldorf – Germany
06/2010 - 10/2010	German Language Courses (Goethe Institute in Göttingen - Germany)
10/2009 - 06/2010	Master Student at Department of Physics / University of Baghdad (Baghdad - Iraq)
10/2004 - 07/2008	Bachelor Student at Department of Physics / University of Baghdad (Baghdad - Iraq)
07/2004	Al-Iskendaria School (Babylon - Iraq)
	Baccalaureate degree

Research Interests

Cold Atoms, Laser cooling and Trapping

Optical clocks

Languages

Arabic (mother tongue)
English (stable)
German (stable)

Acknowledgements

I would like to express my deep grateful to those who worked together with me, helped me and supported me during my PhD time at PTB.

- I would like to thank my supervisor PD Dr. Christian Lisdat for offering me a position in his excellent research group. I have to say that he was more than a supervisor for me. I was lucky that I had the opportunity to meet him almost every day and discuss with him the status of the experiment and results, new ideas, and suggestions. I appreciated so much the time he spent with me in the office and in the laboratory. I would like to thank:

- Dr. Uwe Sterr for has helpful discussions and tremendous support.

- Prof. Dr. Ernst Rasel for been my montor and the second referee of my PhD defense.

- Prof.Dr. Klemens Hammerer for has time to be the head of the board of my PhD defense.

- Dr. Stephan Falke, during my first year at PTB, I worked with him in the experiment. I learned from him a lot in the laboratory.

- Dr. Sören Dörscher, after Stephan Falke left our group, Sören show up in our group as a post-doc. I enjoyed the work with him, especially during the measurement campaigns when the clock was running continuous for several weeks. Also I would like to thank him for reading my PhD thesis.

- Dr. Stefan Vogt and Dr.Sebaistian Häfner, for working together in the laboratory. I would like to thank Stefan Vogt once more for translating the abstract to German.

- Dr. Silvio Koller, Sofia Herbers, Jacopo Grotti, Roman Schwarz for their helped.

- Evgenij Pachomow, Veit Dahlke, Dr. Max Kahmann, and Dr. Oliver Appelt for their helped.

- Dr. Sebastian Raupach, Dr. Christian Grebing, Dr. Thomas legero, Dr. Dan Matei, Robin Weyrich, Dr. Alexander Kuhl, Dr. Sebastian Koke for their helped and supported.
- Andre Uhde , Mandy Rindermann, and Klemens Budin for their help for providing mechanical components.
- Andreas Koczwara, Mattias Misera and Marion Wengel for their help in providing electronic components.
- Prof. Fritz Reihle, Prof. Harald Schnatz, and Dr. Gesine Grosche for their supported.
- Department 4.4 (Time and Frequency) at PTB, I would like to thank all of them for their supported, we did a lot of interesting measurements together.
- Our colleagues at SYRTE Paris (Sr clock group, fiber link group, and frequency comb group) for interesting measurement campaigns via a fiber link.
- Dr. Christian Monte and has colleagues at PTB-Berlin for measuring the transmission of BK7 windows.
- Mrs. Brigit Voss, Mrs. Susanne Ehrenpfordt, and Mrs. Birgit Ohlendorf for their assistance in administrative issues.
- Last but not least, I would like express my deep love to my family.